

Quantification of induced seismicity potential of geothermal operations

Analytical and numerical model approaches

FINAL REPORT by

Loes Buijze, Peter A. Fokker, Brecht Wassing 10 december 2021

Quantification of induced seismicity potential of geothermal operations



Loes Buijze, Peter Fokker, Brecht Wassing 10 december 2021

Dit project is uitgevoerd als onderdeel van het Innovatieplan WarmingUP. Dit is mede mogelijk gemaakt door subsidie van de Rijksdienst voor Ondernemend Nederland (RVO) in het kader van de subsidieregeling Meerjarige Missiegedreven Innovatie Programma's (MMIP), bij RVO bekend onder projectnummer TEUE819001.

WarmingUP geeft invulling aan MMIP-4 – Duurzame warmte en koude in gebouwde omgeving en levert daarmee een bijdrage aan Missie B – Een CO_2 -vrije gebouwde omgeving in 2050.

Projectnummer

060.43190

Keywords

Geothermal doublets, induced seismicity

Jaar van publicatie

2021

Meer informatie

B.B.T. Wassing T 06 46966142

E brecht.wassing@tno.nl

August 2021 ©

Alle rechten voorbehouden. Niets uit deze uitgave mag worden verveelvoudigd, opgeslagen in een geautomatiseerd gegevens bestand, of openbaar gemaakt, in enige vorm of op enige wijze, hetzij elektronisch, mechanisch, door fotokopieën, opnamen, of enig andere manier, zonder voorafgaande schriftelijke toestemming van de uitgever.

Inhoudsopgave

1	Executive summary				
2	Introdu	uction	g		
	2.1	Geothermal target formations in the Netherlands	10		
3	Stress	changes and fault reactivation around an injection well: a fast model	14		
	3.1	Abstract	14		
	3.2	Introduction	14		
	3.3	Method	15		
	3.4	Results	17		
	3.4.1	Representative case	17		
	3.4.2	Variable input	24		
	3.4.3	Probabilistic input	27		
	3.5	Discussion & Conclusion	33		
4	Cooling	g- and depletion-induced rupture in a faulted reservoir	35		
	4.1	Abstract	35		
	4.2	Introduction	35		
	4.3	Methods	36		
	4.3.1	Model setup	36		
	4.3.2	Pressure and temperature changes	37		
	4.3.3	Pressure- or temperature-induced stress changes	38		
	4.3.4	Modeling of fault reactivation and onset of seismic fault slip	39		
	4.3.5	Rupture length	40		
	4.3.6	Input parameters and stochastic analysis	40		
	4.4	Results	42		
	4.4.1	A different stress path for depletion and cooling	42		
	4.4.2	Fault offset locally concentrates fault shear stress	43		
	4.4.3	Reactivation for depletion and cooling	44		
	4.4.4	Along-dip rupture length	47		
	4.5	Discussion & Conclusions	49		
	4.5.1	Depletion-induced fault reactivation: comparison with previous works	49		
	4.5.2	Cooling-induced fault reactivation	50		
	4.5.3	Rupture lengths and potential for rupture to propagate outside of the reservoir interval	51		
	4.5.4	Implications for induced seismicity in geothermal doublets	53		
	4.6	Conclusions & Recommendations	53		
5	Fault re	eactivation potential near a geothermal doublet: a 3D model	55		
	5.1	Abstract	55		
	5.1	Introduction	56 56		
	5.3	Methods	56		
	5.3.1	Model geometry	56		

	5.3.2	Pressure and temperature calculation	58
	5.3.3	Poro-thermo-elastic stress calculation	59
	5.4	Results	59
	5.4.1	Doublet parallel to fault – injection well at 750 m	59
	5.4.2	Doublet parallel to fault – injection well at 100 m	61
	5.4.3	Effect of doublet orientation with respect to fault orientation	63
	5.4.4	Effect of reservoir offset on stress changes	64
	5.4.5	Stiffer seal and base formation	65
	5.5	Discussion & Conclusion	66
6	Integra	ation and discussion	69
	6.1	Comparison of the different modeling tools	69
	6.1.1	Summary of model setup and advantages and limitations	69
	6.1.2	Temperature distributions used in OPM-DIANA3D, SRIMA and PANTHER2D	70
	6.1.3	Stress changes in the reservoir and comparison to uniaxial stress change	72
	6.1.4	Fault stress changes on offset faults	73
	6.1.5	Applications of the different modeling tools	75
	6.1.6	Main model assumptions and recommendations on further tool development	76
	6.2	Key factors driving fault reactivation and seismicity	77
	6.3	Seismic rupture and magnitude – comparison depletion and cooling	78
	6.4	If cooling induces such significant stress changes, why have we not observed felt	
		seismicity near geothermal doublets in sandstone reservoirs?	82
7	Conclu	sions	85
8	Refere	nces	89
Bi	ilage A S	SRIMA background theory and benchmark	93
	A.1	Temperature field	94
	A.2	Pressure field	94
	A.3	Thermo-elastic stress	95
	A.4	Poro-elastic stress	96
	A.5	Total stresses and Risk Measures	97
	A.6	Benchmark of the pressure and temperature calculation in SRIMA	98
	A.7	Benchmark of stress calculation: Model setup and input parameters	102
	A.8	Benchmark of stress changes - Uniform elasticity	105
	A.9	Benchmark of stress changes - Stiffer seal and base	107
	A 10	Renchmark of stress changes - More compliant seal and hase	109

1 Executive summary

The Dutch National Climate Agreement sets the goal to adapt before 2030 1.5 million homes which are now heated by natural gas, into buildings heated by sustainable heat. To this end, a growth of the use of sustainable heat sources needs to be realized. Geothermal energy is considered an important future heat source, with an expected supply of 15 - 50 PJ in 2030 of sustainable heat to district heat networks and greenhouses (Stichting Plaftorm Geothermie et al., 2018, PBL et al., 2020). Theme 4 in the WarmingUp (MMIP4) project aims to accelerate and upscale geothermal development for sustainable heating in the built environment.

For safe and effective application of geothermal energy, it is important to assess the effects of geothermal operations on fault stability and induced seismicity. Work package 4B specifically focuses on the quantification and management of risks related to induced seismicity as a result of geothermal operations. Understanding the mechanisms of stress changes around geothermal doublets, the conditions under which faults could be reactivated and what controls the magnitudes of induced events, is crucial for site-specific hazard assessment and the development of mitigation measures. The use of geomechanical models helps understand and evaluate the (relative role) of important processes, key geological properties, and operational settings affecting fault reactivation and seismic hazard. The main objective of this study is to develop practical methods and modelling workflows for seismic hazard assessment in conventional geothermal projects in the Netherlands, where fluids are circulated through porous sandstone formations. We test and demonstrate the workflows for generic geological and operational settings representative for geothermal operations in the Netherlands. The methods and workflows can be used as a base for guidelines and criteria for field development. Note that the models as presented here always employ (simplifying) assumptions, and capture processes and subsurface complexities only to a limited extent, leading to substantial (epistemic) uncertainties. Though general trends may well be captured and models help understand the general response to cold water injection, for further (field-specific) applications, the models should be informed with available subsurface data, and importantly, be validated through the integration with field data and monitoring data.

Most conventional geothermal systems in the Netherlands produce heat from hot sedimentary aquifers of Tertiary, Cretaceous/Jurassic, Triassic or Permian (Rotliegend) age (e.g. Buijze et al., 2019a). Geothermal energy extraction is generally executed using a geothermal doublet, consisting of an injector and producer in combination with a surface heat exchange facility. As produced fluids are reinjected in the reservoir at temperatures between 20-45°C, long-term injection over the lifetime of a geothermal installation will lead to a progressive cooling of the reservoir rocks. Pressure changes related to production and injection and thermal stresses related to long-term cooling cause stress changes which may affect the reactivation and seismicity potential of faults near the geothermal doublet.

In this report we present three modelling tools for analysis of fault reactivation potential near geothermal doublets, i.e. SRIMA, PANTHER2D and DIANA-OPM. Each of these tools has its own merits and limitations, and each can be used for different purposes. SRIMA and PANTHER2D are (semi-)analytical tools which can give a first order assessment of fault reactivation, and in case of PANTHER2D, induced event magnitudes. The speed of these tools allows for incorporation of uncertainties in stochastic and sensitivity analyses, providing insights into the key factors that drive the potential of fault reactivation and seismicity. As they are based on simplified geometries, they are generally less well suited to capture the effects of geological complexity, heterogeneity and the spatio-temporal evolution of the cooling front. The FE numerical tool of OPM-DIANA analysis is complementary to the fast analyses of SRIMA and PANTHER2D, incorporating less parameter uncertainty but a higher degree of subsurface complexity.

We compare and benchmark results of SRIMA, PANTHER2D and the 3D analysis in OPM-DIANA to assess their specific application and limitations for use. We then use the tools to further our understanding of the hazard of fault reactivation and induced seismicity related to geothermal doublet operations, with specific focus on the following questions:

- What are the key factors that drive fault reactivation and induced seismicity in geothermal doublet operations?:
 - O Which parameters affect (the likelihood of) fault reactivation?
 - O Which parameters affect the extent of fault rupture?
- What is the extent of the cooling front and the critically perturbed zone around the geothermal doublets?
- What are the differences between seismicity induced by cooling (geothermal doublet operations) and by depletion (gas production)? This comparison of cooling-induced seismicity and depletion-induced seismicity is specifically interesting as there is a long history of gas production from onshore gas fields in the Netherlands, with multiple fields that have shown induced seismicity.

We demonstrate the use of **SRIMA** (Seal and Reservoir Integrity Mechanical Analysis) for the analysis of the potential of fault reactivation during injection operations. For a simplified scenario of constant injection into a single vertical well in a reservoir with homogeneous flow and temperature properties, SRIMA allows to map the reactivation risk associated to different injection and subsurface scenarios. Based on an extensive benchmark study, we consider the tool appropriate for a first screening of the extent of the cooled volume and the fault reactivation potential perpendicular to the doublet orientation. Due to its radial-symmetry SRIMA cannot capture the asymmetry of the cooling front during the later stages of injection, as it preferentially grows to the production well with increasing injection time. The use of SRIMA should be limited to reservoirs where advective heat transfer is dominant in the reservoir, where fault offset remains limited (less than the reservoir height), and faults are fully open and in cases where the elasticity ratio between seal and aquifer is larger than a factor 0.5. The assumption of a simplified radial-symmetrical geometry implies some limitations for use, e.g. for strongly deviated wells or when interaction between multiple wells is expected, and in case geothermal doublet operations occur in heterogeneous reservoirs with high-permeability streaks, or in presence of permeable fault systems.

Sensitivity analysis in SRIMA shows that stress changes for geothermal doublet operations in porous sandstone formations derive almost exclusively from temperature decreases around the injection well. The temperature decrease can be up to several 10's of degrees over hundreds of meters from the injection well, whereas pressure changes are often small (<1 MPa) and limited to the vicinity of the injection well. Normal faults that lie within the cooled volume around the injection well experience destabilization – i.e. the Coulomb stress on the fault increases and moves to less stable conditions. Destabilization occurs at the reservoir depth level, as well as just above in the seal and below in the base, as these also experience some degree of cooling. Destabilization can also occur outside the cooled reservoir volume due to stress transfer, although the stress changes decay rapidly beyond the cooled reservoir volume. The fault area that experiences positive Coulomb stress changes is elliptical and increases in size as the cooled volume around the injection well increases with operation time. Simultaneously, the Coulomb stress changes increase with the radius of the cooled volume. The magnitude of Coulomb stress changes depends predominantly on the difference between reinjection and reservoir temperature and the thermo-elastic properties of the reservoir formation. Whether faults are reactivated or not depends on the Coulomb stress change in combination with the pre-existing, tectonic state of stress in and around the geothermal reservoir. Initial stress criticality, temperature difference between injected fluids and reservoir, thermal expansion coefficient and elastic modulus are thus key parameters that increase the potential for fault reactivation. Additionally, the modulus contrast between seal and aquifer is important. A stiff seal and base formation results in larger Coulomb stress changes above and below the reservoir, and a larger fault area that experiences destabilization. This is because the seal and base also cool down, and the thermo-elastic stress in the seal and base are larger than those in the reservoir because of the higher Young's modulus. Even tensile stresses may develop, increasing the risk of inducing hydraulic fractures in the seal. Regarding radius of criticality, we find that when the initial criticality of the stress regime is moderate or low, fault reactivation is not expected for distances from the injection well of more than 1.3 times the radius of the cold front. Only in case of (close to) critical initial stress conditions, radii of criticality can be much larger than the radius of cooling. Radii of criticality can be particularly large (exceeding 500m) in case of an initial stress regime that is critical, or in case of small reservoir thickness. This is an important finding when designing geothermal operations in a reservoir with pre-existing faults or fault structures.

We used **Panther2D** to compare reactivation and rupture characteristics for both a depleting and for a cooling reservoir. Panther2D is a fast, semi-analytical 2D model approach which allows for a rapid stochastic investigation of pressures or temperatures required for fault reactivation and rupture length (i.e. the along-dip fault that slipped during the seismic event), taking into account reservoir offset and rupture dynamics. Panther2D incorporates fault weakening behavior which is a fundamental aspect of seismic instability on faults and crucial for the assessment of magnitudes of seismic events. In our model, we assume the fault is open and lies within the depleted or cooled volume. The assumption of equal cooling of reservoir blocks on both sides of the fault is conservative for cooling and results in a conservative estimate of rupture lengths (simulating e.g. an undetected fault near the injection well).

Using Panther2D, we show that mechanisms of cooling-induced and depletion-induced fault reactivation are distinctly different. The direction of the stress path for cooling is on average more destabilizing than for depletion, which is reflected in a higher fault reactivation potential for cooling. This is because the effective normal stress decreases during cooling but increases during depletion. Note that this conclusion holds for faults that lie within the cooled or depleted area. Complementary to SRIMA, the model configuration in Panther2D allows for the analysis of the effect of fault throw on fault reactivation. Fault throw offsetting cooling and depleting reservoir formations tends to concentrate fault stresses and hence promotes reactivation for steep normal faults. The more abrupt variations in temperature or pressure changes between formations, the larger the stress concentrations, in particular near the edges of formations. The more diffuse the pressure and/or temperature profile, the smoother the stress changes and the smaller the stress concentrations. Sensitivity analysis in Panther2D indicates fault reactivation for depleting reservoirs is strongly controlled by fault throw, the poro-elastic stress parameters Poisson's ratio v and Biot coefficient, and the initial tectonic stress. On the other hand, Panther2D confirms the observation from SRIMA that fault reactivation potential for cooling reservoirs depends predominantly on the reinjection temperature and thermo-elastic properties (Young's modulus and linear thermal expansion coefficient) of the reservoir formation and initial stress, and to a lesser extent on fault throw. Key factors determining the along-dip rupture length for cooling and depletion are similar, with rupture length mostly controlled by the initial tectonic stress ratio, fault dip and frictional weakening parameters. In addition, reservoir thickness and fault throw influenced rupture length, with thicker reservoirs causing larger events. Computed rupture lengths are larger for cooling than for depletion, because cooling of the seal and base results in a longer fault length that experiences stress changes compared to depletion. However, even though computed along-dip rupture lengths are larger, the along-strike dimensions and stress drops are typically smaller for cooling. Estimates of along-dip rupture length, along-strike dimensions and stress drop can be used to obtain a first-order estimate of maximum magnitudes of events. When assuming the events span the entire cooled volume, maximum event magnitude estimates for cooling are in the same range as those estimated for the small gas fields in the Netherlands. The assumption of an along-strike dimension of the rupture over entire cooled area is however a very conservative one. In the more likely scenario that only part of the cooled volume affects the fault, maximum magnitude estimates for cooling are smaller than for the small gas fields. Moreover, while for depletion the pressure change occurs relatively uniformly along the strike of the fault, for cooling around an injection well the fault area affected by the temperature change will grow with time. This may lead to a different evolution of seismicity (and

maximum magnitude) and potentially a more gradual release of seismic energy with time than for gas depletion.

We used **OPM-DIANA** to model fault reactivation in 3D, taking into account the asymmetrical spatiotemporal evolution of the cooling front between the injection and production well, realistic fault and reservoir geometries and heterogeneities, such as stiffness contrasts between reservoir, base and seal. In contrast to the other tools, it can be used to assess the effects of doublet configuration on fault reactivation potential (e.g. doublet orientation with respect to the fault and distance between injection and production well). As modelling in OPM-DIANA is computer-intensive, fully stochastic analysis with 10,000s simulations is not feasible. We consider OPM-DIANA a valuable tool for the understanding of stressing mechanisms around doublets and assessment of fault reactivation potential, when geometry, flow and mechanical parameters are more constrained based on location-specific data and results are validated against monitoring data.

Results from the 3D analysis in OPM-DIANA confirms the observation in SRIMA that higher stiffness of seal and base formations promotes fault reactivation and results in larger stress changes over a larger fault length. The 3D model in OPM-DIANA enables modelling the effect of the increasingly asymmetric cooling front with increasing operation time, growing preferentially in the direction of the production well. Results show that a significantly larger fault area experiences cooling and stressing when wells are oriented perpendicular to the fault and located on either side of the fault, then for a doublet oriented parallel to the fault (which in practice is the default doublet design).

Even though the stress changes computed in the three model approaches are significant and could well lead to fault reactivation, this does not necessarily mean fault reactivation leads to felt events or even seismic events at all. Fault rock properties can be such that faults are reactivated aseismically, which is typical for clay-rich or non-cohesive sedimentary fault rock materials. Also the interaction of the cooling front with the fault may cause fault reactivation to occur progressively, in smaller events, as more and more of the fault area gets cooled. Such a gradual increase of perturbed fault area and gradual release of seismic energy with time could be favorable for mitigation of felt seismic events, as it increases the chance of detecting seismicity (and potentially unmapped faults) by seismic monitoring networks well before large fault segments are perturbed by the cooling front. Furthermore, irregular fault geometry and the layered sedimentary stratigraphy may cause both the initial stress and the induced stresses to vary significantly, which is also expected to lead to smaller, more localized events, instead of larger events.

We **recommend** future research should focus on the thermo-mechanical characterization of reservoir rocks and seal and base rocks (Young's modulus, thermal expansion coefficient), the fault properties (cohesion, dynamic weakening, geometrical variations) and the in-situ stress field, as these are fundamental for constraining the amount of stress change, the potential of fault reactivation and seismic rupture. Both the experimental and in-situ stress characterization of the reservoir rocks is part of the WarmingUp project and will be reported in a separate document. However, additional data based on newly available samples and field studies will be needed to update our knowledge of the mechanical and stress conditions at the geothermal sites. We here emphasize the added value of seismicity monitoring networks, both for mitigation of felt seismic events and to validate tools developed here against field data, enabling testing and improvement of the main model assumptions.

2 Introduction

The Dutch National Climate Agreement sets the goal to adapt before 2030 1.5 million homes which are now heated by natural gas, into buildings heated by sustainable heat. To this end, a growth of the use of sustainable heat sources needs to be realized. Geothermal energy is considered an important future heat source, with an expected supply of 15 - 50 PJ in 2030 of sustainable heat to district heat networks and greenhouses (Stichting Platform Geothermie et al., 2018, PBL et al., 2020). Theme 4 in the WarmingUp project aims to accelerate and upscale geothermal development for sustainable heating in the built environment.

For safe and effective application of geothermal energy, it is important to assess the effects of geothermal operations on the potential of induced seismicity. Work package 4B specifically focusses on the quantification and management of risks related to induced seismicity and other environmental effects. The activities in this work package comprise:

- Development of methods, tools and workflows for analysis of stress changes and assessment of induced seismicity during geothermal doublet operations
- Development of practical, cost-effective monitoring techniques for monitoring and mitigation of seismicity and other environmental effects, such as loss of reservoir seal integrity and leakage to groundwater.

In the present report we address the topic of induced seismicity modelling; the main objective is to develop practical methods and modelling workflows for fault reactivation potential and seismic hazard assessment in conventional geothermal systems (as part of WP 4B1 Induced seismicity - Processes and model chain and WP 4B2 Induced seismicity - PSHA workflow). We test and demonstrate the workflows for representative geological and operational settings in the Netherlands. The methods and workflows can be used as a base for guidelines and criteria for field development, in combination with field data and monitoring data to validate the models. Results on monitoring techniques (WP 4B3 Monitoring and control) will be reported in a separate document.

Geothermal heat in the Netherlands is commonly extracted from brine, which is produced from hot porous sedimentary aquifers, whereas only a limited number of geothermal systems directly target fault zones in fractured (Dinantian) carbonate systems. Current and planned geothermal doublets (will) mostly produce from aquifer rocks of Tertiary, Cretaceous/Jurassic, Triassic and Permian age (Buijze et al., 2019). Geothermal energy production is generally executed using a geothermal doublet system, which consists of an injector and producer in combination with a surface heat exchange facility. Production temperatures of the conventional doublets vary with depth and region, but are commonly between 65-100°C, whereas fluids are re-injected at temperatures between 20 – 45 °C. As the volumes of fluids produced and re-injected is balanced, reservoir pressure changes are expected to be limited and to occur in the near-well area. The long-term re-injection of cold fluids over the lifetime of a geothermal installation will however lead to a gradual, but progressive and significant cooling of the reservoir rocks and (more limited cooling) of burden. This cooling of reservoir and burden causes thermal contraction of the rocks and associated thermal stresses. Particularly doublets drilled in competent rocks and marked by large temperature contrasts (both increasing with depth) are prone to a high likelihood for the buildup of significant thermal stresses over time. These thermal stress changes, superimposed on the pressure-induced stress changes, may affect and jeopardize fault stability within reach of, and close by the thermal front and potentially induce seismicity.

We present three modelling workflows for the assessment of pressure and temperature and stress fields and related fault reactivation and seismicity:

- A stochastic fast model for the assessment of the transient evolution of pressures, temperatures, associated stress changes and fault reactivation around an injection well (SRIMA)
- A stochastic fast model for the assessment of cooling-induced fault rupture (PANTHER2D)
- A dynamic reservoir model coupled to a 3D finite element model for the assessment of pressures, temperatures, associated stress changes and fault reactivation near a geothermal doublet (OPM-DIANA FEA)

The first two are (semi-)analytical 'fast' models, which provide first-order estimates of fault stability and fault rupture. SRIMA provides first-order estimates of the pressure and temperature field around an injection well for varying flow and thermal parameters. It enables analysis of the extent and shape of the pressure and temperature front and its impact on fault loading and reactivation. PANTHER2D particularly assesses the process of fault reactivation, nucleation of seismicity and fault rupture. Both models are fast and allow for stochastic analysis and can be used to provide insights into the key factors that drive the potential of fault reactivation and seismicity during geothermal operations. However, in order to be fast and allow for the analytical calculations both models have also made several simplifying assumptions that could affect fault reactivation. As both fast models are based on stringent conditions for the geometry of the model domain, they are less well suited for cases where geological complexity, heterogeneities and spatially varying pressure and temperatures are expected to be important. To understand the impact of such heterogeneities with respect to more simplified conditions OPM-DIANA FEA can be used. In the current study a number of these heterogeneities are evaluated in a generic model, which gives insight in the potential importance of including these aspects, with respect to more simplified input. For site-specific research the model could be informed with field-based data such as fault geometries, stiffness contrasts, a heterogeneous permeability field etc. Note however that OPM-DIANA FEA will be too computerintensive to evaluate a large number of scenarios and thus capture the large uncertainties that are inevitably present. It is therefore complementary to faster, simpler tools, as PANTHER and SRIMA, but also MACRIS which does capture 3D effects and heterogeneous fault geometries (Candela et al., 2019, van Wees, 2020). In all cases, model validation against field data is key.

In this study, we compare results between SRIMA, PANTHER2D and OPM-DIANA FEA. We investigate for which specific cases we can use the software tools for fault reactivation and seismicity assessment during geothermal doublet operations, and what the limitations for use are. In addition, we used the above three modelling workflows to address the following questions:

- What are the key factors that drive fault reactivation in geothermal doublet operations in porous sedimentary formations as targeted in the Netherlands?
- What is the extent of the cooling front and the critically perturbed zone, and what does that mean for the safe distance of the injection well to faults?
- What are the differences between cooling-induced and depletion-induced fault reactivation and seismicity? What mechanisms are driving fault reactivation and seismicity due to cooling (geothermal) and depletion (e.g. gas production) and what are the consequences for fault reactivation and induced seismicity?

2.1 Geothermal target formations in the Netherlands

In all three model approaches relatively simple generic reservoir and fault geometries are used to study the basic mechanics of fault reactivation around geothermal doublets. The reservoir depth and input parameters are based on those relevant to geothermal doublet operations in the Netherlands and similar settings. Geothermal energy in the Netherlands is produced from relatively shallow (0.8)

- 3.5 km), permeable sedimentary formations. Most of the geothermal targets are situated in tectonically inactive rift basins, with a normal geothermal gradient with an average of 31 °C per km. As mentioned above, geothermal energy is produced from geothermal doublets, where water is injected into an injection well and produced from a production well, using a balanced injection scheme. Currently, more than 20 doublets are operational in the Netherlands, mainly in the southwest and center of the Netherlands (Figure 2-1). Due to the relatively low temperature (< 100°C) the heat that is produced is for direct-use purposes such as agriculture and district heating; no electricity is currently produced in the Netherlands.

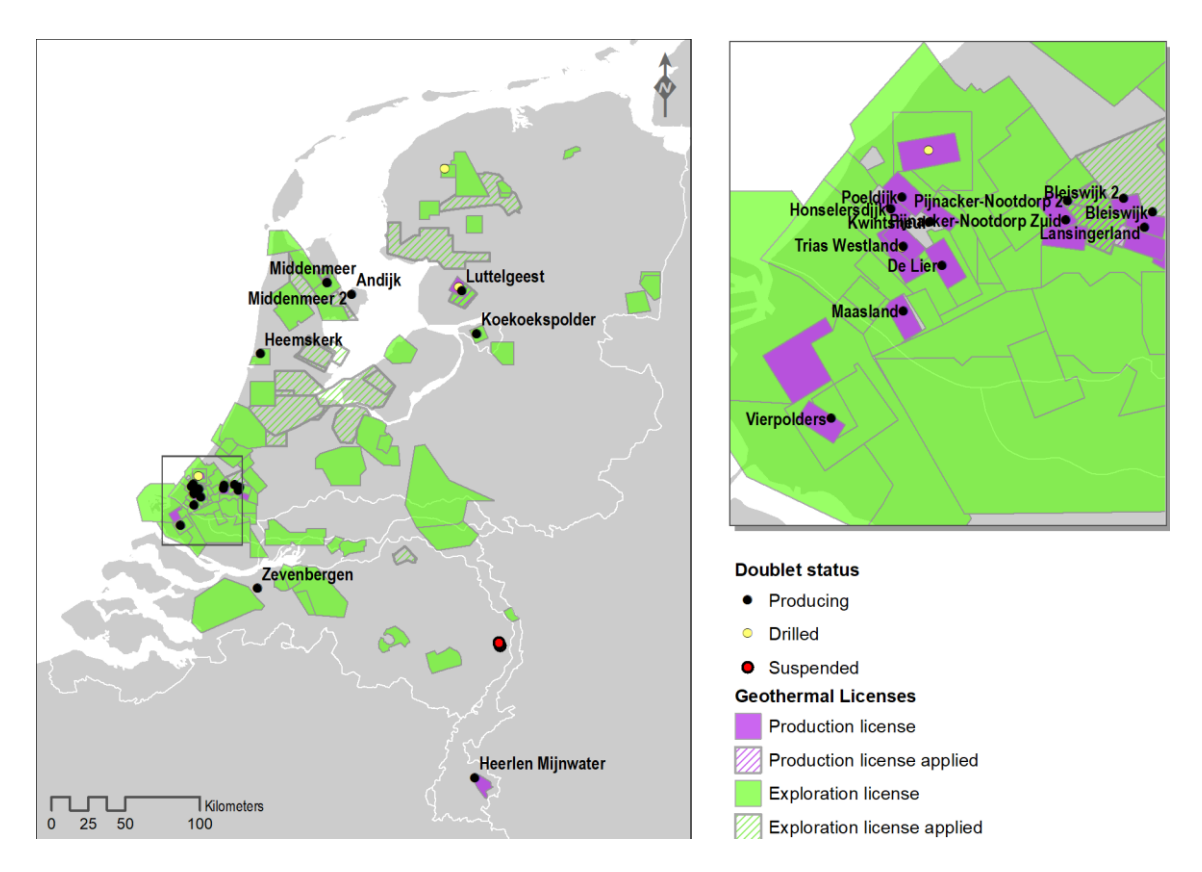


Figure 2-1 Geothermal licenses and doublets in the Netherlands. Licenses and locations drilled wells from www.nlog.nl.

These existing doublets target a number of sedimentary formations, which are briefly summarized here (see Mijnlieff, 2020, Willems et al., 2020 for more elaborate descriptions)

- Tertiary sandstones. These are present nearly everywhere in the Netherlands, and are mostly located at shallow depth (0 1.3 km) and poorly consolidated. Because of their shallow depth the reservoir temperatures are low (<40°C). One doublet is currently operating in the Tertiary (Zevenbergen).
- Lower Cretaceous: The main formation targeted for geothermal operations is the Vlieland Sandstone Formation of the Rijnland Group, which contains the productive Berkel and Rijswijk sandstone members. Both of these are marine sandstones These geothermal target formations have favorable depths and temperature in the southwest (West Netherlands Basin) and potentially other regions of the Netherlands, with temperatures between 40 100 °C and depths 1.5 3 km. Just a few of the earlier doublets target these formations as the underlying Upper Jurassic formations turned out to have better permeability.
- Upper Jurassic: the main formation targeted for geothermal production is the Nieuwerkerk Formation of the Schieland Group. Its main productive member is the Delft Sandstone Member. This member is characterized by fluvial sandstones with a high net-to-gross (30 – 60 %) ratio (Willems et al., 2020). The Delft Sandstone Member is underlain by the

Alblasserdam Member, which consists of fluvial sandstones interbedded with clay layers, with a much lower net-to-gross ratio. Most of the doublets in the West Netherlands Basin target the Delft Sandstone Member, which is located at 1.5-3 km depth, has a temperature of 50-100 °C, porosities between 15-20% and permeabilities 50-4000 mD.

- Triassic: Another geothermal target is found in the Main & Lower Buntsandstein Sub-Groups of the Lower Germanic Trias Group, with the Nederweert sandstone and Volpriehausen, Dethlingen, and Hardegsen Formations, a succession of clays and terrestrial sands. Favorable conditions are encountered at the margins of the West Netherlands Basin. However, the potential is much lower than that of the Jurassic/Cretaceous formations as the transmissivity is much lower. One doublet is currently producing from these formations.
- Permian: Another major geothermal target formation is the Slochteren Formation of the Rotliegend Group. The Slochteren Formation is comprised of terrestrial sandstones up to 200 m thick. Favorable conditions are found in the central Netherlands area around the Texel-IJsselmeer High; here the Slochteren Formation lies at depths 1.5 3 km, with temperatures of 60 to over 100 °C. Permeabilities are generally lower than those of the Jurassic/Cretaceous formations (50 500 mD), but thicknesses are a bit larger (up to 230 m).
- Lower Carboniferous: fractured carbonate formations located in the Ruhr Valley Graben in the southeast of the Netherlands (e.g. ter Heege, 2020). Two doublets were operational in this formation but have been suspended due to problems with the injection well and the potential risks of seismicity.

Note that for none of the doublets operation in these formations felt induced seismic ($^{\sim}M > 2$) events have been recorded to date. Microseismic events with magnitudes up to M 1.7 were recorded near the doublets targeting the Upper Carboniferous where a microseismic monitoring array was present (see e.g. ter Heege, 2020). No recorded events have been published for the doublets in the sandstone formations, though only recently the seismic network was improved in the southwest of the Netherlands.

In this report we focus on the potential for fault reactivation and fault slip due to geothermal operations in the sandstone formations. An overview of the characteristics of the currently active doublets targeting these different geothermal formations is shown in Figure 2-2. Temperatures fall between 60 and 100 °C for depths of 1.7-2.6 km, which corresponds to thermal gradients of 24-38 °C/km (assuming 10°C surface temperature). Permeabilities range from several 10's of mD to over 1000 mD. The thickness of the geothermal target formations is 80-220 m. Note however that the more permeable streaks in these formations may dominate the flow behavior.

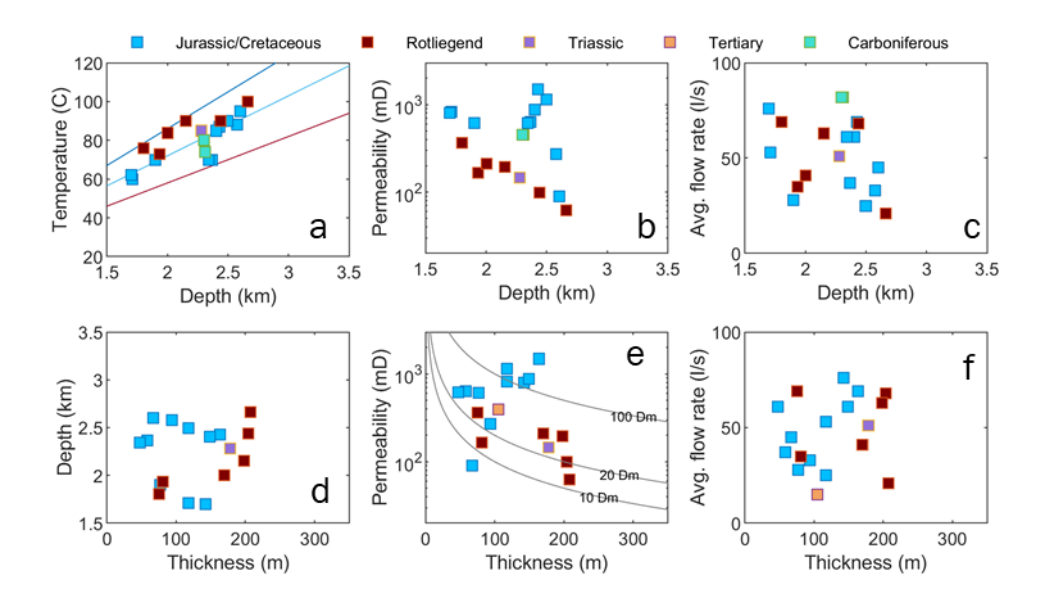


Figure 2-2 Properties of existing geothermal doublets in the Netherlands. Apart from the projects in the Carboniferous, all projects target various sandstone formations (geological age indicated in the legend). Temperature, permeabilities, depth and thickness were taken from well reports on www.nlog.nl or ThermoGIS, average flowrate is the annual average (data from www.nlog.nl). Thickness for the Jurassic targets is that of the Delft Sandstone only (excluding the Alblasserdam Member). In a) the range of thermal gradients (24 – 38 °C/km) is shown, and in e) transmissivity values (thickness x permeability) are shown.

3 Stress changes and fault reactivation around an injection well: a fast model

3.1 Abstract

Fault reactivation, which is at the cause of induced seismicity, is driven by stress changes induced by changes in temperature and pressure. Large unknowns are usually associated with the chain of physical processes. Therefore, it is important to be able to map the bandwidth of unknown process parameters to reactivation risks. A fast model that can be run with probabilistically distributed parameters is extremely useful when such a task prevails. This Chapter describes SRIMA (Seal and Reservoir Integrity Mechanical Analysis), a fast semi-analytical tool that helps the user perform this task. For a simplified geometry (radially symmetric) and injection scenario, it allows to map the reactivation risk associated to different injection scenarios and different values of the possible characterizing subsurface scenarios. We demonstrate how to target safe operations with a typical example. Furthermore, based on stochastic analysis, we derive key factors that drive the potential of fault reactivation. Summary of main results:

- For the case that we evaluate in this report, the most critical input is related to the initial stress situation. If the stress is already critical or close to it, injection of cold water will quickly induce exceedance of the criticality measures in a large part of the reservoir. The initial shear failure capacity is determined by an interplay between the initial stresses, the overpressure of the reservoir, and the failure parameters.
- When the initial shear failure capacity of the system is moderate or low, the expected radius
 of criticality mostly does not extend more than 30% beyond the thermal front
- The second largest effect is related to the magnitude of the thermoelastic stress perturbations. These are mainly related to the temperature difference between injected fluid and the virgin reservoir, the thermal expansion coefficient, and the elastic modulus. Additionally, the modulus contrast between seal and aquifer is important, in particular in the case of a stronger seal. In that case, stress concentration develop in the bounding layers due to their larger resistance against thermo-elastic deformation. Even tensile stresses may develop, with the risk of inducing hydraulic fractures in the seal.
- We consider SRIMA a valuable tool for the evaluation of induced stresses and associated fault reactivation risk measures. Sensitivities can be identified quickly and the key parameters determined.

3.2 Introduction

The safety of geothermal operations in matrix-type reservoirs requires that injected water remains in the target aquifer to which it was injected and that seismicity is minimized. This implies first of all that the integrity of the seal must be safeguarded. Hydraulic fracturing is a phenomenon that can breach this integrity, and it must thus be prevented. Furthermore, fault reactivation or shear fracturing should be prevented as it may induce seismicity and promote flow due to dilatancy. Both hydraulic fracturing and fault reactivation depend directly on the in-situ stresses and the pore pressures. The assessment of the risk of integrity and seismicity issues therefore requires knowledge of the pressure and stress development in the reservoir, the seal and the base.

The pressure and stress in the reservoir and in adjacent layers change upon the injection of water. Two main phenomena must be incorporated. In the first place, injecting the water requires elevated pressures. These alter the total stresses through the poro-elastic effect, and the effective stresses through the pressure change itself. In the second place, injected water of a temperature different

from the in-situ temperature cools or heats the reservoir and its surroundings (heating takes place when heat storage is employed). The temperature change induces a change of the total stress. As long as the stresses remain below the yield envelope of the material these changes are poro-elastic and thermoelastic. An assessment of the stresses due to the injection of non-isothermal water therefore requires a calculation that consists of the temperature and pressure distribution in, above and below the reservoir, and the effect of those fields on the in-situ stresses.

Knowledge of subsurface processes and rock, fault, and stress parameters is commonly marked by large uncertainties. Additionally, many different operational decisions can be envisaged in specific circumstances. Therefore, there is a need for estimation methods which are fast and flexible. Such methods are provided by analytical or semi-analytical means. The present chapter targets such solutions. We have devised semi-analytical correlations for the ingredients of a stress assessment as described in the previous paragraph. The correlations have been benchmarked using comprehensive numerical modelling software. This validation and benchmark exercise is briefly described in the Appendix; a publication that fully describes the details is in preparation.

In the following we will first describe the semi-analytical approach that we developed and their validation. Then we present an example of fracturing and reactivation risk assessment and the sensitivity to different parameters and operational choices. We constrain ourselves to normal faulting regimes (as prevalent in the Netherlands) and strike-slip faulting regimes. The minimum insitu stress is then horizontal and hydraulic fractures will develop vertically. We close this chapter with a discussion of the work in the present state and an outlook to the future.

3.3 Method

In this section we briefly describe the semi-analytical tool SRIMA (Seal and Reservoir Integrity Mechanical Analysis). For the background of the equations we refer to Appendix A. A benchmark of the pressure and temperature calculation, as well as the poro-thermo-elastic stress calculation, is presented in the same Appendix.

SRIMA is a fast semi-analytical tool that helps the user perform quick mechanical calculations and based on that assess the possibility of fault reactivation and hydraulic fracturing. The tool has been developed for a radially-symmetric reservoir where fluid is injected in the well in its center (Figure 3-1). Three layers are present: the permeable layer in which the injection takes place, and the overlying and underlying, low-permeability layers. As a consequence, pressure and temperature fields are also radially symmetric. Injection is supposed to take place evenly over the complete height of the aquifer, and to result in pressure and temperature fields independent of the vertical position in the aquifer. In the aquifer, flow is modelled under steady-state conditions and heat transport is assumed to take place by convection only. In the bounding layers both pressure and temperature are supposed to be controlled by diffusion. The temperature solution has been published earlier; we use the formulation by Candela et al (2018). The steady-state solutions for the pressure in the aquifer are standard reservoir engineering knowledge (see, e.g. Dake, 1978) and have been complemented by an approximate solution to the diffusivity equation in the bounding layers. The solutions have been formulated for a single period of injection at a constant rate.

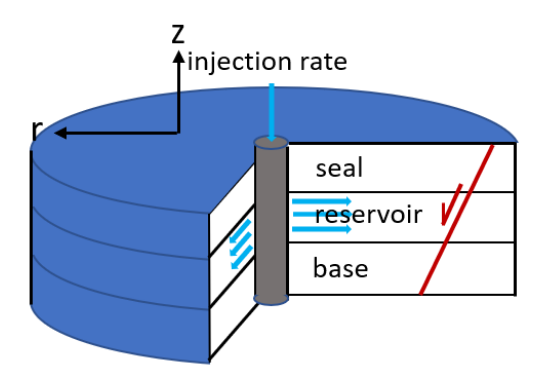


Figure 3-1 Radially-symmetric geometry used in SRIMA for analysis of thermo- and poroelastic stresses in a reservoir caused by injection of cold fluids. Injection is assumed to take place over the entire reservoir height. Stresses are computed on a polar coordinate system and then transferred to a Cartesian coordinate system. The stress tensor is then used to compute stress changes, e.g. on a single fault (presented in red).

SRIMA does not consider wellbore stability. The mere presence of the well already changes the stress distribution around it (Busch et al., 2010). Since we focus on hydraulic fracturing and fault reactivation in the reservoir and seal we discard the stress concentrations at the wellbore. Therefore we consider cylindrically shaped regions with elevated or decreased pressures and temperatures. Analytical solutions are available for those (Myklestad, 1942, Perkins & Gonzalez, 1985). These solutions have been developed for single cylinder with uniform pressure or temperature change, and a step change at the interface. We discretize the pressure and temperature fields using 10 cylinders, each with a temperature or pressure change 0.1 of the total pressure and temperature change, with radii corresponding to the location where the pressure or temperature changes is 0.1, 0.2, etc. of the total pressure change. The stress solutions of the 10 cylinders are superimposed to yield the full stress field

The goal of the calculation is to assess the possibility of fault reactivation or hydraulic fracturing. The stresses must be evaluated in the light of failure criteria. There are different possibilities to define a measure for the reactivation risk. A first one is exceedance of the Mohr-Coulomb failure criterion on an existing fault. The criterion is formulated as a shear stress τ causing failure when it exceeds the failure envelope, which is defined as a linear function for the effective normal stress $\sigma_n{}'$ at the fault:

$$\tau = C + f_s \sigma_n'$$
 3-1

with static friction coefficient f_s and cohesion C. The activation risk measure has been quantified as the shear capacity utilization (SCU) for that fault, defined as the ratio between actual shear stress τ and the shear stress at failure for the actual effective normal stress at the fault:

$$SCU = \left| \frac{\tau}{C + f_s \sigma_n'} \right|$$
 3-2

Faults with a SCU larger than unity will be reactivated.

A second measure is the exceedance of the failure criterion for the fault orientation that is most critically oriented. The SCU then is calculated for the fault orientation that is most prone to failure. The calculation does not require stresses for all possible orientations; it suffices to determine the principal stresses and the associated shear capacity of the rock, which is a measure for the proximity of the Mohr circle to the failure envelope. Failure will occur if the value for the SCU is larger than unity. The measure is defined locally.

A third measure is the radius up to which failure on optimally oriented faults occurs. It can be calculated by defining the maximum distance from the wellbore at which the shear capacity utilization exceeds unity. The measure can be employed as a standalone measure or in conjunction with the position of the cooled front.

Finally, a fourth measure can be formulated as the percentage of possible fault orientations which are critical (Levandowski, 2018). The method to calculate this number is to calculate the criticality

for a large number of evenly distributed fault orientations. This measure is a local measure. It can therefore be used to map the spatial distribution or in conjunction with the position of the cooling front.

Our knowledge of many subsurface properties is subject to large uncertainty. Examples are the virgin stress field and the elastic properties of the reservoir and the bounding layers. Further, different choices can be made for operational parameters. A prime example is the injection temperature. All these parameters have a profound influence on the reactivation potential. The measures defined in the previous paragraphs therefore commonly need to be defined for a range of parameter values. The approach that we take is that we first define the parameters subject to considerable uncertainty or variability and their uncertainty or variability range. Within these ranges, N_I values are chosen randomly — simultaneously for all parameter ranges identified. This creates an ensemble of N_I realizations of parameter value combinations. For every realization, the temperatures, pressures, induced stresses and reactivation measures are calculated.

An assessment starts with identifying the most influential parameters. This is done by determining the correlation between the scaled input parameter and the scaled reactivation measure. For every measure, then, these are sorted and plotted in order of magnitude. The correlations with the largest absolute values are the most influential ones.

Secondly, for every variable input parameter, the ensemble members are divided into a number of subranges, or input range bins. Clearly, different input parameters result in different subranges for these bins. For every input range bin, then, every output measure is also divided in bins. These combinations can then be plotted in a bar graph to gain insight into the effect of the parameter input value on the output measure for reactivation.

3.4 Results

3.4.1 Representative case

We have formulated a representative case to show the capabilities of the setup presented above, with basically the same input as used in the other Chapters of this report and in the Appendix. The parameters are summarized in Table 3-1. Differences with the other Chapters are that (i) a throw cannot be modeled in SRIMA as it assumes fixed depth and reservoir thickness, (ii) only a single value for the dip is used as the activation of a specific fault is not part of the probabilistic evaluation, (iii) dynamic friction and critical slip-weakening distance are no input in SRIMA; (iv) only a single mass injection rate is modeled because of current limitations of the SRIMA code.

Table 3-1 SRIMA input values – range and default values

Parameter	Symbol	Unit	Range (and default)	
Mid depth	<i>Ymid</i>	m	1500 – 3500 (2300)	
Reservoir thickness	h	m	30 – 220 (100)	
Dip	θ	0	70	
Vertical stress gradient	$\Delta \sigma_{\nu}/\Delta y$	MPa/km	21 – 23 (22)	
Stress ratio σ_h / σ_v	K_0	-	0.65 – 0.85 (0.75)	
Horizontal stress ratio σ_H / σ_v	σ_H/σ_h	-	1.0 – 1.2 (1.1)	
Strike with respect to σ_H	φ	deg	0 – 90 (0)	
Pressure gradient	$\Delta P/\Delta y$	MPa/km	10 – 11.5 (10.7)	
Overpressure in the reservoir (overpressure not due to saline water gradient)	Pexc	MPa	-2 - 4 (0)	
Temperature gradient	$\Delta T_{res}/\Delta y$	°C/km	24 – 38 (31)	
Temperature at surface	T_0	°C	10	
Biot coefficient	α	-	0.7 – 1 (1)	
Poisson's ratio	ν	-	0.05 – 0.35 (0.2) (for aquifer) 0.2 (for seal)	
Young's modulus	E	GPa	5 – 25 (15) (for aquifer), 3 – 60 (20) (for seal and base)	
Linear thermal expansion coefficient	η	°C -1	$0.5 \cdot 10^{-5} - 2.5 \cdot 10^{-5} (1 \cdot 10^{-5})$	
Static friction	f_s	-	0.50 - 0.70 (0.60)	
Fault cohesion	С	MPa	0-4(0)	
Permeability	k	mD	50-1500 (500)	
Overburden permeability	k _{seal}	mD	3.0 · 10 ⁻⁵	
Mass injection rate	q	kg/s	20 – 125 (70)	
Injection Temperature	T_{inj}	°C	20	
thermal conductivity	K_{rock}	W/m.K	1-5(3)	
Injection water density	$ ho_{\scriptscriptstyle W}$	kg/m3	1052	
Specific heat capacity water	Cfluid	J/kgK	3771 (for a salinity of 10%, Batzle & Wang, 1992)	
Specific heat capacity rock	Crock	J/kgK	850	
Seal density	ρrock	kg/m3	2200	
Injection water viscosity	με	Pa.s	1.2 · 10 ⁻³	
Water viscosity at reservoir T	μ_h	Pa.s	0.50 · 10 ⁻³	
Seal porosity	Φ_s	-	0.1	
Total Reservoir compressibility	Cres	1/Pa	4.0 · 10-10	

Our tool in the first place facilitates the calculation of the total and effective stresses, and the associated failure risk measures, as a function of time at different positions in the reservoir. Defining a grid in the x-z plane, Figure 3-2 gives pressure increase and temperatures after injection times of 2 month, and 1, 5, and 30 years. Figure 3-3 presents the associated effective stresses.

Figure 3-4 presents, for these times and positions, two risk measures defined above: the shear capacity utilization and the share of fault orientations that would be critically stressed at a certain position. This share can only be non-zero if the shear capacity utilization exceeds unity.

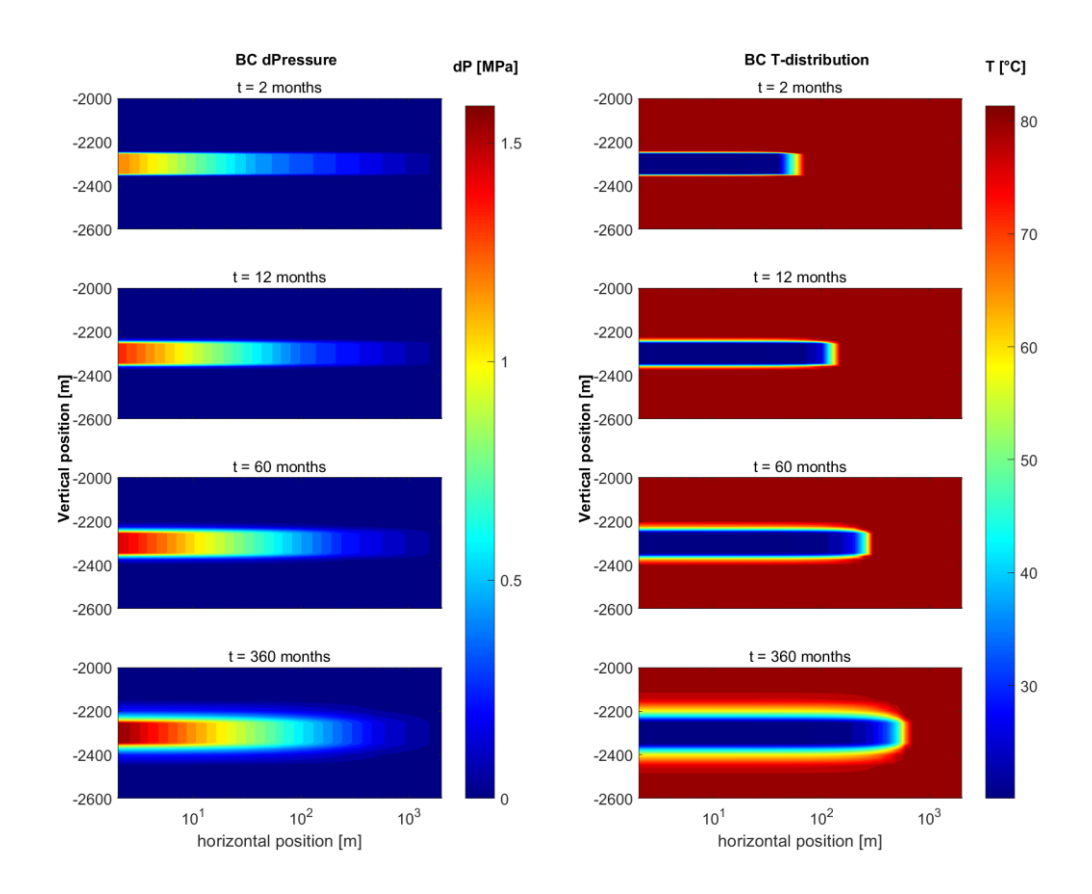


Figure 3-2 Distribution of pressure increase and temperature for the base case (BC). Pressures in the reservoir decrease logarithmically with distance from the injection well, but increase with time due to the growing thermal radius and the associated larger volume with water of larger viscosity. Diffusion of temperature cools the seal and the base with time evolving.

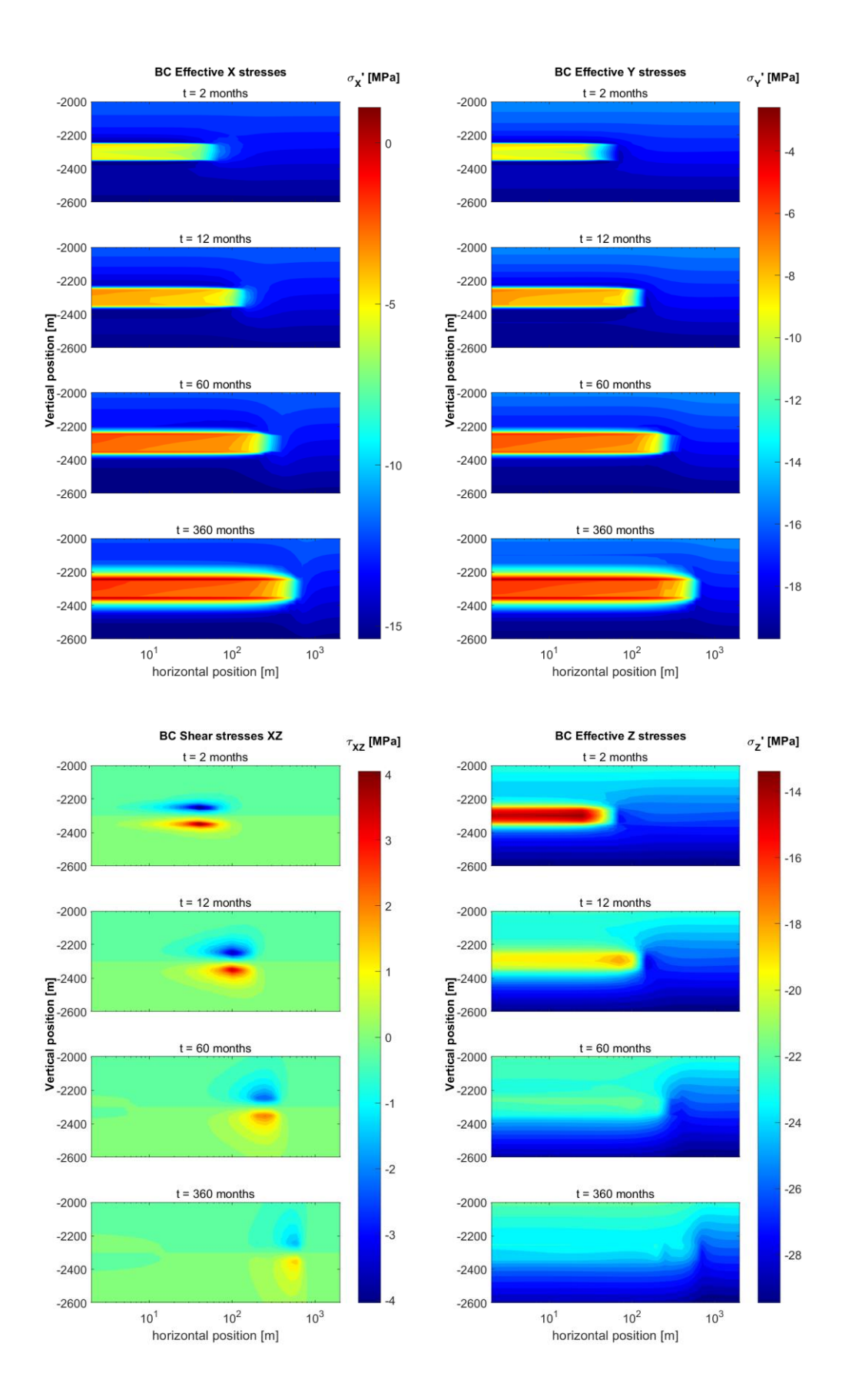


Figure 3-3 Effective stresses associated with the pressure and stress fields of Figure 3-2. The values are given in the x-z plane, so $\sigma_x = \sigma_r$ (with σ_r radial effective stress); $\sigma_y = \sigma_\theta$ (with σ_θ tangential effective stress). Negative normal stresses are compressive.

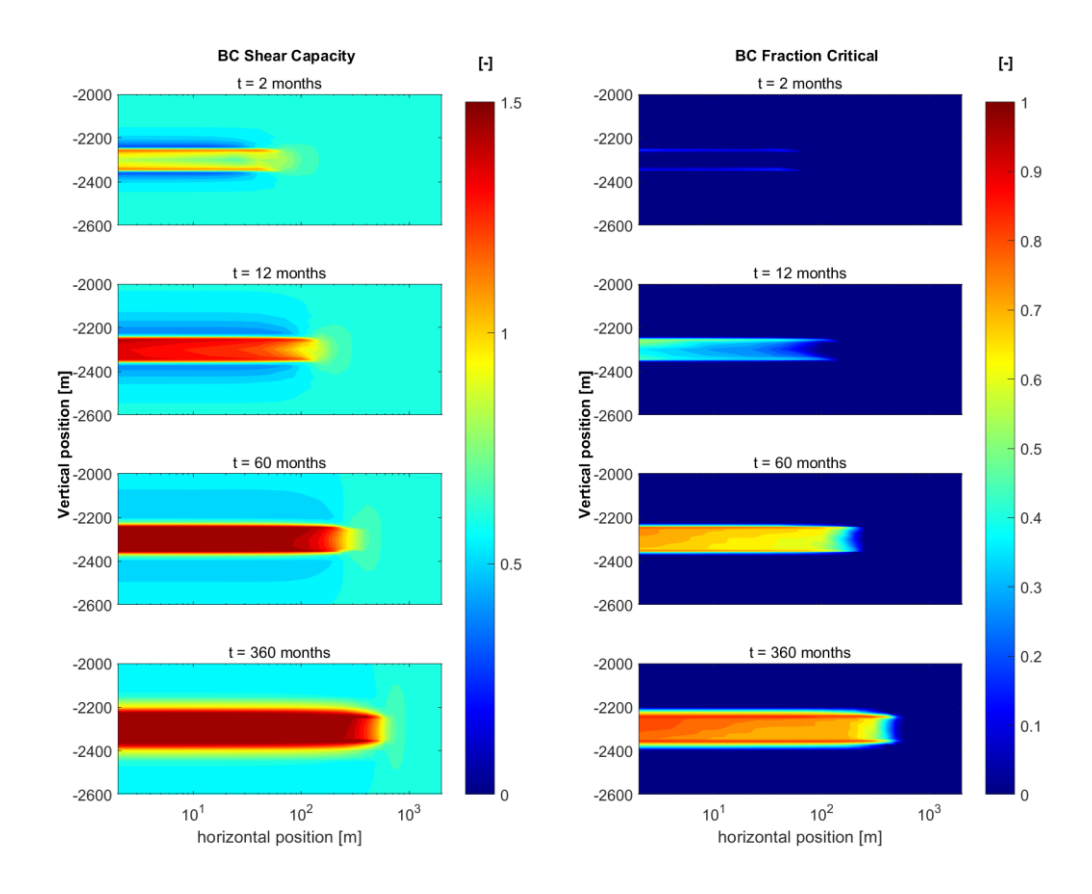


Figure 3-4 Risk measures for the stresses represented in Figure 3-3. The shear capacity indicates how close the most failure-prone fault orientation is to failure; if it is larger than unity, the fraction of critical orientations is larger than zero.

In particular cases the location and orientation of faults is known. In such cases it may be useful to assess the stress development on that fault. This is also possible with the current setup. For demonstration purposes we defined a normal fault 200 m away (at mid reservoir depth) from the injection well, at an angle of 70°.

Figure 3-5 presents the temperature development on the fault between 2 and 7 years after start of the injection. We observe that cooling of the reservoir at the position of the fault starts from the bottom, since the bottom is closer to the wellbore due to the fault inclination. The stresses develop along with the cooling. For a specific fault, the stresses allow direct determination of the normal stresses and shear stresses on it and the associated shear capacity (Figure 3-6).

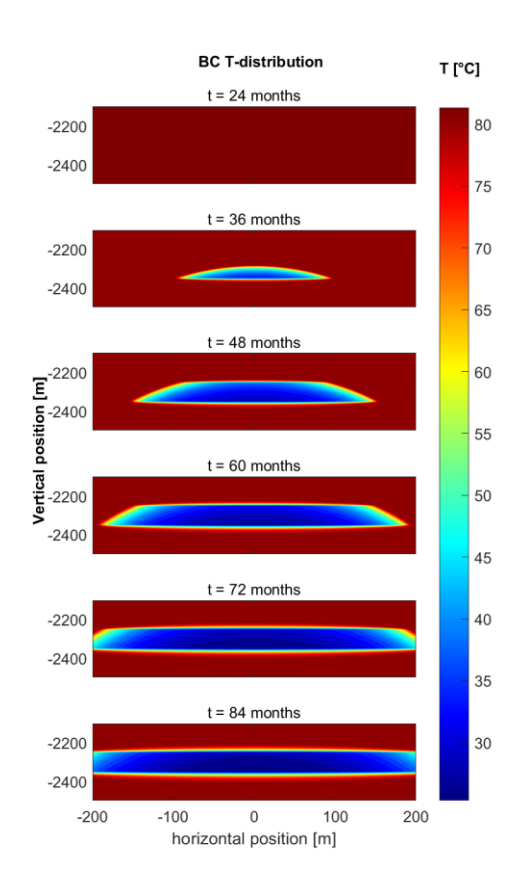
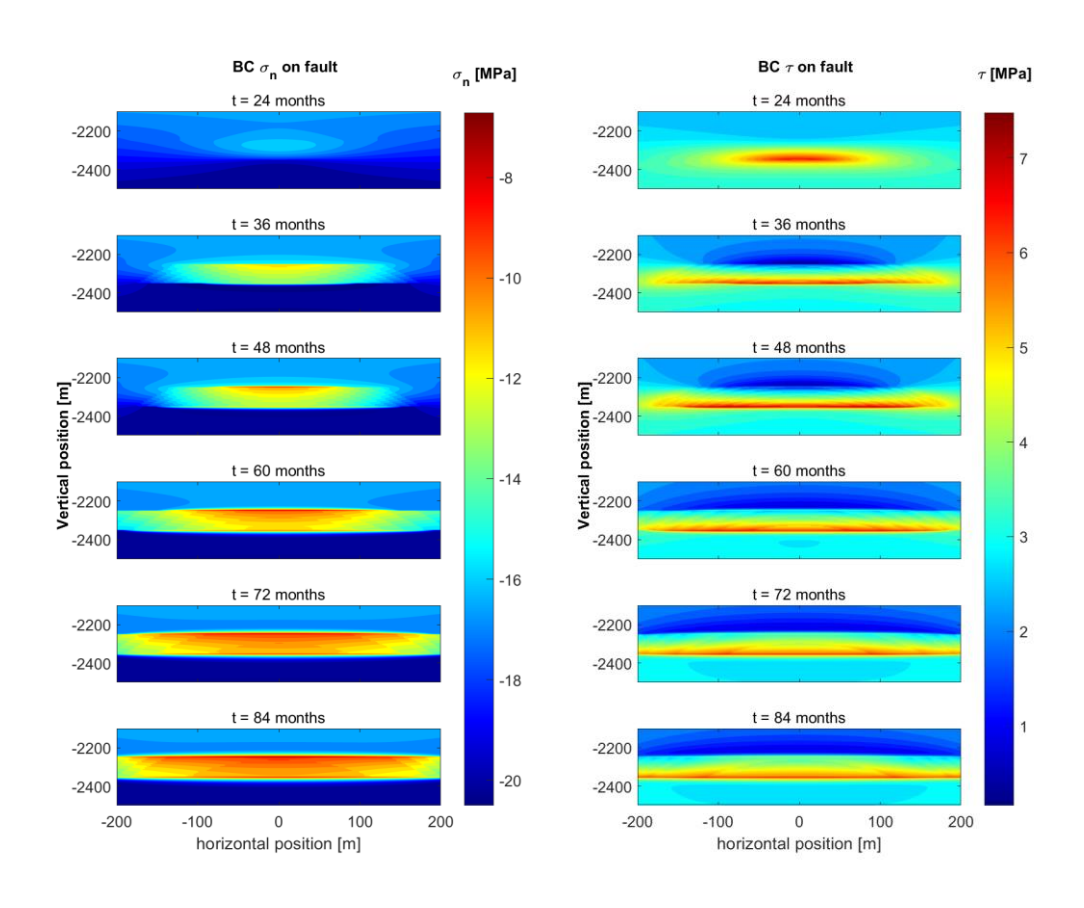


Figure 3-5 Temperature development on normal fault 200 m from injection well



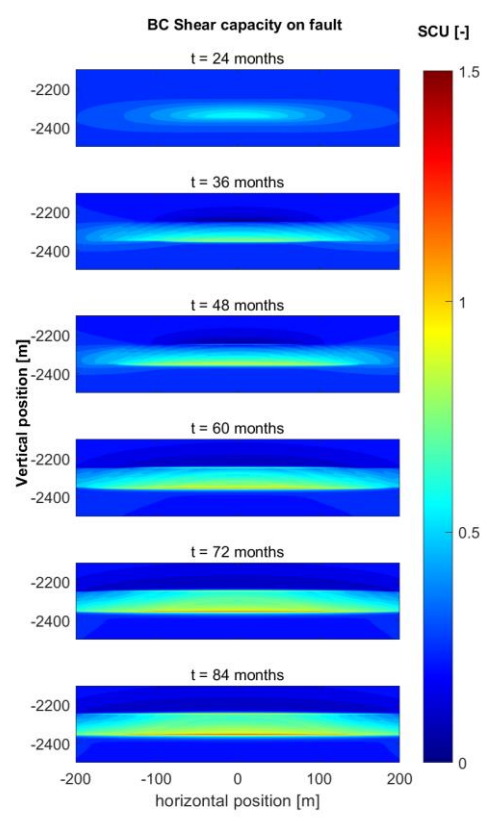


Figure 3-6 Normal stresses, shear stresses and shear capacity on the predefined fault. The size of the critically stressed area allows to make an indication of the maximum size of the reactivation area.

3.4.2 Variable input

Many input parameters in the stress determination are subject to uncertainty. Within the context of thermally induced stresses and failure risk, the most important operational parameters are the injection rate and the temperature of the injected fluid; the most important subsurface parameters are the original in-situ stress and the elastic parameters. The in-situ stresses determine the original criticality of the system: if the horizontal and vertical stresses differ more, the Mohr circle is bigger and the system will enter criticality quicker. The elastic modulus immediately affects the induced stresses; therefore larger moduli will tend to produce reactivation earlier. An additional effect of the elasticity is the possibility of different moduli for the reservoir and the seal and base. The sharp contrast in elasticity across formations induces stress concentrations since the displacements on the interface between these formations must be continuous.

While the effect of injection temperature, stress anisotropy and elastic modulus of the complete system is linear, the effect of an elasticity contrast is more complicated. The base case, with an elasticity ratio of E_{seal}/E_{ag} of 1.3, already induced some stress concentration just across the interface in the bounding layers. We here provide results for a system with a Young's modulus of the seal and base which is larger and which is smaller than the modulus of the reservoir. We apply a factor of 2.0 and 0.67 to the base case parameters presented in the previous Section. The temperature and pressure fields are identical, so we here provide the stress fields and the failure risk measures only. The stress fields (Figure 3-7) show that the larger modulus in the bounding layers induces much larger stress changes in the bounding layers. This results in increased risks, as is also indicated in Figure 3-8, where the Shear Capacity Utilization has been drawn. Note that from the benchmark exercise (see Bijlage A) it was concluded that stresses calculated for the situation with weaker seal and base were not conservative with regard to reactivation risk, and should therefore be assessed with caution. The severity of the Shear Capacity Utilization can further be indicated by the fraction of critical fault orientations, see Figure 3-9. From Figure 3-7 we further see that the resulting stress concentration at the interface even results in positive (tensile) stresses in the bounding layers due to the continued conductive cooling for long times. Hydraulic fracturing of the seal and the base then becomes a risk. The occurrence of tensile stresses have been drawn in Figure 3-10.

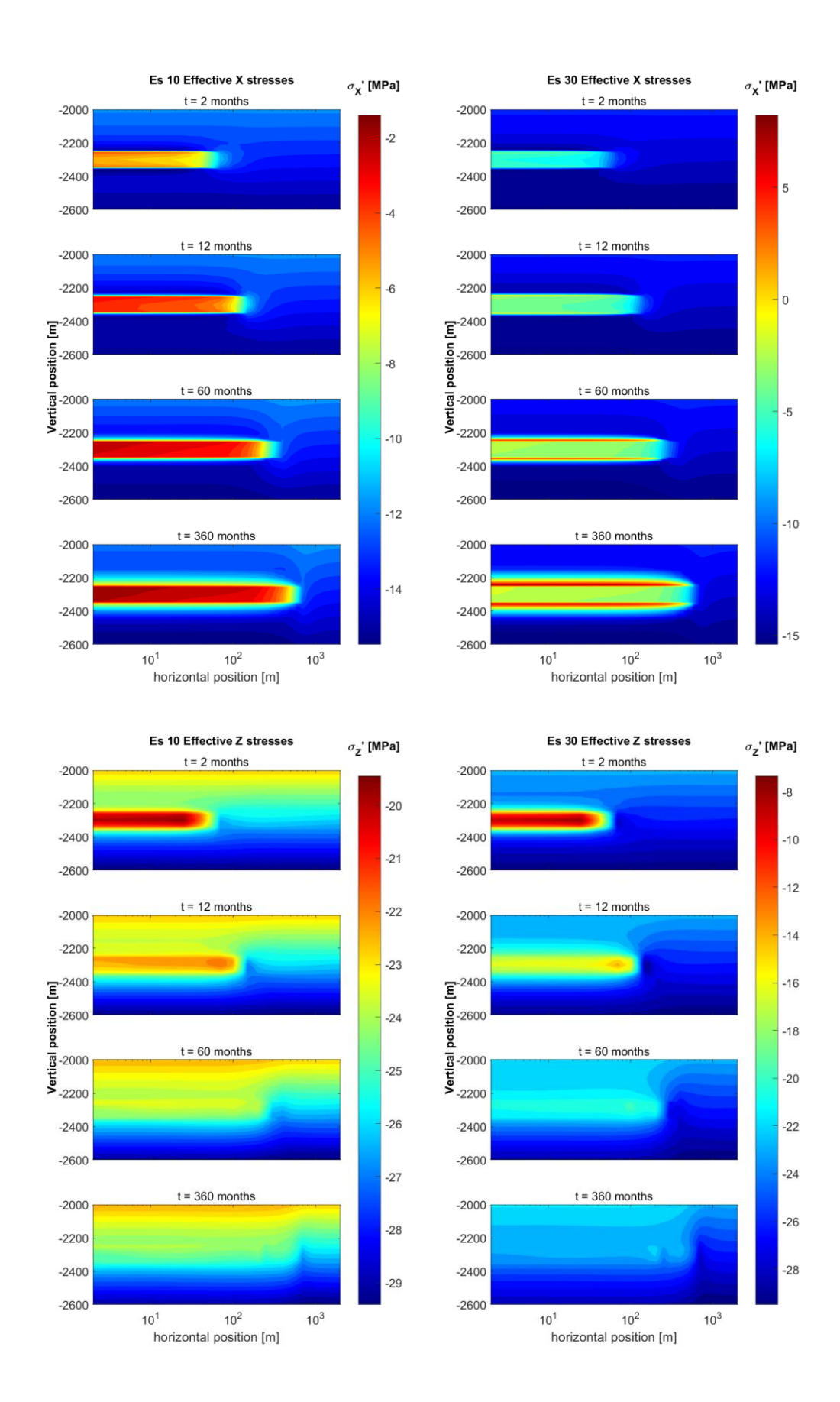


Figure 3-7 Effective horizontal and vertical stresses for an elastic contrast between seal/base and injection layer: modulus ratio of 0.67 (left) and 2 (right). Note the differences in color scale: the larger seal and base elastic moduli result in much larger stress changes. In addition, the larger stresses in seal and base cause stress localization at the interface.

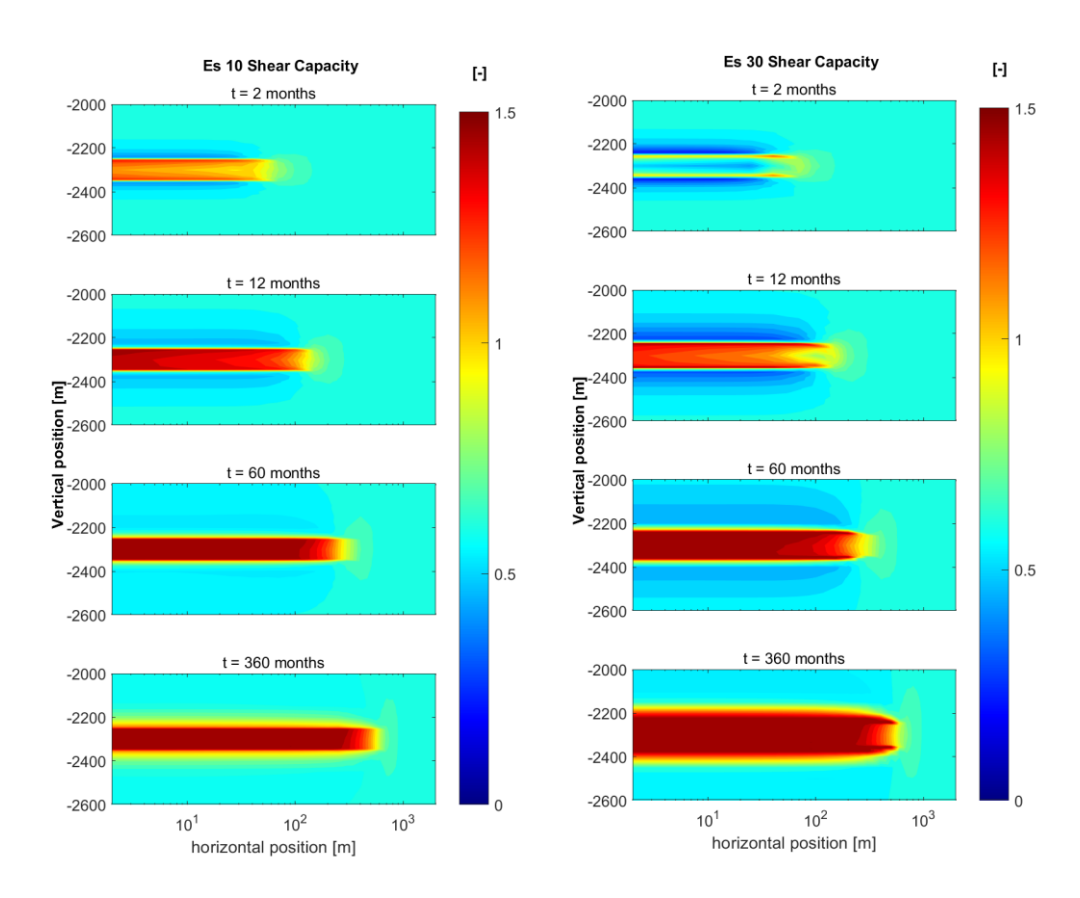


Figure 3-8 Shear capacity for the two scenarios with stress contrast; modulus ratio of 0.67 (left) and 2 (right).

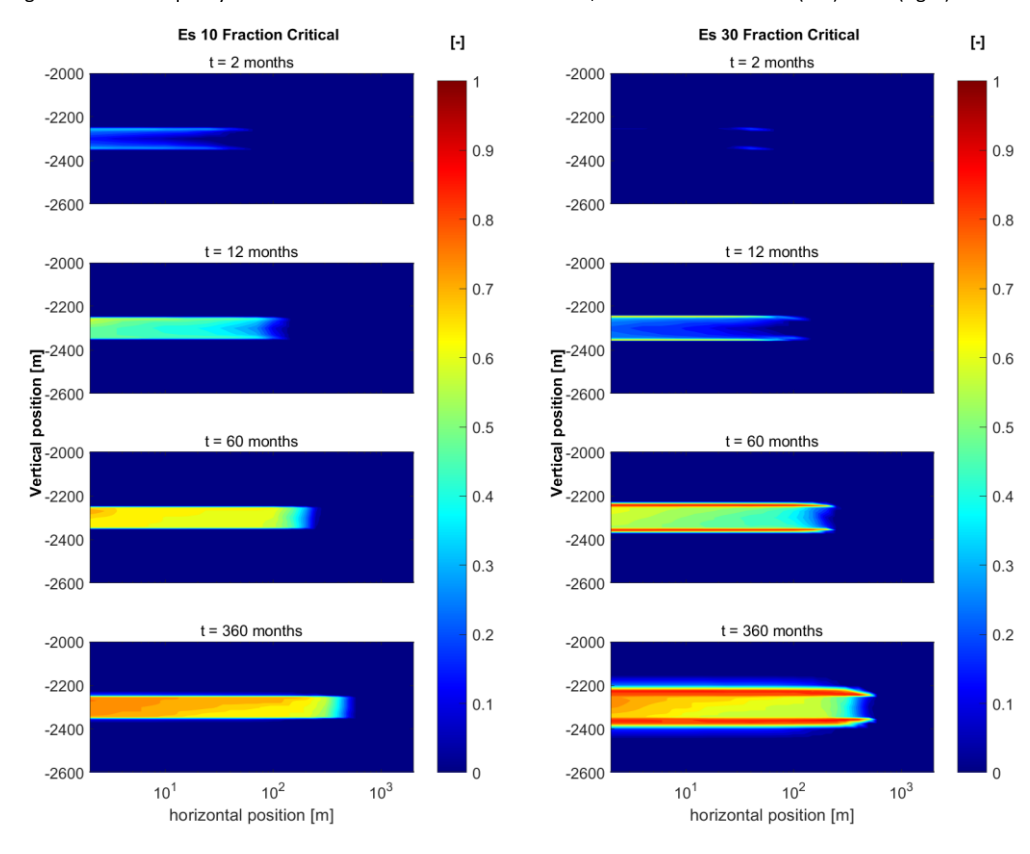


Figure 3-9 Fraction of possible fault orientations that are critical for the two scenarios with stress contrast; modulus ratio of 0.67 (left) and 2 (right).

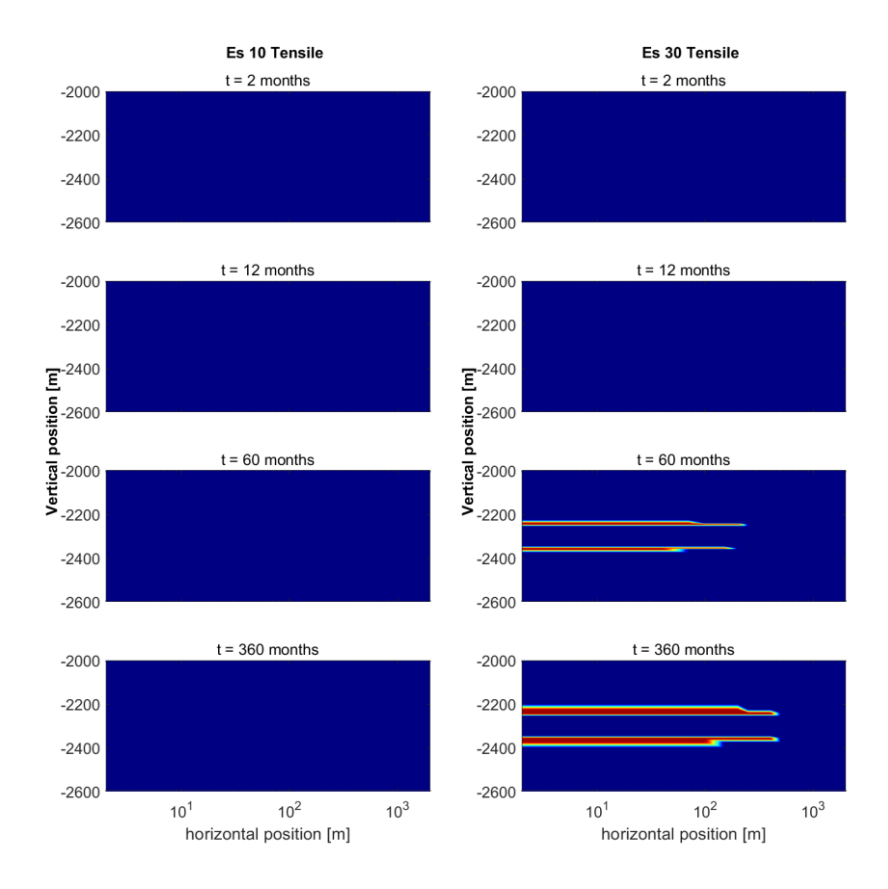


Figure 3-10 Positions where stresses are tensile (red zones) for the two scenarios with stress contrast; modulus ratio of 0.67 (left) and 2 (right).

3.4.3 Probabilistic input

We have also performed a probabilistic study on the uncertain parameters as identified in Table 3-1. The effect of these parameters evolves primarily in the injection layer and just outside it. We have therefore calculated the induced stresses on two horizontal lines: one in the middle of the reservoir, ranging from the wellbore to the reservoir edge, and one at 10% of the height outside the reservoir in the seal. The latter one was chosen because of the sensitivity to the elasticity ratio and the associated stress concentration at the interface that was identified in the previous Section.

An identification of the influence of the uncertain input is provided in Figure 3-11 and Figure 3-12. The first major parameter is the initial stress ratio, K_0 . It determines the initial proximity to criticality and as such how fast criticality is reached upon injection and how far it reaches. Further, the initial pressure (determined by $\Delta P/\Delta y$ and P_{exc}) and the failure parameters (C and f_s) also directly affect the initial criticality. Important parameters for the effect of cooling are the elastic moduli and the thermal expansion coefficient. The effect of the moduli in aquifer and in seal / base are largest in the layer where they apply. In other words, an elasticity contrast due to a stiff seal will mostly affect criticality in the seal.

As an example of the output, Figure 3-13 gives the distribution of the radius of criticality in the aquifer for the different uncertain input parameters. Large effects are associated with, e.g., the elastic modulus in the aquifer and the thermal expansion coefficient, the initial stress ratio, the reservoir overpressure and the cohesion. The elastic modulus in the seal hardly affects the critical behavior in the aquifer. Radii of criticality that are much larger than the radius of cooling only occur for large anisotropy in the stress – i.e. small values of the horizontal / vertical initial in-situ stress and consequently a reservoir that is initially already close to be critically stressed.

As for the criticality in the seal, the sensitivity to the elastic modulus in the seal is striking (Figure 3-14). This is related to the stress concentration in seal and base at the interface, when larger

elasticity contrasts are present. A small elasticity ratio between seal and reservoir alleviates the criticality in the seal.

Figure 3-15 shows the non-scaled radius of criticality in the aquifer, which can, as an example, be an important measure when one needs to determine the minimum distance between an intended well and an existing fault. Some of the values are very large; the share of critical radii larger than 500 m is around 25%. Half of these instances, however, are related to an initial stress regime that is already critical, due to the stress ratio and the initial pore pressure. The remaining instances relate to the cases with small reservoir thickness in which the radius of the thermal front is also considerable: the same volume of injected water must be distributed over a smaller height interval.

The same phenomena are demonstrated with the alternative risk measures. For example, Figure 3-16 presents the distribution of the share of critically stressed fault orientations at the position where the reservoir has cooled to 85% of the temperature difference. The effects are less pronounced than for the radius of criticality.

What is striking in a number of these figures is the absence of certain intermediate color scales. It means that critical radii are either smaller than the thermal-front radius or much larger. The latter is commonly the case for situations where the stress is already critical or almost critical at virgin circumstances. This stresses the need for a thorough data-finding exercise before doing any operations. The current probabilistic analysis can help steer the direction of this exercise since it enables identification of the most influential parameters.

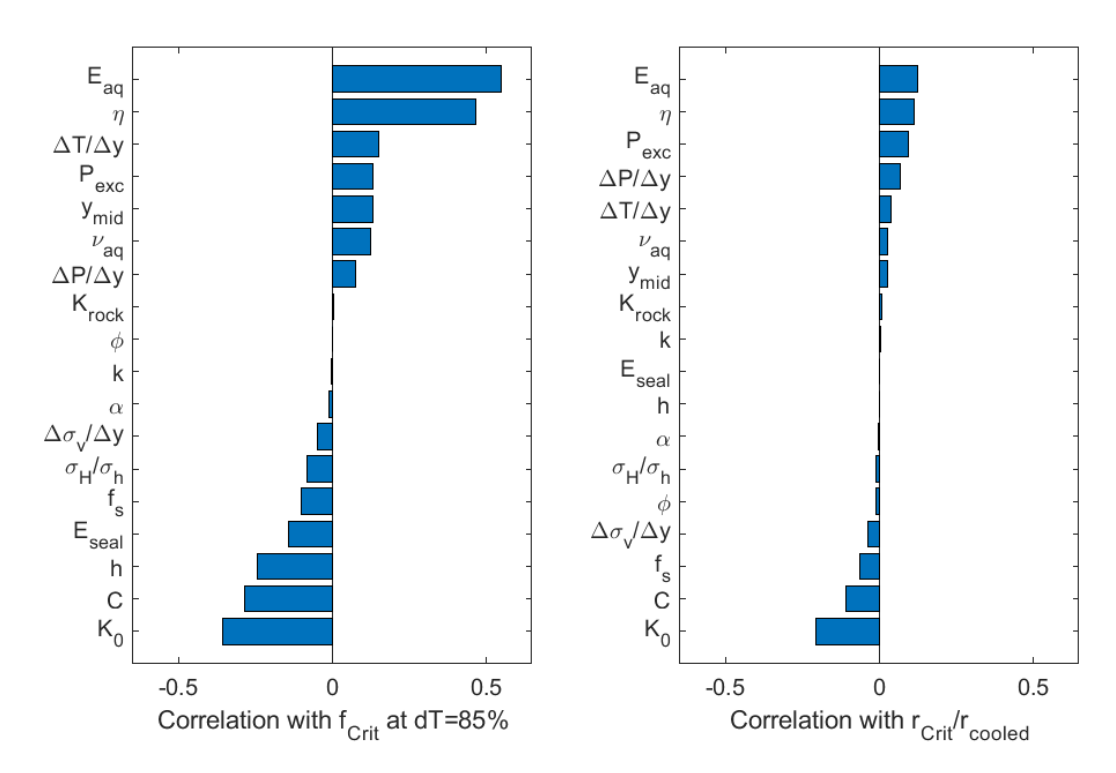


Figure 3-11 Correlation of activation risk measure at a line in the reservoir with the input parameters. For the meaning of the symbols see Table 3-1.

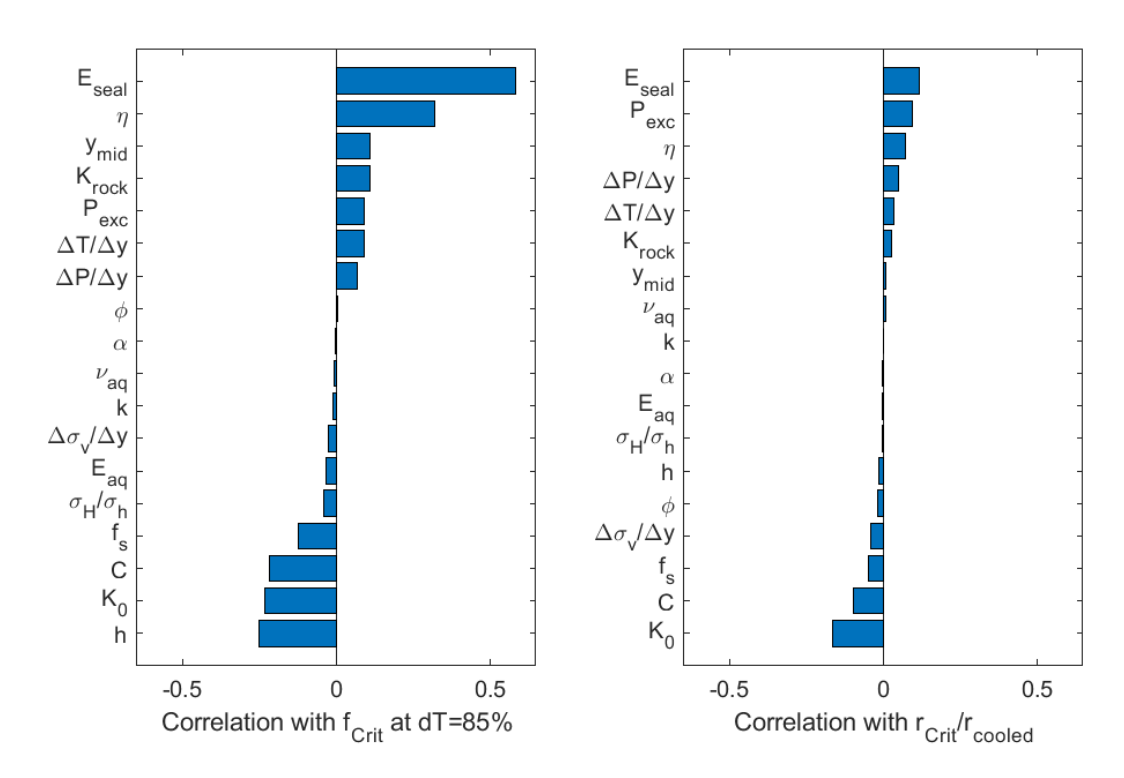


Figure 3-12 Correlation of activation risk measure at a line in the seal with the input parameters. The role of the seal elastic modulus is striking here. See Figure 3-11 for explanation of symbols.

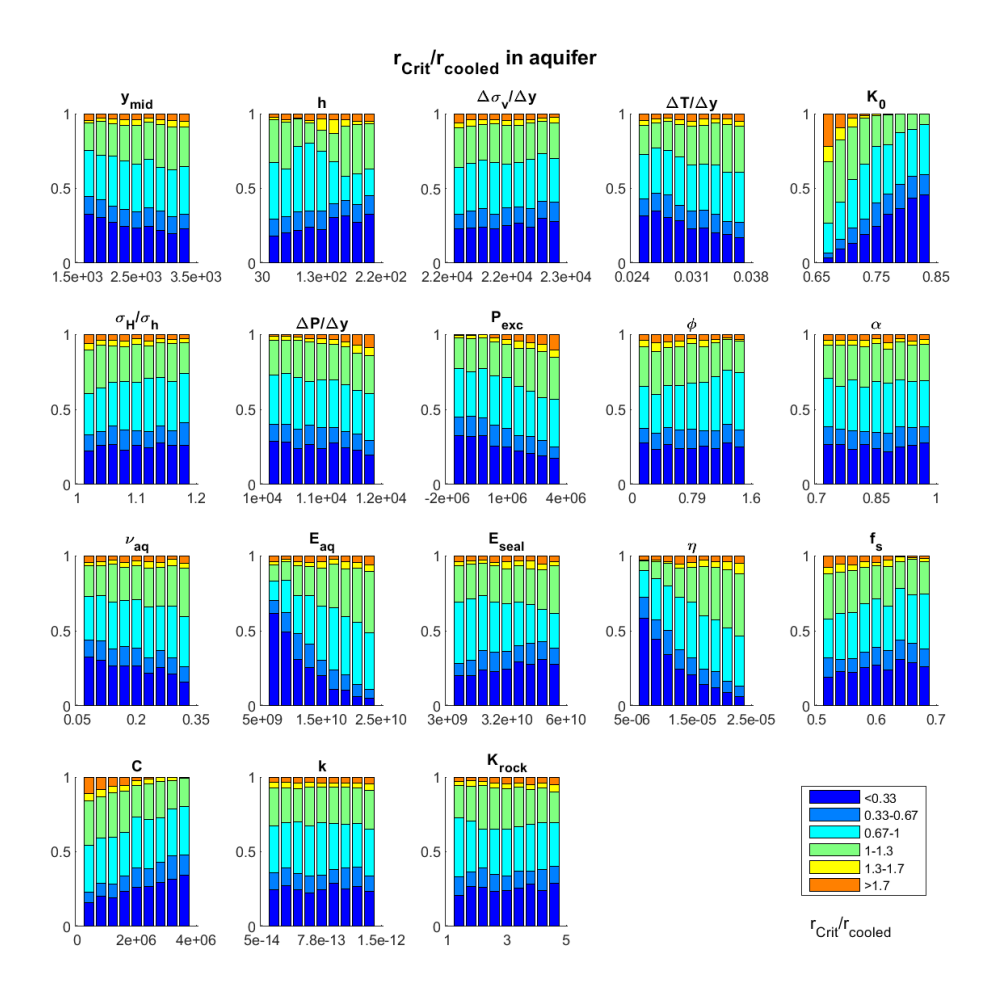


Figure 3-13 Distribution of the Radius of criticality with respect to the cooling radius in the reservoir. Symbols above the subplots refer to the uncertain parameters listed in Table 3-1. The effect of the different parameters is demonstrated by the variability of the distribution over the various bins. Large effects are associated with, e.g., the elastic modulus in the aquifer and the thermal expansion coefficient, the initial stress ratio, the reservoir overpressure and the cohesion. The elastic modulus in the seal hardly affects the critical behavior in the aquifer. Note that the simulations where $r_{crit}/r_{cooled} > 1.7$ reflect simulations that are already at failure at the start of operations.

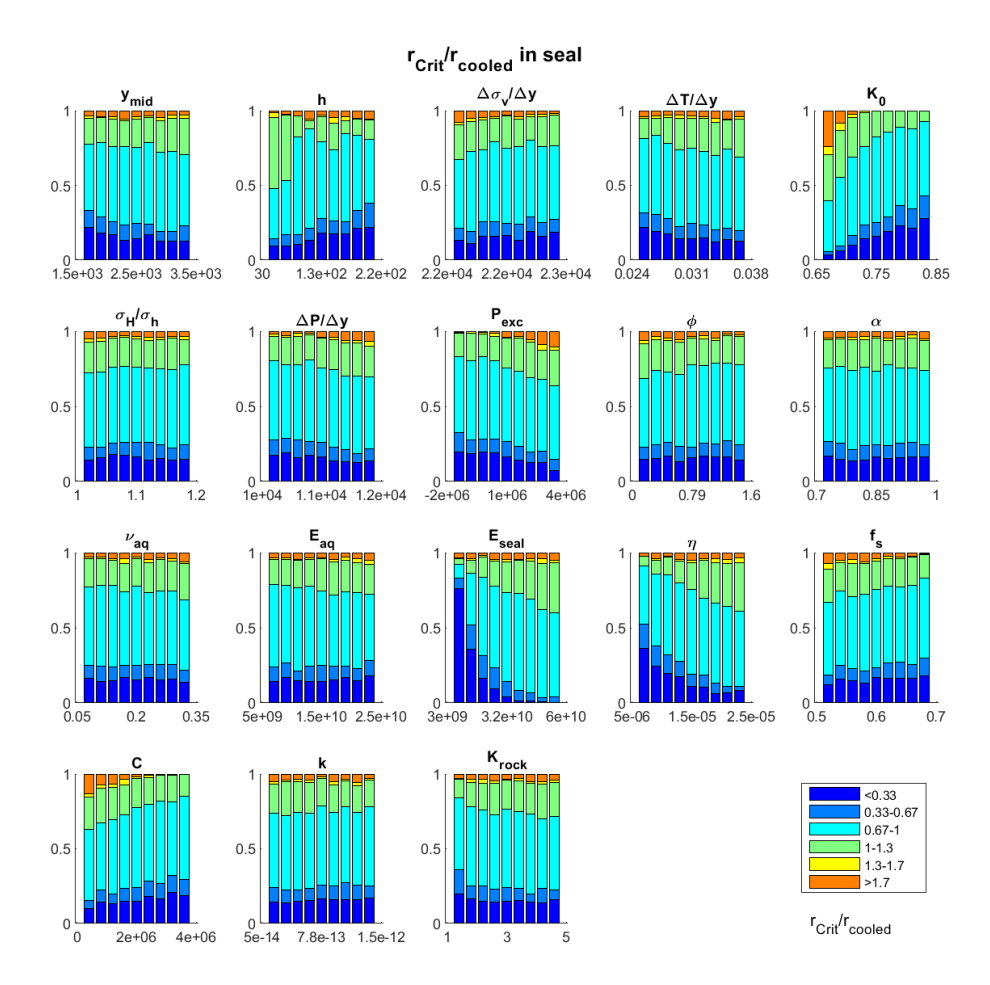


Figure 3-14 Distribution of the Radius of criticality in the seal, with respect to the cooling radius in the reservoir. In comparison with Figure 3-13, the sensitivity to the elastic modulus in the seal is striking. This is related to the stress concentration in seal and base at the interface, when larger elasticity contrasts are present. See Table 3-1 for explanation of symbols used. Note that the simulations where $r_{crit}/r_{cooled} > 1.7$ reflect simulations that are already at failure at the start of operations.

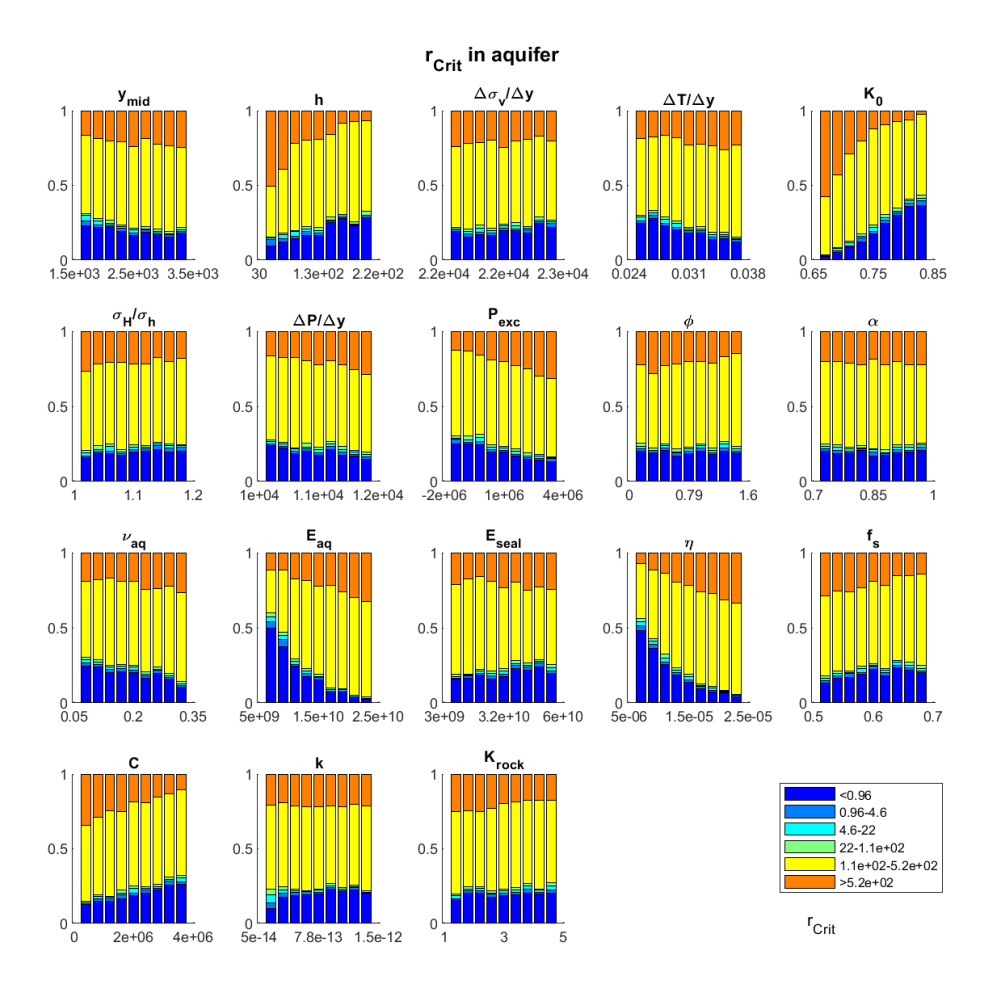


Figure 3-15 Distribution of the Radius of criticality in the aquifer. In comparison with Figure 3-13, the sensitivity to the reservoir thickness is striking. The scaling with the cooled radius in Figure 3-13 has removed most of the effect because the radius of criticality and the radius of cooling depend similarly on the reservoir thickness. See Table 3-1 for explanation of symbols used.

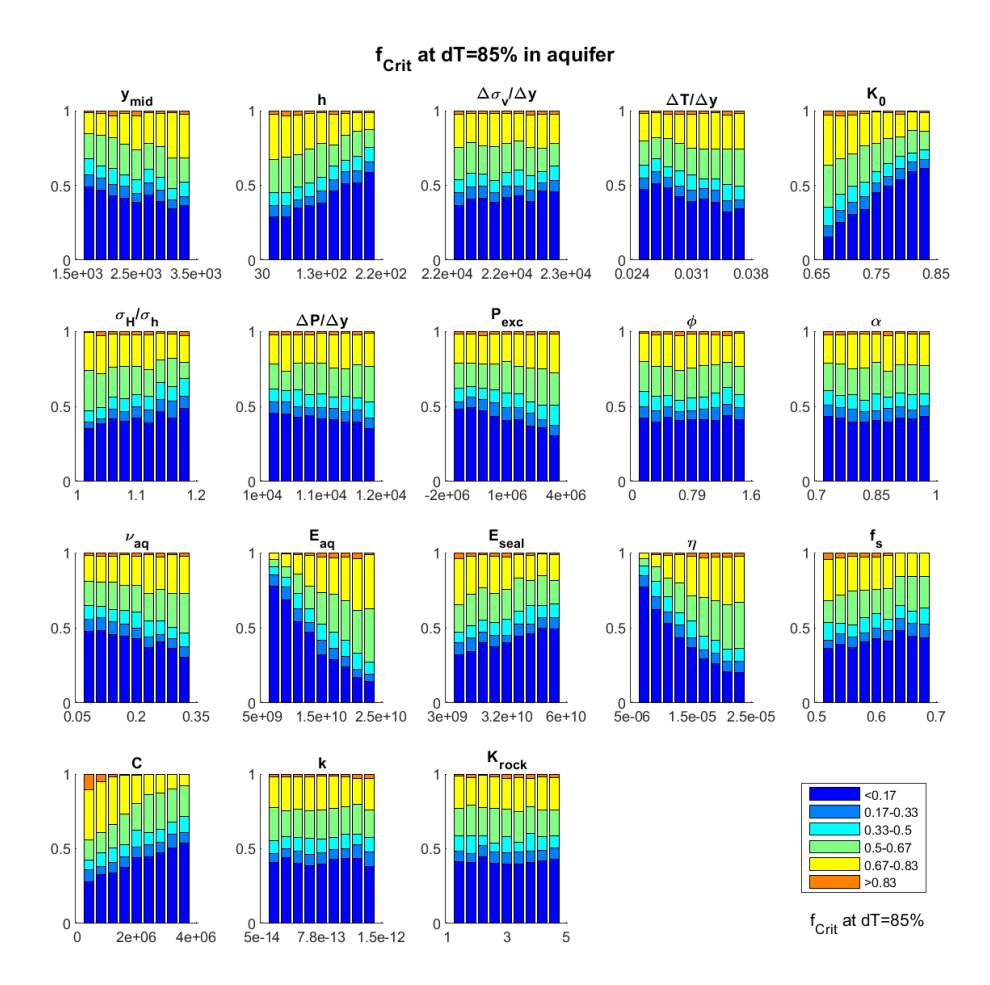


Figure 3-16 Distribution of the share of critically stressed fault orientations at the position where the reservoir has cooled to 85% of the temperature difference, in the reservoir. The distribution resembles Figure 3-13. See Table 3-1 for explanation of symbols used.

3.5 Discussion & Conclusion

We have demonstrated the potential of SRIMA for performing fast analyses, assessing sensitivities, and executing probability studies. The speed of calculation naturally implies some limitations. The first one is the assumption of radial symmetry of the pressure and temperature fields. This limits the application window to injection into a single vertical well in a reservoir with homogeneous flow and temperature properties. The single-vertical-well approximation is acceptable when one is interested in the response in the vicinity of the well and other wells are not very close, and when the well inclination is not severe. The effect of the well inclination can be assessed on the basis of the horizontal deviation in the reservoir with respect to the dimensions of the region where the effect of induced stresses are important. The homogeneity approximation may break down if, for instance, the reservoir exhibits high-permeability streaks or permeable fault systems. The radial-symmetry approximation further implies that the effect of fault offset cannot be investigated. This is an important limitation because such offsets can introduce stress concentrations that promote earlier activation, see also the following chapter.

The radial symmetry is imposed for the pressure and temperature solutions. As a consequence, the induced stresses are also radially symmetric. The original, virgin in-situ stresses, however, are not

bound to this constraint. Indeed, the induced contributions can be added to the non-symmetric virgin stresses; this can consequently lead to reactivation risks that are different for different positions at the same distance from the well. The effect of the original horizontal stress anisotropy propagates into an anisotropy of the risk measures.

A second limitation is that the tool, in the shape it has been presented here, can only handle a single injection rate. This is related to the method by which the heat and flow equations are solved. Solving for multiple injection rate steps is complicated due to the nature of the solution, which combines convection and conduction. The limitation can be alleviated, however, with the newest development that is currently being implemented: the use of pressure and temperature fields that are calculated externally. When such fields are properly digitized into a superposition of cylinders with constant pressure and temperatures, SRIMA can be used to evaluate the induced stresses.

The approximations introduced for calculating the effect of elastic contrasts have introduced inaccuracies; especially for cases with large elasticity contrasts the discrepancy may be considerable. In the Appendix we have shown that the approximations are usually conservative, apart from the reservoir locations just outside the cooled volume. Only for cases where the elastic modulus of the bounding layers is considerably smaller than the modulus of the injection layer the method is not conservative, and care must be taken while interpreting the results. For elastic contrasts up to a factor of 2, however, the differences remain acceptable. Consequently, we consider the tool appropriate for screening purposes as long as the ratio of elasticity between seal and aquifer is larger than a factor 0.5.

For the case that we evaluated in this report, the most critical input is related to the initial stress situation. If the stress is already critical or close to it, injection of cold water will quickly induce exceedance of the criticality measures in a large part of the reservoir. The initial criticality is determined by an interplay between the initial stresses, the overpressure of the reservoir, and the failure parameters.

When the initial criticality of the system is moderate or low, the expected radius of criticality mostly does not extend more than 30% beyond the thermal front.

The second largest effect is related to the magnitude of the thermoelastic stress perturbations. These are mainly related to the temperature difference between injected fluid and the virgin reservoir, the thermal expansion coefficient, and the elastic modulus. Additionally, the modulus contrast between seal and aquifer is important, in particular in the case of a stronger seal. In that case, stress concentration develop in the bounding layers due to their larger resistance against thermo-elastic deformation. Even tensile stresses may develop, with the risk of inducing hydraulic fractures in the seal.

In summary, we consider SRIMA a valuable tool for the evaluation of induced stresses and associated fault reactivation risk measures. Sensitivities can be identified quickly and the key parameters determined. Clearly, to narrow the uncertainties present in current applications, better knowledge of subsurface data is required. In addition, it is crucial models are validated against field data and monitoring data. Does the evolution of the cooling front roughly follows what is predicted by SRIMA? Do we see signs of fault reactivation (seismic events) at locations where we know the cooling front has reached a known fault? Without this step, the predictive power of the models are limited. We recommend this validation step in future site-specific studies, and evaluation of the model performance for an actual case study.

4 Cooling- and depletion-induced rupture in a faulted reservoir

4.1 Abstract

As the number of geothermal doublets in the Netherlands increases, it is important to mitigate felt induced seismic events. To do so it is crucial to understand the mechanics of fault reactivation and key parameters controlling induced events magnitude. Geomechanical modeling can be used to gain a first-order understanding of induced stress changes due to doublet operations, assuming the dominant processes and mechanisms are captured. However, such models should be able to address the substantial uncertainties in subsurface input parameters, and they should be validated to monitoring data. In addition, to model event magnitudes it is essential to incorporate fault weakening behavior which is a fundamental aspect of seismic instability on faults. Here we present a fast, semi-analytical 2D model approach PANTHER2D (Physics-based semi-Analytical Tool for Human-induced Earthquake Rupture). This approach allows for rapid stochastic investigation of fault reactivation and rupture length (i.e. the along-dip fault section that slipped during the seismic event), taking into account reservoir offset and rupture dynamics. We compared reactivation and rupture characteristics for both a depleting and for a cooling reservoir (uniform pressure or temperature change in the reservoir + diffusion to the seal and base). Note that we assume the fault is not sealing, and lies within the depleted or cooled volume, which is a conservative assumption for cooling (e.g. an undetected fault near the injection well). The main results are summarized here, for steeply dipping normal faults:

- The stress path was more destabilizing for cooling than for depletion. This was because the effective normal stress decreases during cooling but increases during depletion.
- Fault reactivation for depleting reservoirs was strongly controlled by fault throw, the poroelastic rock parameters, and the initial tectonic stress state.
- Fault reactivation for cooling reservoirs was mostly influenced by the thermo-elastic rock parameters as well as fault throw and the initial tectonic stress state.
- For both depletion and cooling, reverse faults were less likely to be reactivated than normal faults.
- The finite width of the cooled volume reduced the stress changes and the potential for fault reactivation, but mostly so when the width is small compared to the reservoir height e.g. during initial stages of injection, or for very thick reservoirs.
- Along-dip seismic rupture length was mostly controlled by the initial tectonic stress, fault
 dip and the frictional weakening parameters, as well as reservoir thickness and fault throw.
 The latter two influence the fault length over which stress changes occur, with thicker
 reservoirs causing a larger perturbed fault length and hence larger rupture lengths.
- Along-dip rupture lengths were larger for cooling but the stress drop was smaller, as the
 effective normal stress decreases during cooling but increases during depletion.

4.2 Introduction

The number of geothermal doublets in the Netherlands is expected to increase significantly over the coming decades, as the geothermal energy production will contribute increasingly to the national heat supply (Stichting Platform Geothermie et al., 2018, PBL, et al., 2020). To facilitate the growth of geothermal energy it is important to mitigate undesirable side-effects, one of which is the potential

occurrence of induced seismicity resulting from geothermal operations in the subsurface. Understanding the mechanics of these events and the conditions under which such events can occur is crucial for site-specific hazard assessment and the development of mitigation measures.

Induced seismicity is not a new phenomenon in the Netherlands. Over the past decades more than 1,000 induced events with magnitudes up the M 3.6 were linked to gas production. The majority of events were observed in the Groningen gas field, the largest gas field in the Netherlands, but over 20 smaller gas fields have also been associated with induced seismicity. Most gas reservoirs are composed of porous sandstone formations located at 2 – 3 kilometer depth. Similar shallow sandstone formations are also targeted by the majority of geothermal projects (Buijze et al., 2019a; Willems, 2017; Mijnlieff, 2020, TNO-AGE, 2020). However, even though the lithology is the same, the mechanisms leading to stress changes in the subsurface are very different. Whereas stress changes during gas production are the result of a pore pressure decrease and poro-elastic stress changes causing a reduction in total horizontal stress, stress changes in a geothermal doublet are dominated by cooling of the formation around and away from the injection well and, to a smaller extent, by pressure increases near the injection well. The conditions under which faults can be reactivated will be affected by this difference in stressing mechanism.

Here, we evaluate the effect of the stressing mechanism – i.e. pressure decrease vs. cooling - on fault reactivation and subsequent fault rupture, using a semi-analytical 2D model of a faulted reservoir formation experiencing depletion or cooling. Previous studies on production-induced seismicity have shown the importance of the reservoir offset on stress changes (Buijze, van den Bogert et al., 2019; Mulders, 2003; Orlic & Wassing, 2013; Roest & Kuilman, 1994); hence fault offset is taken into account in the current model. Also, the effect of frictional weakening, a fundamental requirement for seismic instability and earthquake rupture, is incorporated and the length of the fault that slipped during the induced seismic event is computed. The simplified model setup allows for fast calculation of stress changes, reactivation and fault rupture, allowing for stochastic analysis to address the substantial uncertainty in input parameters and a comparison between depletion- and cooling-induced seismicity.

4.3 Methods

4.3.1 Model setup

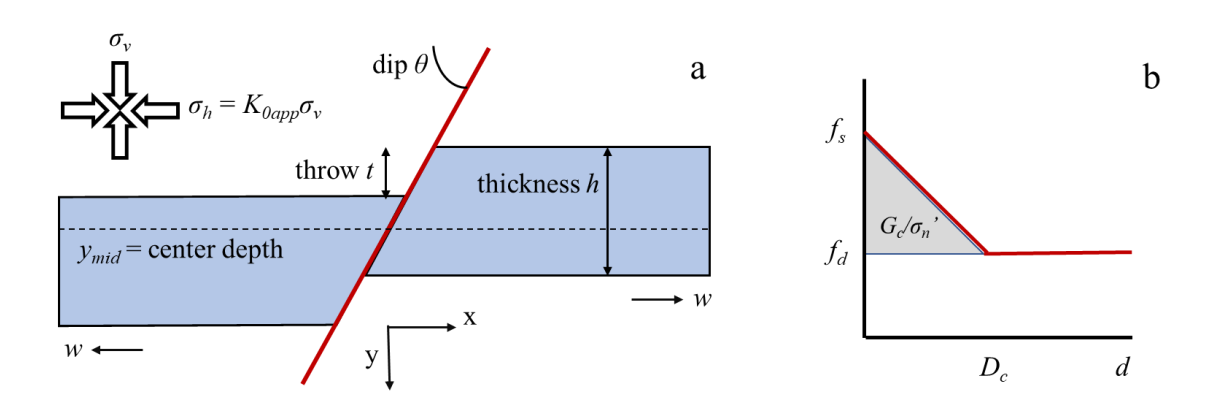


Figure 4-1 Model setup and fault friction model. a) Model setup. Reservoir with width w and thickness h, with the center located at a depth of y_{mid} . The reservoir is offset by a fault with dip ϑ and throw (vertical offset) t. σ_v : vertical stress, σ_h : horizontal stress, compressive stresses are positive. b) Linear slip-weakening friction governing fault behavior, with f_s : static friction, f_d : dynamic friction, D_c critical slip distance, and G_c : fracture energy.

We use a generic plane-strain 2D model geometry based on that of faulted porous sandstone reservoirs in a normal faulting environment, which is considered representative for most of the Netherlands. The model geometry consists of two reservoir compartments with a finite width w, and with vertical thickness h. The compartments are offset by a fault with a vertical offset or throw t and

a fault dip angle ϑ (Figure 4-1a). Depth is taken positive, and the depth of the reservoir is defined by the center depth of the reservoir interval y_{mid} at -0.5(h + t) from the top of the footwall.

The total initial (tectonic) maximum and minimum stress are oriented vertically (σ_v) and horizontally (σ_h) , with $\sigma_v > \sigma_h$ (normal faulting environment) and compressive stresses taken positive. The total vertical stress σ_v is prescribed via a vertical stress gradient $\Delta \sigma_v / dy$, and the total minimum horizontal stress is prescribed through the stress ratio K_0 as $\sigma_h = K_0 \sigma_v$. A difference between the strike of the fault and the direction of the maximum total horizontal stress σ_h is also considered, and is defined by strike deviation angle φ . For $\varphi \neq 0$, the total horizontal stress is recomputed to the apparent minimum horizontal stress σ_{ha} in the model plane from φ and the horizontal stress ratio σ_H / σ_h . Similar to the vertical stress gradient a pore pressure gradient $\Delta P / dy$ is set to describe the initial pressure distribution. Additionally, an initial under- or overpressure P_{exc} can be specified in the reservoir formation, which is defined with respect to the pressure computed at the base of the footwall using the pressure gradient. Initial reservoir pressure P_0 is defined as the total pressure at the base of the footwall – i.e. the sum of the pressure resulting from the pressure gradient and the under- or overpressure P_{exc} . The principal stresses are converted to initial shear stress τ_0 and effective normal stress σ_{n0} on the fault.

Linear elasticity is assumed for the formations, with uniform elastic properties (Young's modulus, Poisson's ratio, and Biot coefficient) throughout the model space. Fault strength τ_s is governed by the Mohr Coulomb failure criterion

$$\tau_S = C + f_S \sigma_n' \tag{4-1}$$

with static friction coefficient f_s , cohesion C, and effective normal stress σ_n . During the depletion or cooling phase no frictional weakening is assumed, but for the rupture phase linear slip-weakening is assumed on the fault, where friction decays linearly from f_s to dynamic friction coefficient f_d over the critical slip distance D_c (Figure 4-1b). The dynamic shear strength τ_d is defined similar to the failure strength as $C + f_d \sigma_n$, here assuming cohesion does not change during rupture.

4.3.2 Pressure and temperature changes

Depletion is modeled in a simplified manner through prescribing a uniform ΔP throughout the reservoir compartments. Equation 8-5 is used to model pressure diffusion to the seal and base. The fault segments flanking one or both of the reservoir compartments are assigned the same ΔP as the reservoir formations. A finite width w is prescribed for the depleting compartments.

For the cooling scenario it is assumed the fault lies close to the well at x=0 (i.e. representative of an undetected fault, and cooling occurs on both sides of the fault. A uniform temperature change ΔT is prescribed in the reservoir compartments flanking the fault, over a width w that is based on the radius of the cooled volume that can be calculated using the convective heat balance equation. This equation assumes lateral convective flow (as in SRIMA, section A.3) and a uniform temperature distribution within the cooled volume, and no conduction to the seal and base. The radius of the cooled volume r_c is given by (e.g. Koning & Niko, 1985, Koning, 1988)

$$r_{cooled} = \left(\frac{c_{fluid}\rho_{fluid} \ qt_{inj}}{c_{rock}\rho_{rock}h\pi}\right)^{0.5}$$
4-2

Where c_{fluid} and ρ_{fluid} are the specific heat capacity (Jkg⁻¹K⁻¹) and density (kgm⁻³) of the injection water, c_{rock} and ρ_{rock} the specific heat capacity and density of the rock formation, q the flow rate (m³s⁻¹), t_{inj} the injection time (s), and h the reservoir height. Whereas pressure changes due to gas production are mostly limited to the reservoir formation, for geothermal doublets cooling propagates into the seal and base formations through conduction (e.g. Saeid & Barends, 2009, Candela et al., 2018). The calculations in SRIMA show that in fact a substantial part of the seal and base can experience cooling (e.g. Figure 3-2, Figure A-3), which in turn causes substantial thermo-elastic stress changes above and below the reservoir (Figure 3-3). Here the same equations for vertical conduction (see section A.1) are used to compute the temperature distribution above and below the reservoir, assuming an injection time of 30 years (see Figure 4-2a and b for example of the temperature field).

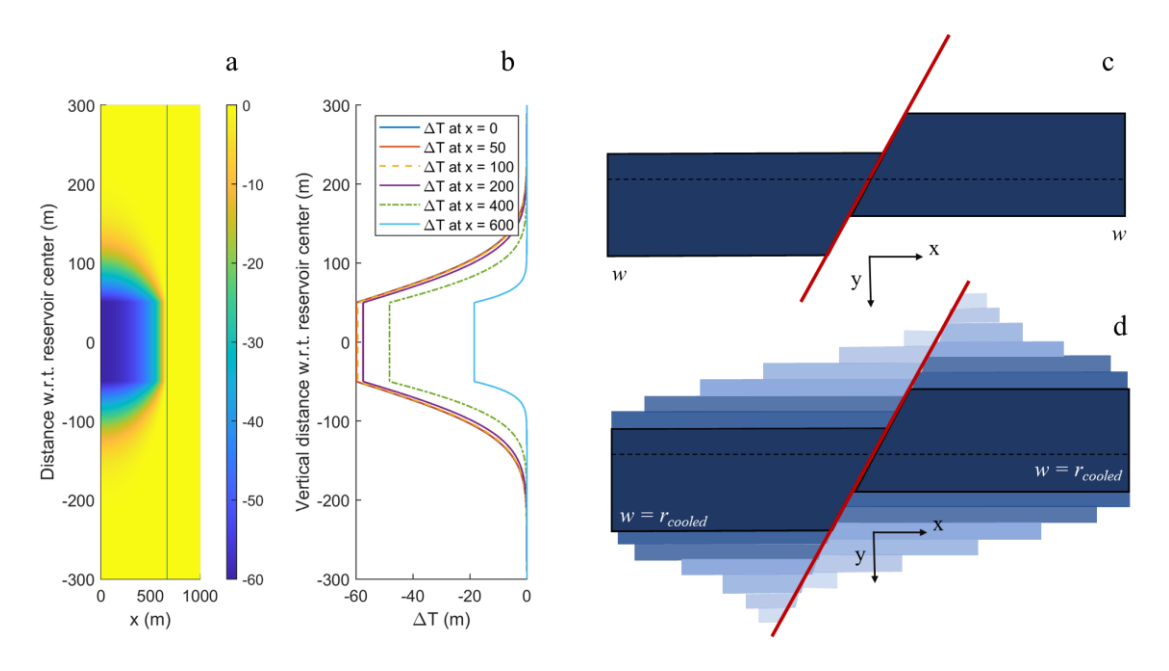


Figure 4-2 Illustration of pressure and temperature functions used in the model. A) temperature field around a well at x - 0 computed assuming axisymmetry and lateral convective flow and vertical conduction as in SRIMA, section A.3, for the default input parameters (Table 3-1), b) temperature distributions at various distances from the well. C and d show the implementation of pressure (c) and temperature fields (d) in PANTHER2D.

4.3.3 Pressure- or temperature-induced stress changes

To compute the stress changes resulting from pressure and temperature changes in the reservoir compartments in 2D the closed-form solutions published by Jansen et al. (2019) are used. These solutions are based on inclusion theory (Eshelby, 1957) where the reservoir compartments are treated as inclusions in an infinite medium. These inclusions undergo a certain pressure- or temperature- induced strain, which is resisted by the presence of the medium around the inclusion. This causes stress changes within and outside of the inclusion. Closed-form solutions of the stress changes can be obtained for certain geometries, such as ellipsoidal and rectangular inclusions (e.g. Eshelby, 1957; Soltanzadeh & Hawkes, 2008), or square and triangular inclusions as used to represent the reservoir compartments in the model of Jansen et al. (2019) and the model geometry used here. The equations in Jansen et al. (2019) were derived for pressure changes; to model uniform cooling of the reservoir formations the poro-elastic stress path parameter s changed from

$$\frac{(1-2\nu)\alpha\Delta P}{(1-\nu)}$$
4-3

for pressure changes ΔP (depletion negative), to the thermo-elastic stress path parameter

$$\frac{E\eta\Delta\mathrm{T}}{(1-\nu)}$$
4-4

for temperature ΔT (cooling negative), where ν is Poisson's ratio, α is Biot's coefficient, E is Young's modulus, and μ is the shear modulus.

To compute the stress changes resulting from depletion or cooling of the seal and base formations the temperature field in those formations is discretized into depth slices of 4 m in height, and a uniform temperature change equal to the maximum temperature change in that depth slice (see schematic example in Figure 4-2d). The width of each depth slice is equal to the reservoir width (for depletion) or, for cooling, equal to the values of x where the temperature change is > 2% of that of the reservoir For each of the depth slices stress changes are computed, which are then summed for all slices and superimposed on the stress changes computed for the reservoir compartments. Note that near the fault the assumption of vertical conduction may not be correct, as here lateral

conduction may also occur along the seal-reservoir and base-reservoir juxtapositions. However, results are in agreement with 2D Finite Element simulations assuming a similar pressure or temperature profile. Also note that the model assumes plane-strain conditions, whereas the temperature field is axisymmetric; this assumption will be addressed in the discussion. Note also that the total amount of cooling is overestimated in this approach, as towards the radius of the cooled front the temperature change will decrease gradually instead of remain uniform (see e.g. Figure 6-2). In future studies a discretization of the temperature front in the reservoir could be implemented such as is done for SRIMA (section A.3) to better model the temperature change in the reservoir.

4.3.4 Modeling of fault reactivation and onset of seismic fault slip

The net effect of the computed shear and effective normal stress changes on the fault can be expressed using the Coulomb Failure Stress changes (Δ CFF)

$$\Delta CFF = \Delta \tau - (C + f_s \Delta \sigma'_n)$$
 4-5

where positive values indicating fault stresses are closer to failure and negative values indicating fault stresses become more stable. Similarly the total Coulomb Failure stress on the fault (i.e. the sum of the initial shear and normal stress and the stress changes) indicates the proximity to failure on the fault

$$CFF = \tau - (C + f_s \sigma'_n)$$
 4-6

with reactivation occurring for CFF = 0. For fault reactivation assessment and seismic hazard studies it is of interest to model the amount of ΔP or ΔT that is required to bring a fault to failure (CFF \geq 0). However, the uniform depletion of a square- or triangular-shaped reservoir formation leads to shear stress singularities developing at the reservoir corners; this is inherent to the closed-form solution for rectangular inclusions (Jansen et al., 2019). The presence of the singularities implies that only an infinitesimal amount of ΔP is required for the fault to be reactivated – i.e. for the first location on the fault to attain its failure strength τ_s (e.g. Jansen et al., 2019). The singularity is artificial and expected to be flattened by e.g. fault slip or plastic deformation. Taking the reactivation pressure to be equal to the pressure or temperature change required for τ to exceed τ_s at any location along the fault would thus be erroneous. In addition, frictional weakening requires a finite fault length to be sliding (i.e. to be reactivated) in order for seismic instability to develop and for rupture to self-propagate along the fault without any further induced stress changes. This critical nucleation length depends on the elastic properties of the medium around the fault and the amount of frictional weakening; for the linear slip-weakening friction used here (Figure 4-1b) the nucleation length is defined as (Uenishi & Rice, 2003)

$$L_c = 1.158 \frac{\mu^* D_c}{(f_s - f_d)\sigma_n'}$$
 4-7

where μ^* is the mode II shear modulus $\mu/(1-\nu)$. Previous numerical studies showed that this theoretical nucleation length matched well with the observed slipping fault length at the numerically determined onset of seismic instability (Buijze et al., 2019b; Buijze, 2020; Buijze et al., 2017). Here we define the onset of fault reactivation as the ΔP or ΔT that is required to raise the stress to $\tau >= \tau_s$ over a fault length L_c . The pressure or temperature change at which this occurs is indicated as ΔP_c or ΔT_c , and similarly the fault stresses at the onset of reactivation are termed τ_c and σ_{nc}

Note that critical length-scales for reactivation are often present explicitly or implicitly in other numerical modeling approaches for induced fault reactivation. In numerical modeling studies, the magnitude of the stress concentration depends on the cell size used in the numerical model; the smaller the element size the more resolved the stress singularity. In Vöros and Baisch (2018) the stress distribution along the fault is actually smoothed with a minimum lengthscale of 10 m. The L_c in our simulations, using the input parameters in Table 4, covers a similar range, from ~1 – 10s of meters. The stress concentrations could also be smoothed by allowing aseismic slip on the fault (e.g. Buijze, 2020, van Wees, 2018). This is possible in PANTHER2D but has not been included in the

current work for the sake of computation speed. Uncertainties in the nucleation process are substantial and multiple approaches may be reasonable, as long as clearly stated what is the reactivation criterion, in terms of the assumed critical length scale, element size, smoothing length-scale and/or aseismic slip.

4.3.5 Rupture length

Once the nucleation criterion is reached, no further pressure and temperature changes are modelled and fault slip will self-propagate beyond the reactivated fault length L_1 . It is interesting to compute the final rupture length (i.e. the fault length that will have slipped during the seismic rupture, L_2) as this length is directly related to the event magnitude. The along-dip rupture length L_2 is approximated using linear elastic fracture mechanics (LEFM), rather than using computer-intensive dynamic simulations. Previous modeling studies showed that fracture mechanics theory for crack growth works well to approximate the arrest of rupture on a slip-weakening fault (Ampuero & Ben-Zion, 2008; Galis et al., 2015; Ripperger et al., 2007), and fracture mechanics has also been shown to quantitatively describe rupture arrest in experiments (Bayart et al., 2016; Kammer et al., 2015; Kammer & McLaskey, 2019; Svetlizky & Fineberg, 2014). LEFM has been applied to compute induced rupture lengths in a 2D Finite Element model of a depleting faulted reservoir (Buijze, 2020). Following the same methodology, we compute the along-dip rupture length for the current 2D model.

4.3.6 Input parameters and stochastic analysis

There are a substantial number of input parameters in the model which often have a large uncertainty, for example the initial stress ratio which is poorly known. Therefore, stochastic analysis was performed to investigate the impact of various geometrical, elastic, and frictional parameters and their uncertainties on reactivation (ΔP_c and ΔT_c) and rupture length (L_s). For each input parameter a range was defined, and for each model realization the input parameters are sampled randomly from these given ranges, yielding a ΔP_c and ΔT_c and rupture length for each realization. Input parameter ranges were based on those for geothermal plays in porous sandstone formations in the Netherlands. For the current analyses we have used uniform distributions specified by an lower and upper bound, listed in Table 4-1.

Table 4-1 Overview of default input parameters and ranges of the uniform distributions used for the stochastic analysis.

Parameter	Symbol	Unit	Range (default)
Mid depth	Ymid	m	1500 – 3500 (2300)
Reservoir thickness	h	m	30 – 220 (100)
Throw	t	m	-0.5 h – 1.5h (0.5h)
Dip	θ	0	50 – 90 (70)
Vertical stress gradient	$\Delta\sigma_{v}/\Delta y$	Mpa/km	21 – 23 (22)
Stress ratio σ_h / σ_v	K_0	-	0.65 - 0.85 (0.75)
Horizontal stress ratio σ_H / σ_h	σ_H/σ_h	-	1.0 -1.2 (1.1)
Pressure gradient	$\Delta\sigma_v/\Delta y$	Mpa/km	10 – 11.5 (10.7)
Strike with respect to σ_H	φ	deg	0 – 90 (0)
Overpressure in the reservoir	P_{exc}	Mpa	-2 - +4 (0)
Biot coefficient	α	-	0.7 - 1 (1)
Poisson's ratio	ν	-	0.05 - 0.35 (0.2)
Young's modulus	E	Gpa	5 – 25 (15)
Linear thermal expansion coefficient	η	°C -1	$0.5 \cdot 10^{-5} - 2.5 \cdot 10^{-5} (1 \cdot 10^{-5})$
Static friction	f_s	-	0.5 - 0.7 (0.6)
Dynamic friction	f_d	-	0.15 - 0.45
Critical slip-weakening distance	D_c	mm	0.6 - 100
Cohesion	C	Mpa	0 - 4
Width (gas fields)	w	m	1000 - 7000
Width (geothermal = r_{cooled})			Follows from Eq. 4-2

Most geothermal target formations in the Netherlands are situated at depths between 1500 and 3000 m and have a thickness h between 50 and 220 m (Figure 2-2). These ranges are similar for hydrocarbon fields, although they are thinner and some of these fields can be deeper. The total width of most hydrocarbon fields is in the order of 1000 – 7000 m (www.nlog.nl). Note that in the current model the formations on either side of the fault have the same width, so that w for hydrocarbon fields is 500 - 3500 m. The width of the reservoir compartments for the cooling scenario is based on the cooled radius computed using the heat balance equation (Equation 4-2). Assuming a salinity of 10% the specific heat capacity of the injected water is $c_{fluid} = 3771 \text{ Jkg}^{-1}\text{K}^{-1}$ (ref, e.g. Sun et al., 2008) and a density is 1052 kgm⁻³ (Batzle & Wang, 1992), and the specific heat capacity of the reservoir formation is taken as c_{rock} = 850 Jkg⁻¹K⁻¹ with a rock density of 2200 kgm⁻³ (see also Table 3-1 and Table 5-1). The injection time is set at 30 years, the typical lifetime for which geothermal doublets are developed. Lower and upper bounds of r_{cooled} computed from the given range of reservoir thicknesses h(30 - 300 m), the range of flow rates $(0.02 - 0.125 \text{ m}^3\text{s}^{-1})$ are 190 m and 1290 m, with the largest r_{cooled} for thin reservoirs with high flowrates (Figure 4-3). For each simulation a value is sampled for the reservoir thickness and the width w of the modeled reservoir is set equal to this radius r_c. To compute the vertical heat or pressure diffusion the same parameters are used for the seal and base as in Chapter 3 and Chapter 5, e.g. Table 3-1.

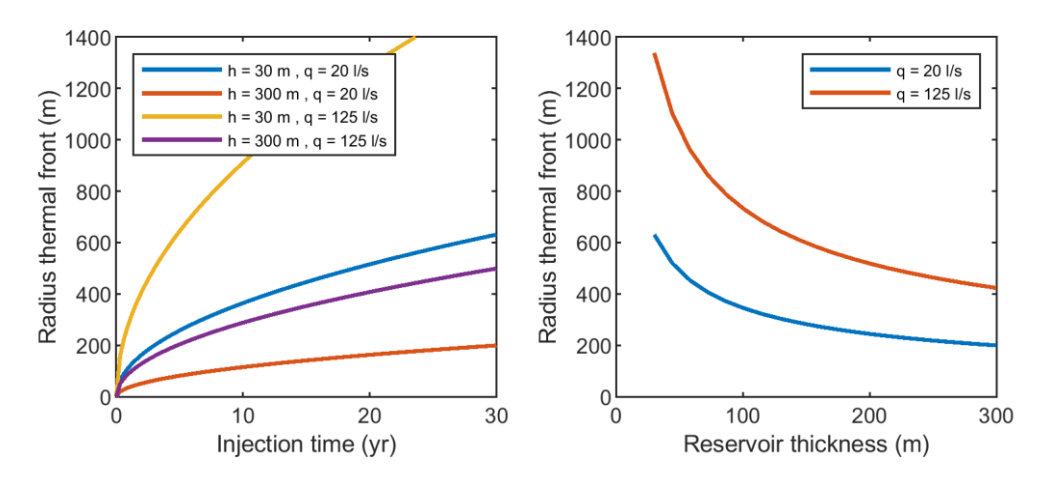


Figure 4-3 Radius of the thermal front computed based on heat balance (Equation 4-2). This radius is used to set model width w for cooling reservoir formations.

The maximum pressure decrease in a hydrocarbon field is taken as 95% of the initial reservoir pressure (and will thus be dependent on depth). Similarly, the maximum amount of cooling depends on the initial temperature in the reservoir, which is also a function of depth. An injection temperature of 20°C is assumed, which gives a minimum ΔT of -30°C and a maximum ΔT of -110°C, for the range of $\Delta T/\Delta y$ and depths evaluated.

4.4 Results

4.4.1 A different stress path for depletion and cooling

Depletion and cooling lead to a different stress response on the fault. A first order comparison of the stress paths can be made assuming uniaxial strain conditions (representative for a laterally extensive reservoir without offsets or other geometric complexities). For a give pressure and temperature change, uniaxial strain conditions the total vertical stress change is zero, and the total horizontal stress change due a pressure change is given by (e.g. Soltanzadeh & Hawkes, 2009)

$$\Delta\sigma_h = \frac{\alpha\Delta P(1-2\nu)}{(1-\nu)}$$
 4-8

and for a temperature change is given by

$$\Delta \sigma_h = \frac{E \eta \Delta T}{(1 - \nu)} \tag{4-9}$$

where E is Young's modulus, η is the linear thermal expansion coefficient, and v is Poisson's ratio. The corresponding stress paths for depletion and cooling are shown in Figure 4-4. Several differences are apparent. First of all, the slope and direction of the stress path $(\Delta \tau / \Delta \sigma_n')$ is different; for depletion an increase in both shear and effective normal stress is observed, whereas for cooling the shear stress increases but the effective normal stress decreases. This difference is related to the pressure changes in the fault during depletion. For both depletion and cooling a volumetric strain of the reservoir occurs – the reservoir shrinks. For laterally extensive reservoirs as used for the example in Figure 4-4, this volumetric reduction can be accommodated vertically in the form of reservoir compaction and subsidence of the overburden, and the total vertical stress change is thus zero. Strain in the horizontal direction is prevented as the reservoir is elastically coupled to formations to the side, which leads to reduction of total horizontal stress σ_h . Since the total vertical stress remains constant, a decrease in total horizontal stress causes an increase in differential stress, $\sigma_v - \sigma_h$ for a normal faulting regime, and a stress path where $\Delta \tau$ is positive and $\Delta \sigma_n'$ is negative, as seen for cooling. For depletion however, the effective normal stress is also affected by the reduction of pore pressure in the fault. The net result of the reduction in total horizontal stress and the pressure change in the fault is an increase in effective normal stress for depletion. If we were to assume that the fault

pressure does not change during depletion the effective normal stress would decrease with depletion and the slope of the stress path would have a similar direction as for cooling.

A second difference is that the slope of the stress path $(\Delta\tau/\Delta\sigma_n')$ for depletion under uniaxial conditions (laterally extensive reservoir) depends on the elastic parameters, whereas for cooling the slope does not change, only the magnitude of the stress changes. This is again due to the combined effect of the total horizontal stress decrease and the fault pressure change on the effective normal stress change for the depletion scenario. If no pressure change would be assumed in the fault the slope of the stress path would solely be a function of fault dip, for laterally extensive reservoirs. Note that for other geometries and aspect ratios the slope of the stress path will depend on the elastic parameters both for cooling and for depletion.

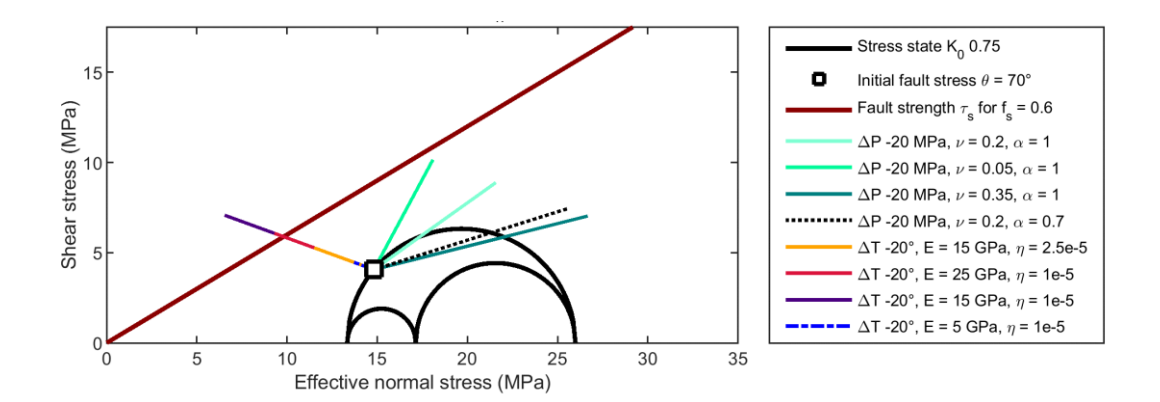


Figure 4-4 Examples of stress paths for depletion and cooling, for a normal fault with a dip of 70 degrees without offset. The stress paths were computed using the default parameters shown in Table 4-1, for default and upper and lower values of Poisson's ratio and Biot coefficient or Young's modulus and linear expansion coefficient.

4.4.2 Fault offset locally concentrates fault shear stress

The stress changes above were calculated for a laterally extensive reservoir. However, reservoirs are often intersected by faults that offset the reservoir formation. A number of previous studies have shown that depletion of offset reservoir formations causes the fault stresses to concentrate in the reservoir and in particular near the top and bottom of the reservoir interval, promoting fault reactivation with respect to a reservoir formation that is not offset (Buijze et al., 2019b; Mulders, 2003; Orlic & Wassing, 2013; Roest & Kuilman, 1994). This is inherent to the discontinuity in the assumed pressure change at the reservoir's top and bottom, in combination with the angular shape of the reservoir; in the equations derived by Jansen et al. (2019) it can be seen that shear stress concentrations (singularities in fact) develop at the corners of angular inclusions. Here pressure or temperature diffusion to the seal and base are accounted for. This more gradual P or T profile strongly reduces these stress concentrations, and a smoother stress profile is observed along the fault (Figure 4-5a-d)). Also, the sharp normal and shear stress decreases above and below the reservoir that are typically present for uniform depletion of the reservoir only (e.g. Mulders et al., 2003, Buijze et al., 2019) have largely disappeared due to pressure diffusion. However, a CFF decrease is observed for several 100 m from the reservoir (Figure 4-5c)

With respect to the stress change computed for a fault without offset in a laterally extensive reservoir (i.e. uniaxial conditions, as used for the stress paths in Figure 4-4 and indicated with the black markers in Figure 4-5), the shear stress change for the offset reservoir is significantly enhanced along the entire reservoir-reservoir interval. The effective normal stress change in the reservoir similar to the uniaxial strain conditions, but the net effect is an enhancement of the Coulomb Failure stress change with respect to uniaxial conditions (Figure 4-5c). Hence, for the depletion scenario reservoir offset concentrates the fault failure stresses along the reservoir interval and promotes fault reactivation along this interval.

This is reflected in the available stress drop at the onset of fault reactivation (Figure 4-5d), which is the difference between the shear stress at the onset of reactivation τ_c and the dynamic stress strength τ_d . A positive stress drop allows for fault slip and rupture to occur, but a negative stress drop will arrest a propagating rupture. Whereas the conditions in the reservoir area favorable for the propagation of rupture, those further away from the reservoir are less favorable.

The fault stress changes for cooling shows some differences compared to those for depletion. Firstly, it can be observed how the effective normal stress for cooling decreases instead of increases (see also 4.4.1). Secondly, the stress perturbation extends further into the seal and base. This is due to the different length scale of pressure diffusion versus temperature diffusion. Whereas for depletion the shear stress and Coulomb failure stress were significantly enhanced with respect to those for uniaxial conditions, for cooling the stress changes in the reservoir-reservoir interval are only slightly larger than for uniaxial conditions; the role of reservoir offset appears less than for depletion, likely due to the smoother temperature profile. A positive stress drop is observed over a larger fault length than for depletion which leads to a larger seismic slip length L_5 (Figure 4-5h). However, the average stress drop over the ruptured area is larger for depletion (2.2 MPa) than for

cooling (1.1 MPa), because the aforementioned decreased normal stress for cooling.

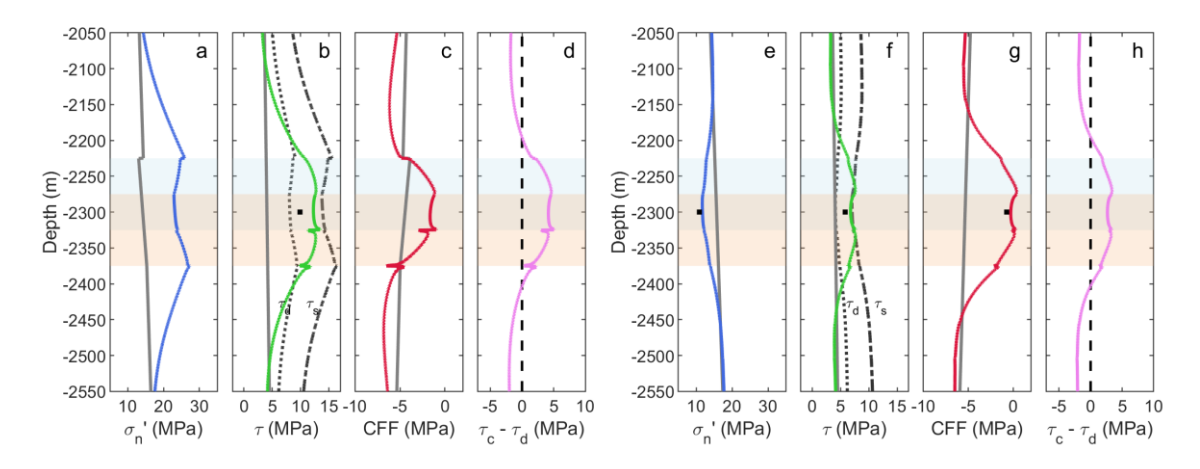


Figure 4-5 Stress changes on the fault for depletion (a-d) and cooling (e-h) for the default scenario. Grey lines: initial stress, colored lines: stress at the onset of fault reactivation. Fault reactivation occurs at $\Delta P_c = -24$ MPa for depletion and $\Delta T_c = -28$ °C for cooling. Reservoir footwall and hanging wall depth ranges are indicated with the lightblue and orange patches respectively. A, e) effective normal stress. B, f) shear stress (green line) and static and dynamic fault shear strength $\tau_s = \sigma_n' f_s$ (dashed-dotted line) and $\tau_d = \sigma_n' f_d$ (dotted line). C, g) Coulomb Failure Stress. D, h) available stress drop at the onset of rupture, defined as the difference between shear stress at reactivation τ_c and dynamic shear strength τ_d . Positive values allow rupture propagation. Dots in a-c and e-g indicate the stress change at ΔP_c and ΔT_c for the same input parameters but obtained for a laterally extensive reservoir (uniaxial strain conditions) on a fault without offset. L_s in d and h is the rupture length (fault length experiencing unstable fault slip) computed using LEFM after fault reactivation occurs.

4.4.3 Reactivation for depletion and cooling

In the first model ensemble the depletion of a laterally extensive reservoir was modeled, sampling from the uniformly distributed input parameters summarized in Table 4-1. The bar charts depicted in Figure 4-6 show the fraction of simulations where reactivation occurred within a certain range of ΔP plotted against the different input parameters. Grey bars indicate reactivation did not occur at all within the maximum pressure change. Note that for relatively critical initial stress ($K_0 < 0.7$) a number of simulations were discarded because the initial state of stress was already at failure.

Reactivation occurred in 20% of the model runs simulating depletion (Figure 4-6), and the probability of reactivation depended on many of the input parameters. The poro-elastic parameters Poisson's ratio v and Biot coefficient α (Figure 4-6p and q) clearly had large effect on ΔP_c as may be expected, with a higher probability of reactivation for lower v and higher α ; see also the stress path dependence

on these parameters in Figure 4-4. For the lowest v of 0.05 reactivation was observed for 50% of the simulations, whereas for v > 0.3 fault reactivation is barely observed. The important role of α and v on fault reactivation is also reflected in the higher regression coefficients (Figure 4-7a and c), with v having a slightly stronger effect than α .

However, the strongest effect on fault reactivation was observed for fault throw t, exceeding that of the poro-elastic parameters (Figure 4-6c, d Figure 4-7a, c). For reverse offsets or offsets close to zero the reactivation was much lower than for normal offsets, increasing to over 30% at normal offsets equal to the reservoir height. This emphasizes the role the shear stress enhancement that results from the offset reservoir geometry on fault reactivation. In addition, poro-elastic stress parameters Poisson's ratio v Biot coefficient α also had a significant influence on reactivation, as well the proximity of the initial (pre-depletion) stress to failure, notably the stress ratio K_0 (Figure 4-6i). Furthermore overpressure promoted fault reactivation, but the vertical stress and pressure gradients had little effect on reactivation. Also σ_{H}/σ_h and strike angle with respect to σ_H (ϕ) had minor effect on ΔP_c , likely due to the limited range in σ_H/σ_h . The dip played a bigger role, with the probability for reactivation increasing significantly towards 65 degree dip.

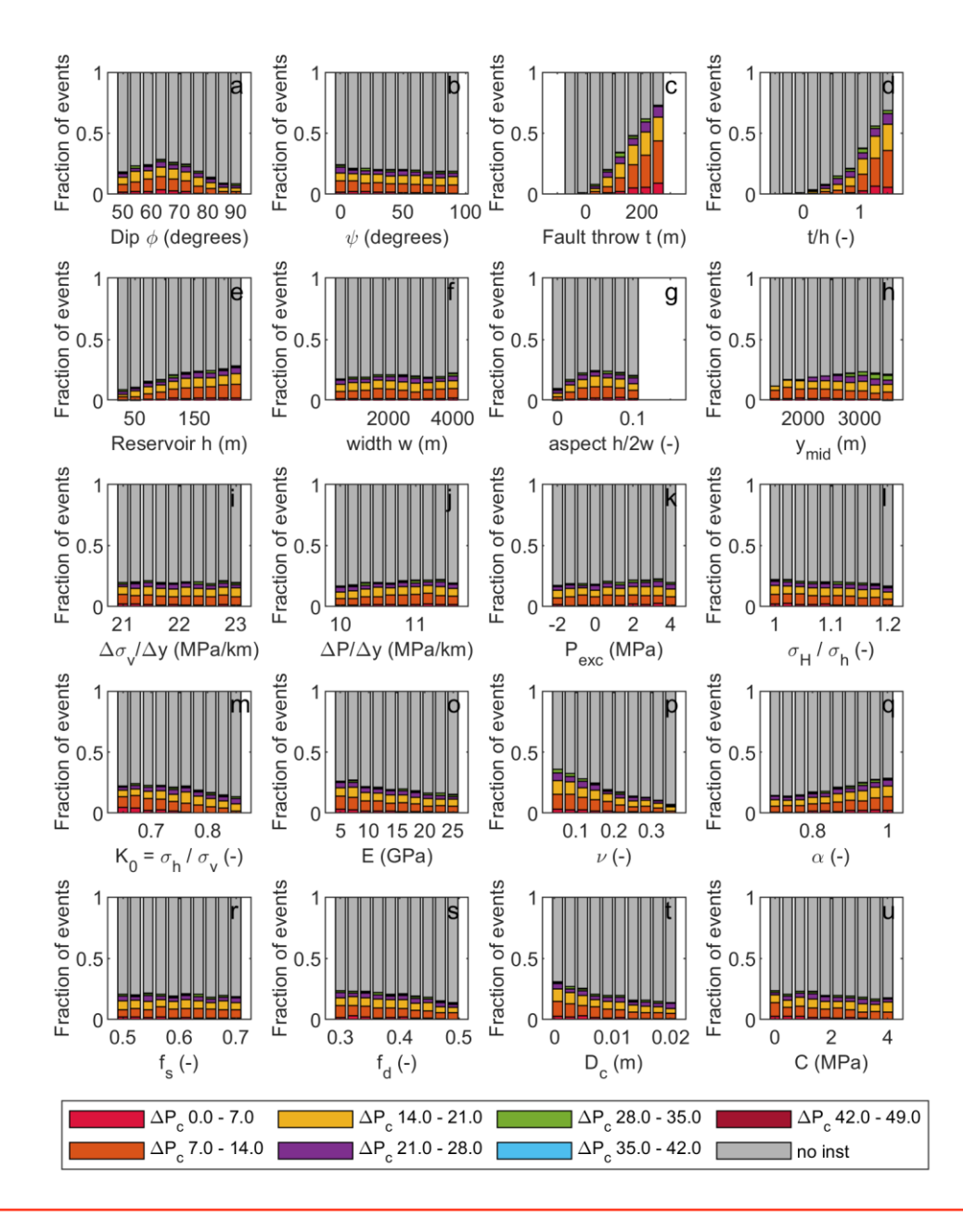


Figure 4-6 Effect of input parameters on the depletion pressure required for the onset ΔP_c . Bar charts were made by binning each input parameter into 10 bins, and dividing ΔP_c (MPa) into 8 categories, with 'no inst' indicating that instability did not occur for full reservoir depletion. The normalized fraction of events falling into each category is presented in the above figure; since sampling is done from uniform distributions, each bin represents ~1,000 simulations.

The friction parameters had a smaller effect on reactivation compared to the poro-elastic parameters, with the probability of reactivation decreasing mildly towards higher f_s and C (stronger faults) (Figure 4-6 r & u). Also D_c affected the reactivation pressure, with higher ΔP_c required for higher values of D_c (Figure 4-6t). This is because D_c , as well as f_d , E, and V determine the critical nucleation length L_c which must be reactivated before failure occurs (Equation 4-7), with L_c increasing from a few m to ~20 m. The critical nucleation length-scale also resulted in an effect of reservoir thickness. Whereas the magnitude of depletion-induced stress change was actually the same for the same normalized reservoir throw (t/h), thicker reservoirs result in broader stress peaks which reach the nucleation length at lower ΔP_c compared to thinner reservoirs. These observations underline the importance of the nucleation length-scale in relation to the reservoir length-scale, and the nucleation criterion that is used to pinpoint fault reactivation. Note however that the nucleation process is subject to large uncertainties; in the discussion we address potential effects that this may have.

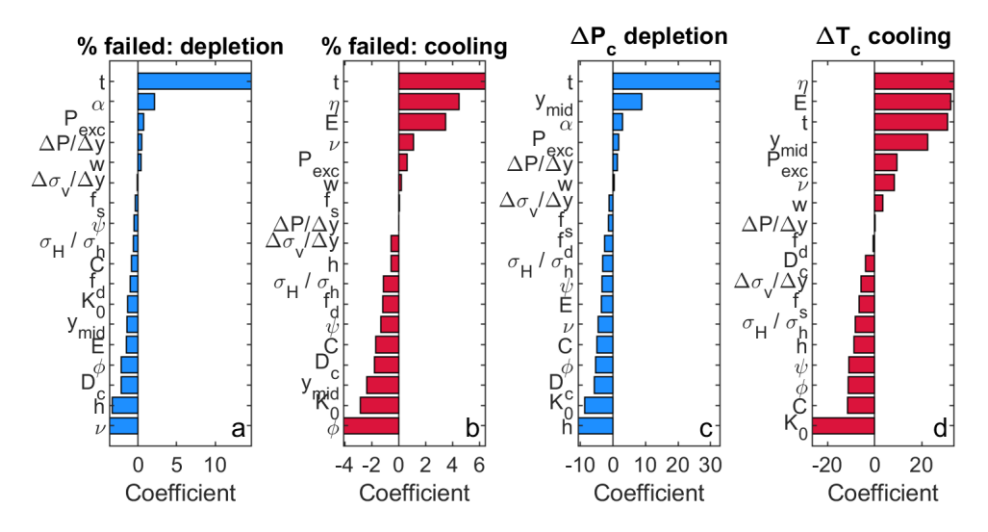


Figure 4-7 Regression coefficients for depletion- and cooling-induced fault reactivation. Logistic regression coefficients are shown for probability of failure (no instability vs reactivation) during depletion (a) and cooling (b), and linear regression coefficients are shown for the reactivation pressure change (c) and reactivation temperature change (d).

In the second model ensemble the effect of cooling was investigated. For the cooling scenario overall the percentage of failure occurring was much larger than for depletion, with 52% of the simulations reaching failure (Figure 4-8). The two most important parameters promoting reactivation were the thermo-elastic parameters Young's modulus E and linear thermal expansion coefficient η (Figure 4-8 o and q), both exhibiting a strong negative correlation with ΔT_c (Figure 4-7). Their effect is stronger than that of v and α for depletion. Throw had a strong effect, but less than for depletion, likely due to the difference in the diffusion length-scale (pressure changes decay more rapidly for the current set of input parameters than temperature changes). As for the depletion scenario, the parameters affecting initial stress played an important role for the temperature change required for the onset of failure ΔT_c . The relative strengths and signs of the regression coefficients of the initial stress parameters were similar, with K_0 again the most significant (Figure 4-8i), followed by the overpressure, vertical stress gradient, and horizontal stress ratio (Figure 4-7b). Also the correlation with depth was strong, as depth determined the maximum ΔT (i.e. the difference between initial reservoir temperature, which is dependent on depth and the temperature gradient, and the injection temperature).

To conclude, the poro-elastic or thermo-elastic rock parameters as well as fault throw, in-situ stress ratio K_0 remain crucial for reactivation for both cooling and depletion. The main difference between cooling- and depletion-induced reactivation was the dominance of Young's modulus and thermal expansion coefficient for ΔT_c compared to a relatively strong influence of throw on ΔP_c .

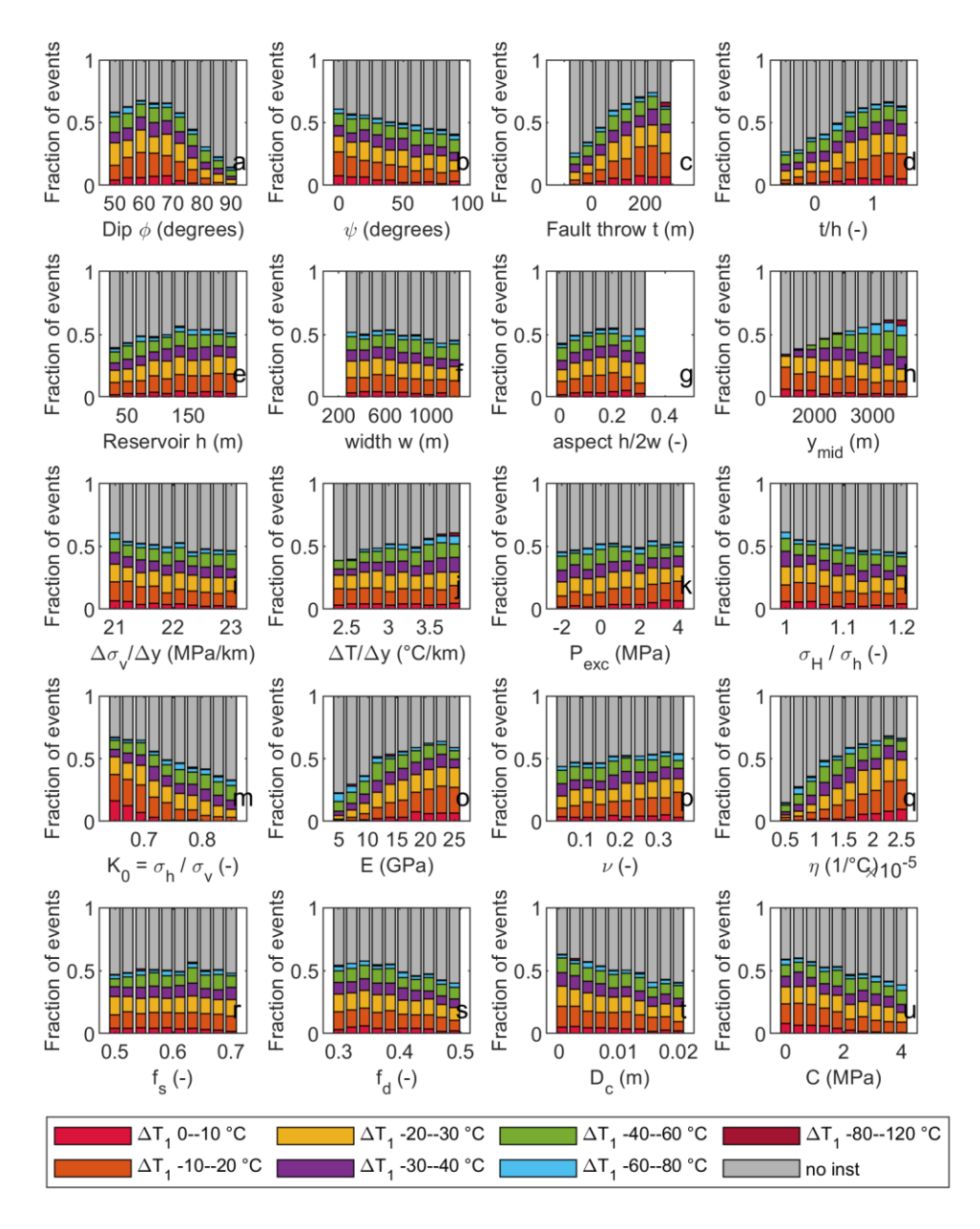


Figure 4-8 Effect of input parameters on the temperature change required for the onset of reactivation ΔT_c . Bar charts were made by binning each input parameter into 10 bins, and dividing ΔT_c (MPa) into 8 categories, with 'no inst' indicating that instability did not occur for full reservoir depletion. The normalized fraction of events falling into each category is presented in the above figure; since sampling is done from uniform distributions, each bin represents ~1,000 simulations.

4.4.4 Along-dip rupture length

After reactivation, the along-dip rupture length (i.e. length of the fault that slips during the seismic event) was computed semi-analytically using Linear Elastic Fracture Mechanics (LEFM). The along-dip rupture length is important, as together with the along-strike dimension and amount of fault slip

or the stress drop, it will determine the induced event magnitude. Whether rupture remains confined to the reservoir interval or not is thus an important issue for assessing e.g. the maximum magnitude that could be induced. Rupture lengths are shown for depletion and cooling in Figure 4-9, and relative importance of input parameters is shown in Figure 4-10.

Rupture lengths ranged from several 10's to 100's m (Figure 4-9), and rupture lengths were larger for the cooling reservoir than for the depleting reservoir. For both depletion and cooling the rupture lengths increased with a more critical tectonic state of stress and/or more frictional weakening . A convenient measure to combine both these two factors is the ratio between the available stress drop at the onset of reactivation and the strength drop $(\tau_c - \tau_d) / (\tau_s - \tau_d)$. This is a measure of both the criticality of the initial stress τ_0 (which is a function of K_0 , dip, $\Delta \sigma_v / \Delta y$ etc.) and the frictional weakening parameters. The numerator $\tau_0 - \tau_d$ controls the energy available for rupture, and $\tau_s - \tau_d$ is a measure of the fault strength. Large ruptures propagating far beyond the reservoir interval require a positive $\tau_0 - \tau_d$ (energy is supplied from the medium around the fault), whereas a negative $\tau_0 - \tau_d$ will lead to rupture arrest (energy is consumed as rupture propagates) (Buijze, 2020; Galis et al., 2019; Galis et al., 2017). Indeed this can be observed in Figure 4-9, where the largest rupture lengths occur as $(\tau_0 (\tau_d)/(\tau_s-\tau_d)$ approaches or exceeds 0. Some rupture at these higher stress/strength drop ratios could even propagate far outside the reservoir interval (run-away). On the other hand, for lower stress/strength drop ratios most seismic events remained confined to the reservoir interval - i.e. fault slip only occurred within or close to the reservoir, which is best seen using the normalized rupture length L_s / (h + t) in Figure 4-9 c and d. Both initial stress and dynamic weakening parameters are thus crucial in determining whether rupture can propagate beyond the reservoir interval and grow into a larger event. Here a large range of in-situ stress was evaluated; if this range can be better constrained from data the range of computed rupture lengths will be narrowed.

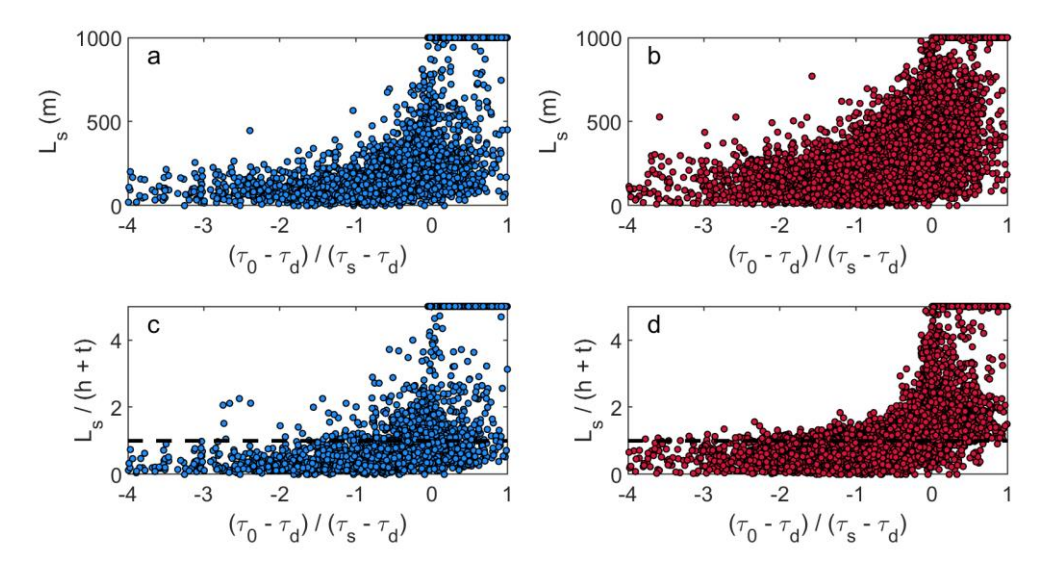


Figure 4-9 Along-dip rupture lengths for depletion (blue) and cooling (red) as a function of initial stress state and frictional weakening parameters. Rupture lengths (L_s) were computed after reactivation occurred, using Linear Elastic Fracture Mechanics (see 4.3.5), and are plotted against the ratio of stress drop ($\tau_0 - \tau_d$) and strength drop ($\tau_s - \tau_d$) of the background tectonic stress. Ruptures that propagate indefinitely (run-away) have been truncated at 1000 m (a,b) or 5 (c, d). Absolute rupture lengths along the fault dip are shown for a) depletion and b) cooling, and rupture lengths normalized for reservoir height + throw are shown for c) depletion and d) cooling. The dashed line indicates a normalized rupture length equal to the height of the reservoir interval

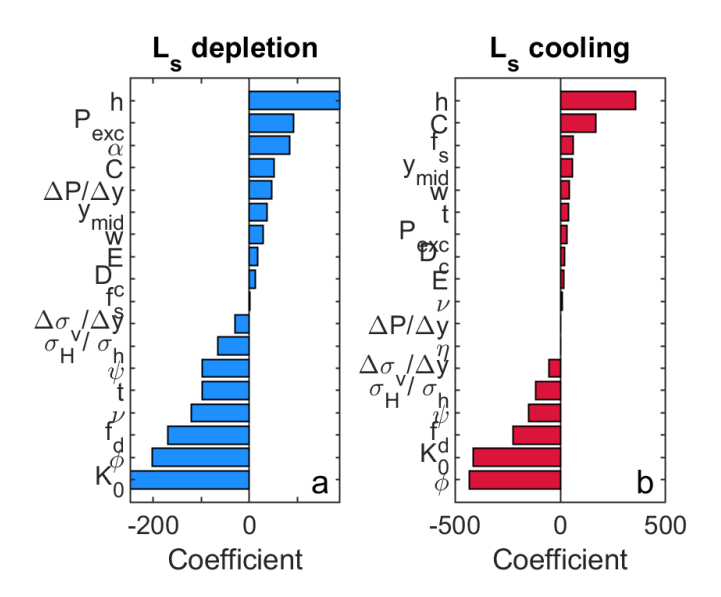


Figure 4-10 Linear regression coefficients for input parameters in relation to the seismic slip length along the fault (L_s). Scenario's without reactivation have been omitted from the regression, as well as scenario's where run-away rupture occurred (i.e. rupture growing indefinitely).

The effect of initial stress and dynamic weakening are also manifest in the regression coefficients (Figure 4-10). For both depletion and cooling-induced events, the three most important parameters for rupture size were initial stress ratio K_0 and fault dip \mathcal{O} (which determine τ_o and σ_{n0} ') and the dynamic friction coefficient f_s . The lower these three parameters, the larger the seismic slip event. Furthermore the reservoir height h played an important role as it control the length-scale of the reservoir formation and the length of the depletion- or cooling-induced stress perturbation, and hence the length-scale of ruptures confined to the reservoir interval. Note that although ruptures were slightly larger for cooling-induced events, the relative importance of input parameters is the same for depletion and cooling. This is contrary to what was observed for fault reactivation, where different input parameters played a role (Figure 4-7). So even if the mechanisms for reactivation are different, once the fault is reactivated, the (maximum) along-dip rupture size will be determined largely by reservoir dimensions, dynamic weakening parameters, and the initial, tectonic + induced shear stress on the fault.

4.5 Discussion & Conclusions

The onset of induced rupture (fault reactivation) and rupture lengths were compared for a depleting and a cooling formation, using a simplified, 2D plane-strain, stochastic geomechanical model. Although the geometry was simplified, the model does capture the effect of fault offset on the induced stresses as well as frictional weakening behavior controlling the seismic slip length along the fault dip. Here we discuss the main observations in relation to other works, the assumptions, and the implications.

4.5.1 Depletion-induced fault reactivation: comparison with previous works

The mechanisms of depletion-induced seismicity have been investigated quite extensively in a number of other geomechanical studies, ranging from 2D models similar to the current model geometry (e.g. Buijze et al., 2017, 2019; Jansen et al., 2019; van den Bogert, 2015, 2018; van den Bogert et al., 2020; Wassing et al., 2017; Zbinden et al., 2017), disk-shaped models (Mulders, 2003; Orlic et al., 2013) to 3D field-scale models with realistic fault geometries (van Wees et al., 2019; Candela et al., 2019). The added value of the approach presented here is the stochastic component in which large uncertainty in input parameters is accounted for, the inclusion of pressure diffusion,

and the coupling of the stress changes to a physics-based calculation of rupture length (using LEFM) and stress drop. The advantage of using LEFM over fully dynamic simulations as performed in Buijze et al. 2017, 2019 is the computation speed which allows stochastic analysis, whilst the accuracy of the computed rupture sizes is within 10% of the fully dynamic results (Buijze, 2020). Even though the model geometry is relatively simple compared to some of the 3D simulations, the stochastic analysis reveals which parameters are of key importance. This gives important guidelines and constraints for more complex modeling approaches as in e.g. Chapter 5. For depletion the pressure change required for the onset was governed mostly by the poro-elastic rock parameters, fault throw, stress ratio K_0 , dip, and reservoir depth. Note that the effect of reservoir depth will largely disappear when considering the normalized pressure change $(\Delta P/P_0)$ rather than the absolute pressure change because the maximum reservoir pressure and hence the maximum pressure decrease increased with depth. These findings are in line with the aforementioned works on depletion-induced stress changes where e.g. the effect of fault throw on fault reactivation was recognized, or rather the fault throw normalized by the reservoir thickness, with the most stable configuration found for zero offset, and the most unstable configuration found for fault throws equal to the reservoir thickness (Buijze et al., 2019; Jansen et al., 2019; Mulders, 2003; Orlic & Wassing, 2013; van den Bogert, 2018; Zbinden et al., 2017). Reverse throw configurations are more stable than normal fault configurations. The quantitative comparison in our study indeed shows fault throw to be the most important parameter for the reactivation pressure. Note that the importance of throw will depend on model resolution, and/or the critical fault length for reactivation, and the hydraulic diffusivity of the seal and the base; the more the stress concentrations are smoothed because of e.g. element size, the less dominant throw will become. The poro-elastic rock parameters were also important as may be expected. However, in the current study the rock properties were assumed linear elastic, and uniform throughout the model space. In reality stiffness contrasts may exist between the seal and base formation with respect to the reservoir, see e.g. Section 5.4.5 Section A.3. These could lead to additional stress concentrations that are not considered here, as shown in Figure 5-12.

4.5.2 Cooling-induced fault reactivation

Whilst many studies have been dedicated to depletion-induced fault reactivation, less work has been targeting fault reactivation for doublet operations in sandstone reservoirs, in particular using offset reservoir compartments. One difference between the doublet operations modeled here and e.g. an Enhanced Geothermal System in fractured rock is the very small pressure increase around the injection well in such a porous sandstone formation. Stress changes will thus be dominated by cooling. A simple comparison of poro-elastic and thermo-elastic stress path parameters already reveals thermo-elastic stresses can be significant (Soltanzadeh & Hawkes, 2009, Figure 4-4). Our stochastic analysis shows thermo-elastic stresses due to cooling of sandstone reservoirs are equal to or larger than depletion-induced stresses in the same reservoirs, and lead to a higher probability of reactivation. Note that the difference between the cooling and depletion stress is dependent on the difference between the minimum injection temperature that is allowed (here: 20°) and in-situ temperature, versus the maximum depletion pressure that is limited by the initial pressure for depletion. In addition the model is plane-strain, which overestimates stress changes with respect to the more applicable axisymmetric case (Soltanzadeh & Hawkes, 2009, Section 6.1). Note also that uniform cooling was assumed in the reservoir formation and that it is assumed the fault lies within the depleted or cooled volume, which tends to overestimate the stress changes. Whereas this assumption is realistic for intra-reservoir faults in depleting gas fields, cooling is more local than gas depletion, typically occurring within a radius of several hundreds of meters from the injection well (e.g. van Wees et al., 2020, Section 3.4.1, Figure 4-3). Stress changes are largest within the cooled zone and decay rapidly outside of it (Section 3.4.1). The current model assumption could be seen as a worst-case scenario where an undetected fault lies close to the injection well. If the location of faults is well known, other tools could be used to estimate a safe distance from known faults, such as SRIMA (Chapter 3) or a FE analysis such as presented in the next chapter. Note that even though the model geometry may represent a worst-case scenario, still in 48% of simulations reactivation did

not occur. The current study aids in defining under which conditions reactivation could or could not occur; when more data is available for a specific location the reactivation potential could be refined. For cooling the temperature change required for onset of fault reactivation was controlled by the Young's modulus E, thermal expansion coefficient η , and stress ratio K_0 , with smaller dependence on fault throw than for depletion. Compared to depletion, thermal diffusion extended further into the seal and base leading to a smaller shear stress increase in the reservoir itself. In reality, the temperature field around the fault will be smoother than in the current model setup because thermal conduction to all directions will occur, also fault perpendicular which further reduces the temperature contrast across the fault which in turn may lead to even lower shear stress changes, closer to those of uniaxial cooling. The role of fault throw may thus be even smaller when considering more realistic temperature fields. This may imply that tools as SRIMA, which do not incorporate fault offset, could present a satisfactory (first-order) approach for fault reactivation (see Section 6.1 for a comparison). Note that for depletion also pressure diffusion occurs, which smoothens the stress profile concentrations. Hydraulic and thermal diffusivities were not varied in this study; it is recommended to evaluate these parameters to asses relative length scales of pressure and temperature diffusion in future models. The smoother the PT distribution along the fault, the smoother the stress changes.

This relative importance of the input parameters also underlines the importance of characterization of different geothermal reservoirs, not only in terms of pre-existing faults but also in terms of rock mechanical parameters, as for example stiffer reservoirs may be more prone to large stress changes and hence fault reactivation. On the other hand, weaker rock types, such as unconsolidated sandstone formations, may generate smaller stress changes and present a lower risk of fault reactivation and seismicity. In such rocks, inelastic deformation may also play a large role. The effect of inelastic behavior on thermo-elastic stress needs to be investigated. The elastic parameters are also important for the risk of fracturing; the normal stress decrease may be large enough to create new tensile fractures, such as in volcanic geothermal fields where temperature differences are much larger, or in very stiff rock types. Tensile fracture is not considered here, but when seal and reservoir integrity are investigated we recommend to incorporate an analysis of tensile fracturing potential. For induced seismic risk tensile fracturing is not considered important, as seismic events resulting from tensile fracturing are typically small. In addition to the elastic properties of the formations, also the static fault friction and cohesion along the fault is expected to vary across different formations cut by faults. It is recommended to evaluate this heterogeneity in future studies (see also next section).

4.5.3 Rupture lengths and potential for rupture to propagate outside of the reservoir interval

Using Panther2D the along-dip rupture length can be computed based on the energy available for rupture (LEFM approach), taking into account frictional weakening of the fault following reactivation. This rupture length is important, as together with the along-strike dimension of rupture it will determine the total fault area experiencing seismic slip. This area, together with the stress drop resulting from fault weakening, determines the event magnitude. Important here is whether the rupture can grow far beyond the volume perturbed by the cooling; if it does not the maximum earthquake size will be largely controlled by the perturbed fault area. For cooling, several 10s of m of seal and base rocks may also cool down due to diffusion, extending the perturbed area above and below the aquifer. This promoted rupture propagation into those cooled parts of the seal and base. Temperature and pressure diffusion are thus important to take into account when estimating event sizes. In previous studies investigating depletion the hydraulic diffusion effect was not taken into account (e.g. Buijze et al., 2019); however, here it is shown that inclusion of pressure diffusion reduces the stress concentrations in the reservoir but will increase the fault area affected by the pressure perturbation.

In Section 4.4.4 it was also observed that rupture only extended far beyond the reservoir interval for low values of in-situ stress ratio K_0 and/or low dynamic friction. In the current model setup, uniform

distribution of in-situ stress rate and friction were assigned to the formations and fault. However, geothermal operations in the Netherlands target layered sedimentary sequences in which stresses and friction may vary per lithology. In the West Netherlands Basin for example, geothermal target formations are comprised of sandstone members, overlain by or interbedded with claystones or siltstones (Willems, 2020). In these sequences the in-situ stress may vary depending on the lithology. For example, minimum stress measurements in a tectonically quiet sedimentary basin in the USA at depths 1-2 km show that σ_h in mudstone formations was close to the lithostatic values, whereas the σ_h in the sandstones was significantly lower, down to 10 MPa lower (see schematic illustration in Figure 4-11. In absence of high tectonic loading, the creep behavior of the mudstones relaxes the differential stresses in these formations. Near-isotropic stresses are also seen in other creep-prone lithologies such as argillite (Wileveau et al., 2007) and within or close to salt formations (Rioseco et al., 2013, Farsimadan et al., 2020). These near-isotropic stresses mean the in-situ shear stresses on the fault are low, which is very unfavorable for rupture propagation. Hence if clay-rich seal and base formations are present above and below the targeted aquifer, rupture propagation outside of the aquifer may be unlikely. In-situ stress data is needed to check whether higher or near-isotropic stresses are indeed observed in clay-rich formations. As part of WarmingUp 4B, leak-off test and minifrac data are being analyzed, looking at distinct trends per region and/or lithology in the Netherlands. Results from this analysis will be reported at a later stage, with implications for the rupture potential in Dutch lithologies.

Rupture length is heavily dependent on the amount of frictional weakening that can occur on faults. Of all the input parameters, this is likely the most uncertain factor. Knowledge of the dynamic weakening behavior of fault rocks can be obtained in the laboratory, or from seismological observations. In the laboratory, it is challenging to reproduce the rapid accelerations and high, seismic velocities $(0.1-1~{\rm ms^{-1}})$ at the in-situ conditions $(\sigma_n'>20~{\rm MPa}, T~100^{\circ}{\rm C})$, including e.g. in the presence of pore fluids. Low-velocity experiments indicate that sedimentary rock types are in fact more prone to stable behavior than unstable, seismic behavior. Recent high-velocity experiments on sedimentary fault gouges however show frictional weakening down to f_d of $^{\sim}0.3$, at slip rates and slip distances relevant for 'smaller' sized induced earthquakes (M3-4) (Hunfeld, 2020). However, other experiments also showed significant cohesion could develop on inactive faults in sandstone and evaporites, e.g. on faults in the Netherlands (Hunfeld, 2020). This could lead to an extra stress drop, and an additional mechanism for fault weakening and seismicity. Cohesion and cementation are therefore important factors to determine per target formation.

In addition, fault properties vary per lithology as, in particular for relatively small-displacement faults, the fault rock materials may be largely derived from the wall rock. Clay-rich fault rock have a lower static friction, and do not exhibit healing and thus are unlikely to build up significant cohesion (Hunfeld et al., 2020). They are also more prone to aseismic slip. Sandstone fault gouges are stronger, and may develop cohesion. Also, the amount of weakening and the fracture energy will vary with fault lithology (Hunfeld, 2020). This affects the rupture propagation as well (e.g. Buijze, 2020). It is recommended to include frictional variability in future studies. Also, under the conditions of interest it is possible that fault slip occurs aseismically and via slow slip transients. Such non-seismic behaviors are also observed along plate boundaries (e.g. Ito et al., 2007) and are the results of heterogeneous stress or heterogeneous fault properties with brittle asperities within creep-prone fault materials. It is important to investigate whether this is likely to happen in Dutch geothermal doublets targeting shallow sedimentary formations; if a substantial part of the deformation is accommodated aseismically seismic hazard could be low even if faults are reactivated. This needs to be confirmed by laboratory experiments and field data – e.g. monitoring of seismicity and deformation using tiltmeters, fiber optics, geophones measuring low frequencies.

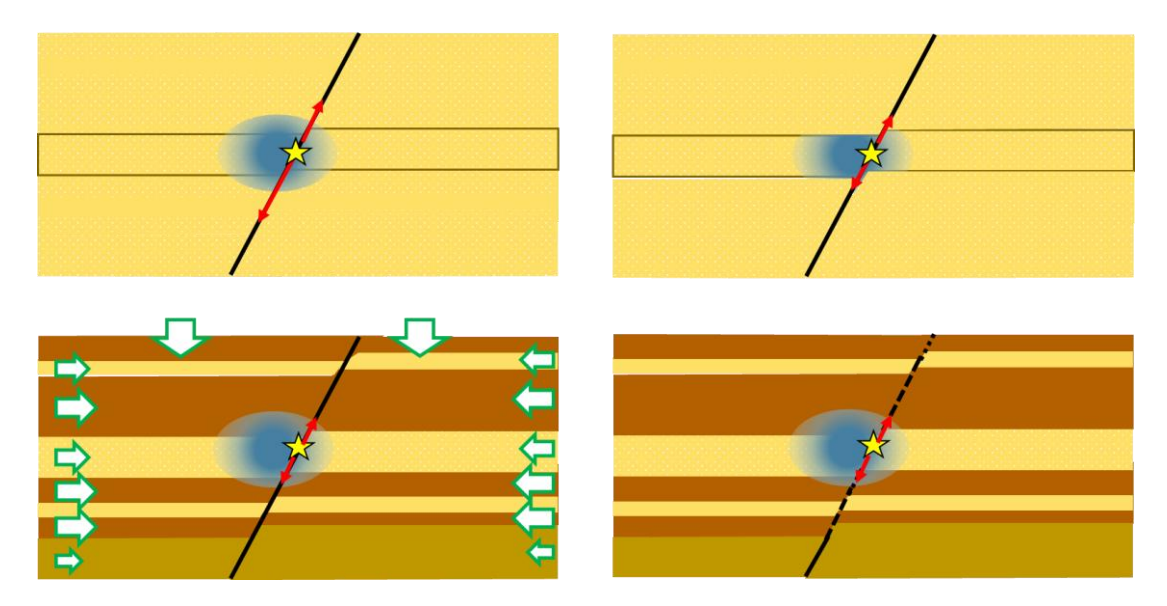


Figure 4-11 Schematic illustration of model assumptions that will affect rupture propagation along the fault dip. A) uniform properties, b) effect of ignoring pressure or temperature diffusion into the seal and base, c) heterogeneous, lithology-dependent horizontal stresses, d) heterogeneous, lithology-dependent fault properties (e.g. cohesion, friction).

4.5.4 Implications for induced seismicity in geothermal doublets

Our study shows that cooling-induced stress changes are significant and could lead to fault reactivation if a fault is present within the cooled volume. To avoid fault reactivation, it is thus important to stay away from known faults. The safe distance from known faults could be determined to a first order using e.g. Equation 4-2, or better using SRIMA (Chapter 3), which better captures the temperature field and also allows for stochastic variability to be taken into account

In our study we have taken a generic set of input parameters relevant for upper crustal conditions in sandstone reservoirs in the Netherlands. This helps to understand the relative importance of the different input parameters, but to apply the model better constraints on the input and a validation to field data is essential. The input distributions could be populated with location-specific parameters, to e.g. differentiate between regions in terms of reactivation potential. If for example one region would have thinner formations of higher porosity and hence a lower stiffness, the reactivation potential would differ from a region with thicker formations and a higher stiffness. The model could also be linked to spatial data available in the public domain, such as ThermoGIS where thicknesses, permeabilities, depths, etc. are available, to generate a region-based reactivation potential. This could be improved with laboratory data on samples from different geothermal targets, as planned in WarmingUp 4B. Note that in addition to the frictional weakening parameters, in all cases information on the initial tectonic stress remains one of the key (unknown) input parameters; it is important that this stress is better quantified in a region-specific and lithology-specific analysis. Such an analysis is also foreseen in WarmingUp4B.

4.6 Conclusions & Recommendations

Chapter 4 presents a fast model approach to compute stress changes, reactivation, and rupture for uniform depletion or cooling in a faulted reservoir. The model assumptions are: 2D plane-strain model, seal-reservoir-base stratigraphy with uniform linear elastic properties, fault flanked by two reservoir compartments of width w, uniform cooling occurs within these compartments, and reservoir compartments are offset by the fault. Such a tool can be used for e.g. quick assessment of fault reactivation, identification of key parameters for reactivation and rupture sizes. In this chapter stochastic analysis was performed to compute the fault reactivation potential and rupture sizes, and to rank the input parameters. The main conclusions are as follows:

- Cooling-induced stress changes are larger than for depletion, which is reflected in a higher fault reactivation potential for cooling. This is because the effective normal stress decreases during cooling but increases during depletion. Note that this conclusion holds for faults that lie within the cooled or depleted area.
- Fault reactivation for depleting reservoirs was strongly controlled by fault throw, the poroelastic stress parameters Poisson's ratio v and Biot coefficient, and the initial stress ratio K_0 .
- Fault reactivation for cooling reservoirs was mostly influenced by the thermo-elastic parameters Young's modulus E and linear thermal expansion coefficient η as well as the fault throw initial stress K_0 .
- For both depletion and cooling, reverse faults are less likely to be reactivated than normal faults.
- Taking into account the finite width of the cooled zone reduces the potential for fault reactivation, but mostly so when the width is small compared to the reservoir height. This could e.g. be during initial stages of injection, and/or for very thick reservoirs.
- Along-dip rupture length was mostly controlled by the initial stress ratio K_0 , fault dip and the frictional weakening parameters, for both cooling and depletion.
- In addition, reservoir thickness and fault throw influenced rupture length, with thicker reservoirs causing larger events.
- Rupture lengths are larger for cooling but the stress drop is smaller, as the normal stress has been reduced during cooling.

5 Fault reactivation potential near a geothermal doublet: a 3D model

5.1 Abstract

Understanding the mechanics of fault reactivation is crucial to understand and potentially mitigate felt seismic events in geothermal doublets. Geomechanical models can shed light on important processes, key geological properties, and operational settings affecting fault reactivation, though for predictive power such models should always be validated against field and/or monitoring data. The previous two chapters have focused on fast model approaches to give a first order assessment of fault reactivation, and in case of PANTHER2D, rupture lengths. The advantage of these methods is their speed which allows for stochastic analyses and incorporation of uncertainties. The draw-back of these fast approaches is the lack of the third dimension and subsurface heterogeneity like stiffness contrasts. 3D Finite Element analysis can be used to model fault reactivation in 3D, taking into account the spatio-temporal evolution of the cooling front, offset fault geometries, stiffness contrasts, etc. Such an analysis is complementary to the analyses in the previous 2 chapters, incorporating less parameter uncertainty but a higher degree of subsurface complexity. In this Chapter we present such a 3D model workflow of reactivation in and around a geothermal doublet. The 3D models geometry consists of a seal, reservoir, and base stratigraphy that is offset by a 2D fault. Pressure and temperature fields in these formations were computed in Open Porous Media (OPM), and imported into DIANA FEA to compute poro-thermo-elastic stress changes. Fault stress changes for various doublet configurations are evaluated. Additionally, the results are compared to the two fast models SRIMA and PANTHER2D presented in the previous two sections, to define when and where the fast models could be employed, and where a 3D approach is warranted. The results are summarized as follows:

- Stress changes are almost solely determined by cooling; the pressure changes around the injection and production well remain limited.
- Circa 50 100 m of the seal and base formation are also cooled for the current thermal parameters.
- The cooling front becomes increasingly asymmetric with increasing operation time, growing preferentially in the direction of the production well.
- The extent of the cooling front perpendicular to the doublet orientation matches relatively
 well with SRIMA and the cooling front predicted by the heat balance equation. The largest
 differences occur in the doublet-parallel orientation because of the asymmetry mentioned
 above.
- Cooling of parts of the fault results in a decrease in effective normal stress and increase in shear stress, with the net effect a positive Coulomb stress change (destabilizing)
- When the cooling front has reached the fault a spherical (doublet fault-perpendicular) or elliptical (doublet fault-parallel) area of higher Coulomb stress develops.
- The cooling-induced Coulomb stress reaches its maximum at depths where reservoir is juxtaposed against reservoir, and decreases gradually towards the seal and the base.
- For stiffer seal and base the Coulomb stress changes in the seal and base exceed those of the reservoir. Stiffer seal and base hence promote reactivation and lead to a larger depth interval that is affected by the stress changes.

5.2 Introduction

Understanding the mechanisms of stress changes around geothermal doublets, and the conditions under which faults could be reactivated and the magnitudes of induced events, is crucial for sitespecific hazard assessment and the development of mitigation measures. In the previous two chapters fast, semi-analytical tools for fault reactivation near geothermal doublets were presented; SRIMA and PANTHER2D. SRIMA calculates poro-thermo-elastic stress development around an injection well, and the resulting fault criticality with distance from the well, without explicitly modeling the fault itself. PANTHER2D focuses on the effects of fault geometry and fault weakening on reactivation and rupture: a simpler, uniform pressure or temperature field is prescribed within the reservoir and the resulting poro- and or thermo-elastic stress changes are computed on and around a fault that offsets the reservoir. Fault reactivation is modeled, as well as the along-dip rupture length with the incorporation of fault weakening behavior. Both models are fast and allow for stochastic analysis. However, in order to be fast and allow for the analytical calculations both models have also made several simplifying assumptions that could affect fault reactivation. For SRIMA these include the assumption of radial symmetry and lack of a production well, the limited incorporation of stiffness contrasts between formations and the lack of realistic fault geometries (e.g. fault offset). For PANTHER2D these include the lack of the third dimension, the very simple PTfield of uniform temperature and/or pressure changes in the reservoir and the absence of stiffness contrasts between formations. In this chapter we present a third approach, namely a 3D Finite Element modeling workflow which models the full 3D stress development around an injection well and can incorporate subsurface complexities as stiffness contrasts and faults offsetting the reservoir. Pressures and temperatures are computed in Open Porous Media flow simulator and one-way coupled to stress changes in DIANA FEA. This is similar to the approach of Wees et al. 2020 using MACRIS, but through the use of Finite Elements a higher degree of complexity could be incorporated, e.g. the aforementioned stiffness contrasts, but also reservoir elastoplasticity etc. (Buijze, 2020).

5.3 Methods

Poro-thermo-elastic stress changes are computed in a coupled workflow consisting of reservoir simulator Open Porous Media Flow (OPM Flow) (Rasmussen et al., 2021) and DIANA Finite Element Analysis. OPM is run within the RoSim reservoir simulation workflow developed by TNO. A one-way coupling is assumed between the pressure and temperature changes and the stress changes and deformation (Figure 5-1) - i.e. deformation of the porous medium is assumed not to affect the pressure and temperature evolution. The same model geometry is assumed in OPM and DIANA FEA. In the following section the model geometry, pressure and temperature modeling, the stress modeling, and input parameters are introduced .

Pressure & Temperature

Open Porous Media (OPM)

Within RoSim reservoir simulation workflow for geothermal systems

One-way coupling PT - mechanics

Mechanics

DIANA Finite Element Analysis v10.4

Post-processing Matlab

Figure 5-1 3D model workflow. Pressure and temperature are computed in OPM Flow and one-way coupled to DIANA FEA

5.3.1 Model geometry

The model geometry consists of a generic seal – reservoir – base stratigraphy, with a fault offsetting the three formations with a throw t – i.e. vertical offset (Figure 5-2). The reservoir thickness h has a default value of 100 m, with a default throw of 0.5 h (50 m). The thickness of the seal and base are set to 150 m. The center depth z_{mid} of the reservoir is defined similar to y_{mid} of PANTHER2D (halfway between the top of the footwall and base of the hanging-wall, and has a default depth of -2300 m. The width of the model is 5000 m in both dimensions.

An injection and a production well are placed in the model in various configurations (Figure 5-3). Both fault-perpendicular and fault-parallel scenarios are evaluated. The doublet spacing is 1400 m. In two of the scenarios the wells are located 750 m from the fault, in the other two scenarios the injection well was placed 100 m from the fault. The 100 m scenario represents a worst-case scenario where e.g. an undetected fault is present near the well, as in PANTHER2D.

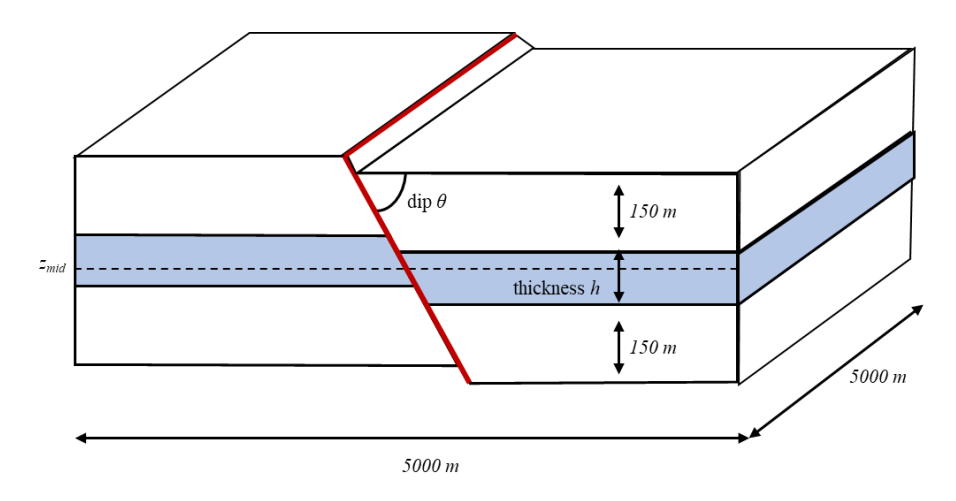


Figure 5-2 Model geometry consisting of a seal – reservoir – base stratigraphy. A fault offsetting all three formations with vertical offset t is present in the center of the model.

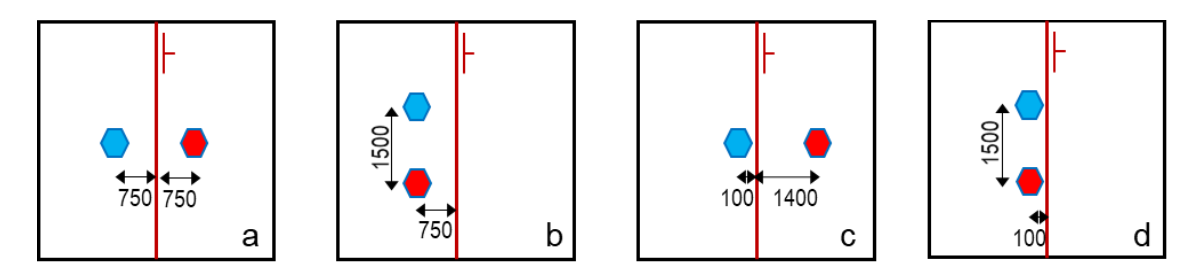


Figure 5-3 Well configuration scenario's shown in map view at a depth of zmid. Blue: injection well, red: production well.

Table 5-1 Overview of default input parameters used for the OPM-DIANA workflow.

Parameter	Symbol	Unit	Default parameter
Mid depth	Zmid	m	2300
Reservoir thickness	h	m	100
Dip	θ	0	70
Vertical stress gradient	$\Delta \sigma_{v}/\Delta y$	MPa/km	22
Stress ratio σ_h / σ_v	K_0	-	0.75
Horizontal stress ratio $\sigma_h / \sigma H$	σ_H/σ_h	-	1.0
Strike with respect to σ_H	φ	deg	0
Pressure gradient	$\Delta P/\Delta y$	MPa/km	10.5
Overpressure in the reservoir	P_{exc}	MPa	0
Temperature gradient	ΔΤ/Δy	°C/km	31
Subsurface temperature at surface	T_0	°C	10
Biot coefficient	α	-	1
Poisson's ratio	ν	-	0.2
Young's modulus	E	GPa	15
Linear thermal expansion coefficient	η	°C -1	1 · 10-5
Static friction	f_s	=	0.60
Cohesion	C	MPa	0
Permeability	k	mD	500
Overburden permeability	k_{seal}	mD	3.0 · 10-5
Mass injection rate	q	kg/s	70
Injection Temperature	T_{inj}	°C	20
Rock thermal conductivity	K_{rock}	W/m.K	3
Injection water density	$ ho_w$	kg/m3	1052
Specific heat capacity water	C_{fluid}	J/kgK	3774
Specific heat capacity rock	c_{rock}	J/kgK	850
Rock density	$ ho_r$	kg/m3	2200
Water viscosity at 80°C	μ_{c}	Pa.s	0.5 · 10 ⁻³

5.3.2 Pressure and temperature calculation

The pressure and temperature fields resulting from fluid circulation in the geothermal doublet were computed using Open Porous Media (OPM) Flow reservoir simulator (Rasmussen et al., 2021), using single-phase flow (water). OPM was run within the TNO in-house RoSim reservoir simulation workflow. A static flow model with geometry and well placement as described in Figure 5-2 was generated, with a cell size of 50 m in the horizontal plane and 10 m in the vertical direction, similar to van Wees et al., 2020. The open hole section of either well is limited to the reservoir thickness h. Reservoir permeability is set to 500 mD both vertically and horizontally, whereas the seal and base are assumed impermeable 3x10⁻⁵ mD; the same as the input properties used in SRIMA (Chapter 3, Table 5-1). The same parameters are also assumed for the rock heat capacity (3 W/kg/K) and thermal conductivities (Table 5-1). The fault is assumed to have the same properties as the adjacent reservoir section; in this report we do not consider (partly) sealing faults. A constant flow rate with a default of +-70 l/s (250 m³/hr) is imposed at the injection and production well – i.e. balanced circulation. The initial fluid density, viscosity, and fluid heat capacity depend on temperature, pressure, and salinity,

and is computed using Batzle & Wang 1992 (see Table 5-1 for values at 80 degrees, ambient reservoir pressure, and 100000 ppm salinity). Density, viscosity, and fluid heat capacity are however kept constant during the flow simulation.

5.3.3 Poro-thermo-elastic stress calculation

The FE model was built using the same geometry as specified in Figure 5-2. Displacement boundaries were imposed at the base and sides of the model space to prevent motion perpendicular to the base or sides. Linear elasticity is assumed for the formations, with default values as presented in Table 5-1. Linear wedge (TP18L) and brick (HX24L) elements are used for the mesh of the formations, and planar interface elements are used to model the fault. The element size at the fault in the reservoir is 10 m, increasing to a maximum element size of 25 m in the reservoir and 100 m in the seal and base formations, yielding a total element number of ~250,000 elements. Smaller element sizes are not feasible in terms of memory and calculation time.

The vertical stress is initialized by application of gravity to the formations and an added overburden load to simulate the weight of the formations at depth shallower than 1900 m. The total horizontal stress is set using the K_0 stress ratio, with its default value of 0.75. The initial pore pressures are set using a constant pressure gradient function. The pressure and temperature fields computed in OPM are mapped onto the DIANA FEA mesh using the LinearNDInterpolator function in Scipy. The stress changes resulting from the changes in pressure and temperature over time can then be computed. Stress changes on the fault are expressed in shear and normal stress changes, as well as the Coulomb Failure Stress (CFF)

$$CFF = \tau - (C + f_S \sigma'_n)$$
 5-1

Here shear stress τ is the along-dip shear stress, with positive values promoting normal faulting, σ_n' is the effective normal stress, f_s is the static friction (default 0.6), and C is cohesion (default 0 MPa).

5.4 Results

5.4.1 Doublet parallel to fault – injection well at 750 m

The first scenario considers injection at 750 m from the fault in the footwall block. Pressure and temperature distributions at z_{mid} are shown in Figure 5-4 and Figure 5-5. Pressure changes remain limited, mostly below 0.5 MPa except in the direct vicinity of the injection well (Figure 5-5). Temperature changes on the other hand are significant, with several hundreds of meters being cooled down to the injection temperature of 20 degrees. The radius of the cooled volume increases from 300 m after 5 years of injection to over 800 m after 50 years. The temperature front also becomes increasingly asymmetric with injection time, with a preferential direction to the production well. Vertically, the largest temperature decrease occurs within the reservoir interval, though also part of the seal and base formations cool down. After ~30 years cooling starts to affect the fault, amounting to 10 degrees of cooling after 50 years of operations (Figure 5-5). The pressure changes at the fault are negligible.

The stress response on the fault is dominated by the evolution of the cooling front. Initially no stress changes are observed (Figure 5-6). As the cooling front approaches the fault after 30 years the normal stress decreases on the fault within and above the reservoir (Figure 5-6c), and the shear stress increases on the fault segments within and above the reservoir; the net effect is an increase in Coulomb stress change on the fault in and around the reservoir formation. Hence, the fault becomes more unstable, but note that the magnitude of the stress changes is still relatively small. The fault stress changes increase significantly when the cooling front has passed the fault and parts of the reservoir around the fault have cooled down, with a decrease in normal stress and an increase in shear stress, as was also observed in the previous Chapters. A circular area of high Coulomb stress

develops on the fault at the reservoir depth interval (Figure 5-6l). Even though after 50 years only 10 degrees of cooling is observed at the fault location the maximum magnitude of the Coulomb stress change is already 2 MPa. Larger stress changes will occur when the fault is located closer to the injection well – such a scenario is evaluated in the next section.

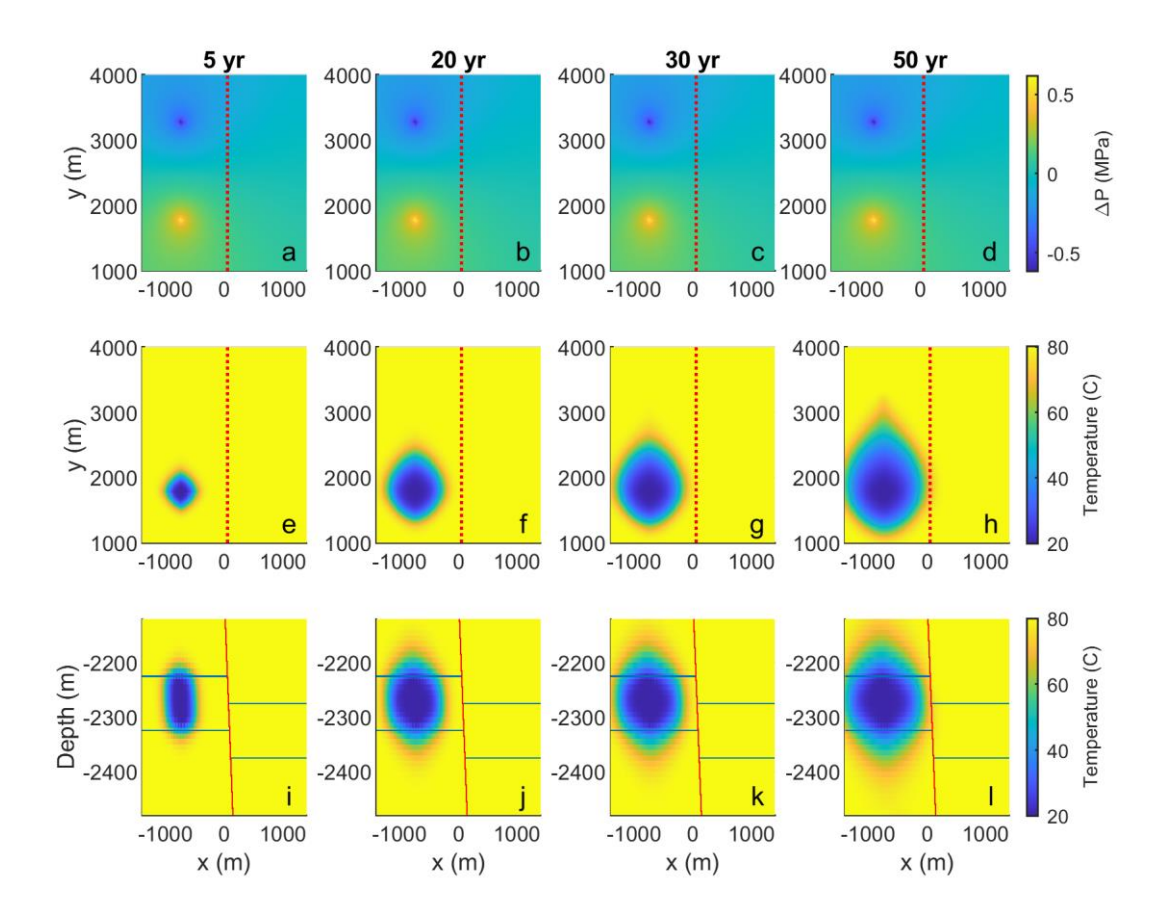


Figure 5-4 Pressure and temperature with injection time for a fault-parallel doublet 750 m from the fault. Pressure at a reservoir depth of -2300 m (z_{mid}). The position of the fault at reservoir depth is indicated with the red dotted line. a-d) pressure change at a reservoir depth of -2300 m (z_{mid}), e-h) temperature at a reservoir depth of -2300 m, I-I) temperature in vertical cross-section at y = 1750 m. Footwall and hanging wall depths are indicated by the horizontal lines. Note the exaggeration of the vertical scale in the final four plots.

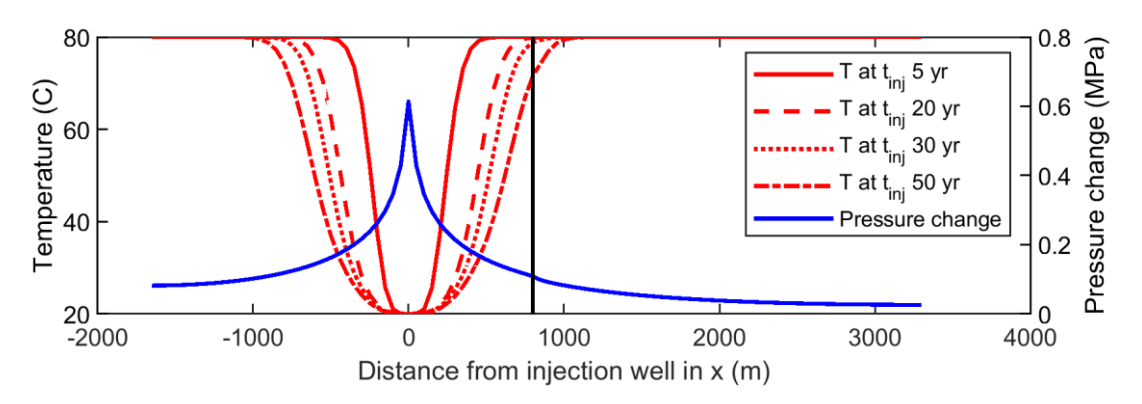


Figure 5-5 Temperature evolution and pressure change at -2300 m with distance from the injection well. The position of the fault at reservoir depth is indicated with the black line.

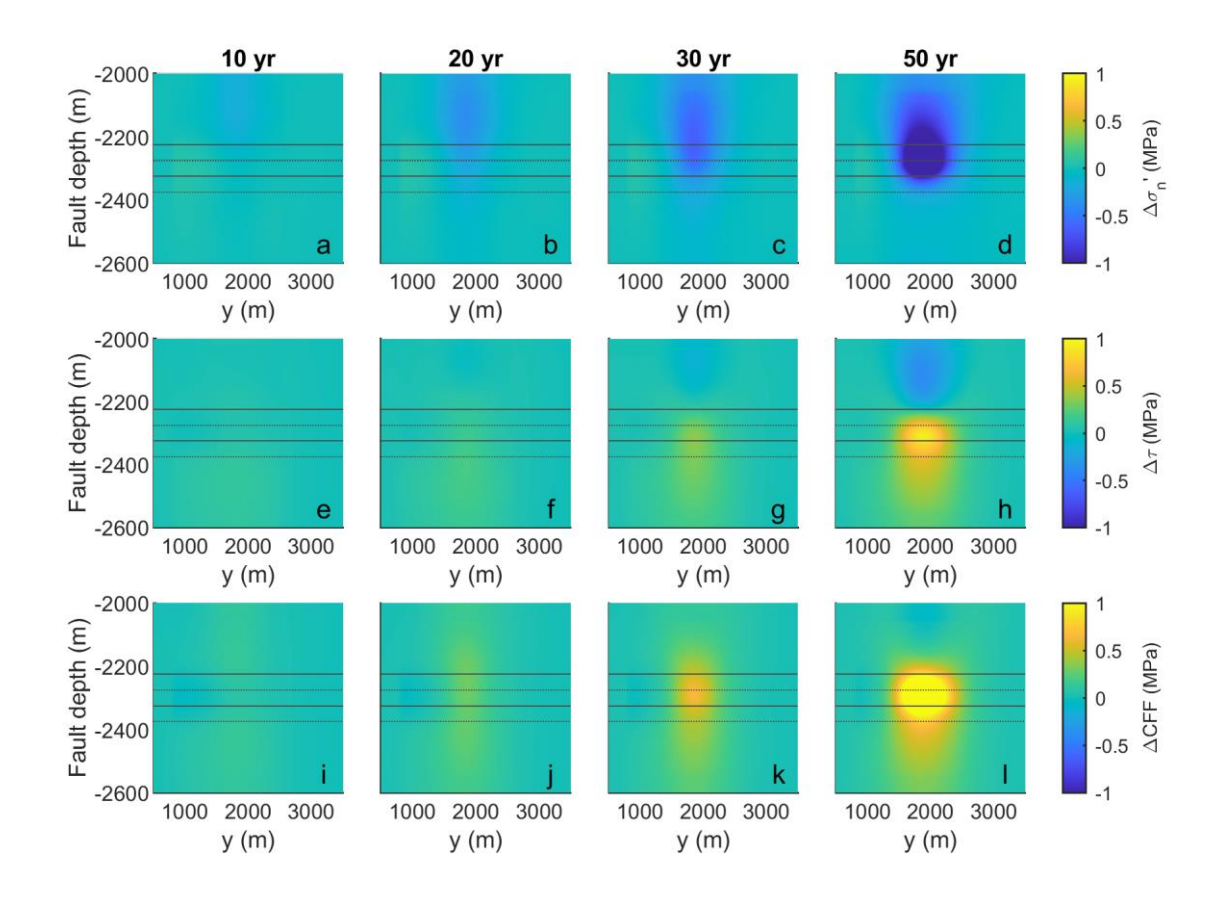


Figure 5-6 Fault stress with injection time for a doublet oriented parallel to the fault at 750 m distance in the footwall. The position of the footwall and hanging wall depths are indicated with the solid and dotted line. a-d) normal stress change, e-h) shear stress change, e-h0 Coulomb Stress change. The cooling front reaches the fault after ~30 years.

5.4.2 Doublet parallel to fault – injection well at 100 m

In the second scenario the injection well is located close to the fault. The pressure and temperature evolution in the horizontal plane are similar as those for the doublet far away from the fault. Due to the proximity of the doublet to the fault the cooling front reaches the fault in the first years of the injection, and eventually several hundreds of m along the fault's strike are affected by the cooling front. In the vertical cross-sections the offset of the cooled volume following the offset of the reservoir formation can be clearly seen.

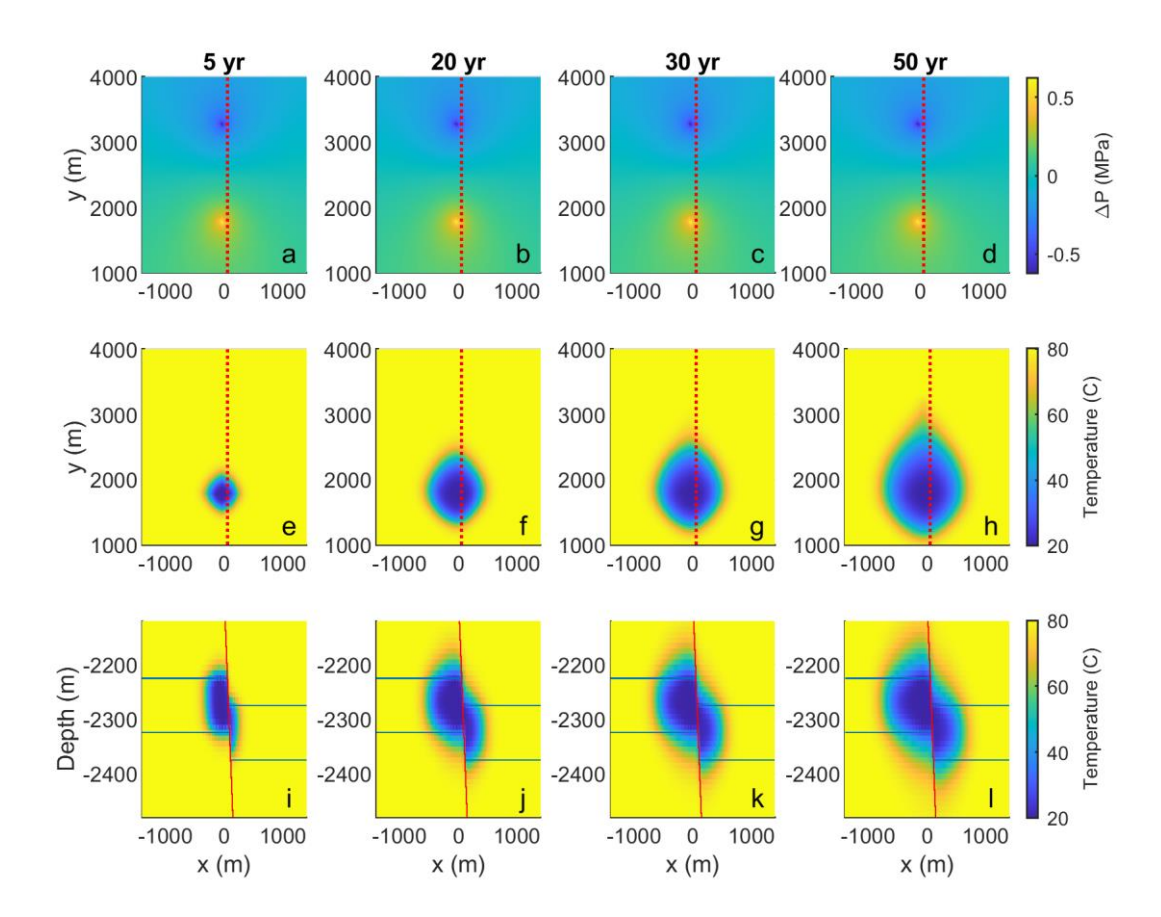


Figure 5-7 Pressure and temperature with injection time for a doublet parallel to the fault at 100 m from the fault. Pressure at a reservoir depth of -2300 m (z_{mid}). The position of the fault at reservoir depth is indicated with the red dotted line. a-d) pressure change at a reservoir depth of -2300 m (z_{mid}), e-h) temperature at a reservoir depth of -2300 m, I-I) temperature in vertical cross-section at y=1775 m (i.e. the well y-coordinate). Footwall and hanging wall depths are indicated by the horizontal lines. Note the exaggeration of the vertical scale in the final four plots.

The cooling of the rock volume around the fault results in significant stress changes on the fault, with a decrease in effective normal stress and an increase in shear stress (promoting normal faulting). The net effect is an increase in the Coulomb stress (CFF) of over 10 MPa. On parts of the fault CFF > 0 indicating reactivation occurred. Note however that in the current example fault slip was not modeled. The maximum of the stress changes coincides with the center depth of the reservoir z_{mid} , at -2300 m. Stress changes decrease gradually up- or down-dip along the fault, decaying to the insitu stresses at ~100 m below or above the base or top of the reservoir (e.g. Figure 4-5, Chapter 4). The stressed area along the strike of the fault is elliptical with a maximum axis of ~1000 m.

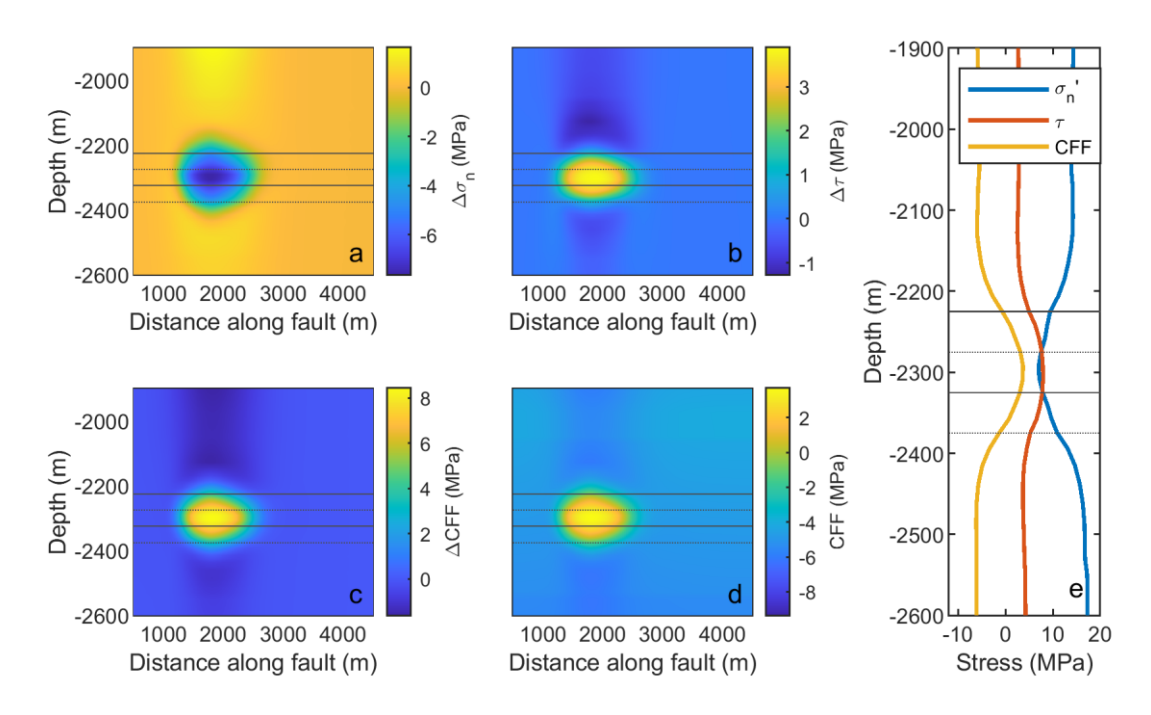


Figure 5-8 Stress changes on the fault after 30 years of injection, for a doublet oriented parallel to the fault at a distance of 100 m. a) Normal stress change, b) Shear stress change, c) Coulomb stress change (Δ CFF), d) Total Coulomb stress (CFF), e) stress changes on the fault at the location closest to the injection well (1900 m). Note the exaggeration in the vertical direction in a-d. Horizontal lines indicate the top and bottom boundaries of the reservoir footwall (solid lines) and hanging wall (dotted lines).

5.4.3 Effect of doublet orientation with respect to fault orientation

The temperature distribution around the injection well is asymmetric, in particular after several decades of operations, as mentioned in Section 5.4.1 and as can be seen in Figure 5-4. The cooled volume grows preferentially towards the production well. Since cooling dominates the stress changes experienced by the fault, the orientation of the doublet with respect to the fault orientation can influence the stress changes. In Figure 5-9 the growth of the cooled volume with operation time is shown for a doublet parallel and perpendicular to the fault. Although in both cases the injection well is located at the same distance to the fault (750 m), the fault area affected by cooling is much larger in case of a doublet perpendicular to the fault, because of the aforementioned asymmetric growth of the cooled volume. This is reflected by the Coulomb stress changes on the fault. After 30 years only small stress changes (<0.8 MPa) occur on the fault for the fault-parallel doublet, whereas a >2 MPa Coulomb stress increase occurs on the fault for the fault-perpendicular doublet (Figure 5-10). Doublet orientation with respect to the predominant fault orientation in an area can thus affect the reactivation potential, with doublets perpendicular to the fault orientation generating the largest Coulomb stress change. Note that in the current study it is assumed the fault is open; if faults are sealing stress changes are expected to be different from those presented here, see e.g. van Wees et al., 2020.

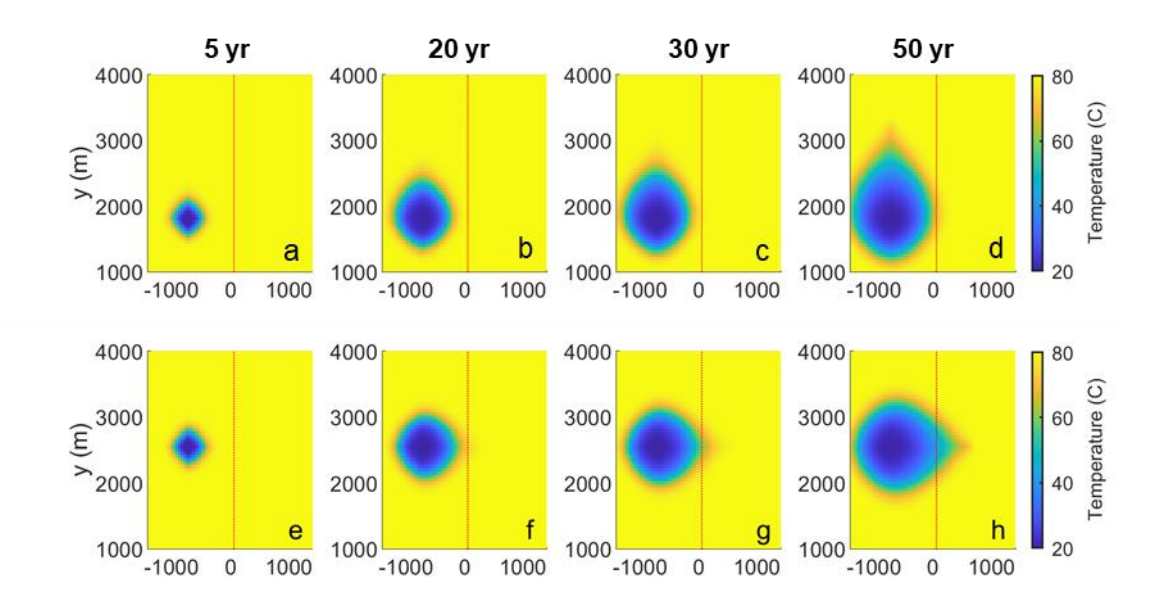


Figure 5-9 Effect of doublet orientation on evolution of temperature field. Temperature distribution is shown in map view, at a depth of -2300 m. In both cases the injection well is located 750 m from the fault (red dotted line). a-d) doublet parallel to fault orientation, e-h) doublet perpendicular to fault orientation.

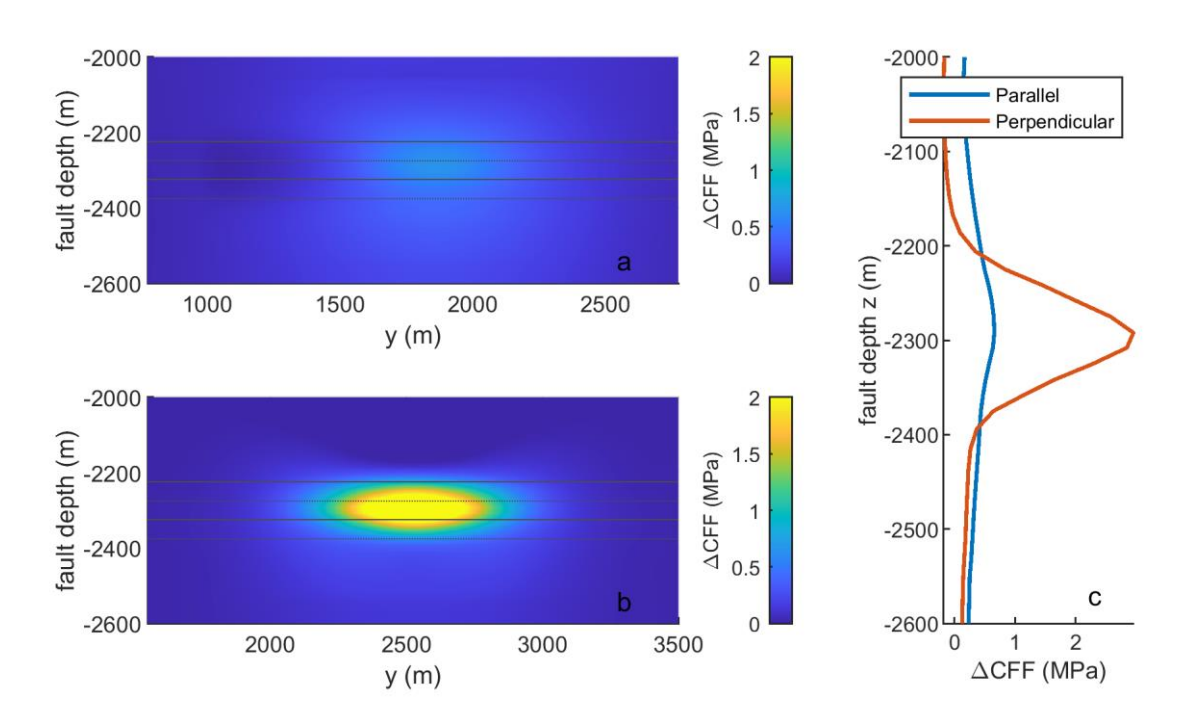
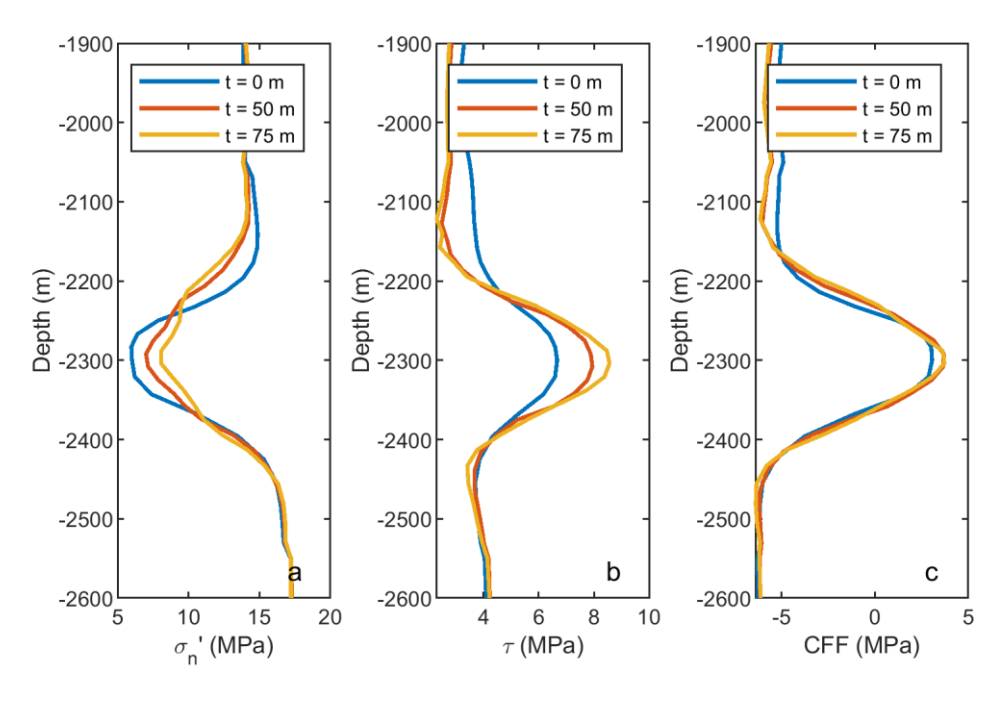


Figure 5-10 Effect of doublet orientation on fault stress. In both cases the injection well is located 750 m from the fault. a) Coulomb stress change after 30 years for a doublet parallel to fault orientation, b) Coulomb stress change after 30 years for a doublet perpendicular to fault orientation, c) Coulomb stress change along fault for fault-parallel doublet (at y = 1850 m) and a fault-perpendicular doublet (at y = 2525 m).

5.4.4 Effect of reservoir offset on stress changes

Previous studies showed that for depletion fault offset plays an important role as the offset reservoir configurations concentrates the shear stresses on the fault and hence promotes reactivation (e.g. Buijze, van den Bogert et al., 2019; Mulders, 2003; Orlic & Wassing, 2013; Roest & Kuilman, 1994). This was also apparent in the results generated by PANTHER2D, e.g. Figure 4-5b, where clearly the offset focuses the shear stresses and CFF along the reservoir-reservoir juxtaposition. For cooling

the effect was less pronounced, though still present. However, in PANTHER2D a relatively simple temperature function was imposed, whereas the temperature function used in DIANA3D is generated by reservoir simulator OPM. In +Figure 5-11 the effect of reservoir offset on fault stresses is shown for OPM-DIANA. Similar to previous modeling studies, reservoir offset concentrates the shear stress in the reservoir interval, whereas the normal stress changes is less than for a 0 m offset case. The resultant CFF is slightly larger for the offset scenarios compared to the 0 m offset scenario, though not by much. Note that differences may be larger for other fault dips. The elevated shear stress and CFF found at the reservoir top and bottom in PANTHER2D (Figure 4-5f, h) are however absent in the OPM-DIANA results. This may be due to differences in the temperature distribution around the fault and/or the larger element size used in OPM-DIANA which tends to smoothen stress concentrations.



+Figure 5-11 Effect of reservoir offset on fault stress changes, for a fault-parallel doublet at 100 m from the fault. A) effective normal stress, b) shear stress, and c) Coulomb failure stress.

5.4.5 Stiffer seal and base formation

In the previous sections all formations had the same elastic material properties. However, significant variations in stiffness are expected between formations in the subsurface, with for example weaker clay and unconsolidated sand formations and stiffer anhydrite and carbonate formations. These stiffness contrasts can affect the stress changes that develop on faults during operations, in particular since the seal and base formation also experience cooling through thermal diffusion, see e.g. Figure 5-4. In Figure 5-12 the fault stresses of the default scenario with the doublet close to the well are compared to the same scenario where the seal and base formation were assigned a higher Young's modulus of 30 GPa, twice that of the reservoir. The higher stiffness of the seal and base results in a larger decrease of normal stress and larger increase of shear stress on the fault in the seal-reservoir and reservoir-base juxtapositions, as well as directly above and below the seal and base (Figure 5-12b). The net effect is a larger Coulomb Stress over a larger part of the fault compared to the uniform elasticity case (Figure 5-12c). In the center of the reservoir (z = -2300 m) Coulomb stresses were the same, but in the upper and lower parts of the reservoir interval Coulomb stress changes for the stiffer seal and base are several MPa larger than for the default scenario. A stiffer seal and base can thus lead to an increased potential for fault reactivation. Note that at the boundaries between

formations the stresses may be more concentrated than shown here as the element size of 10 m will smooth these concentrations.

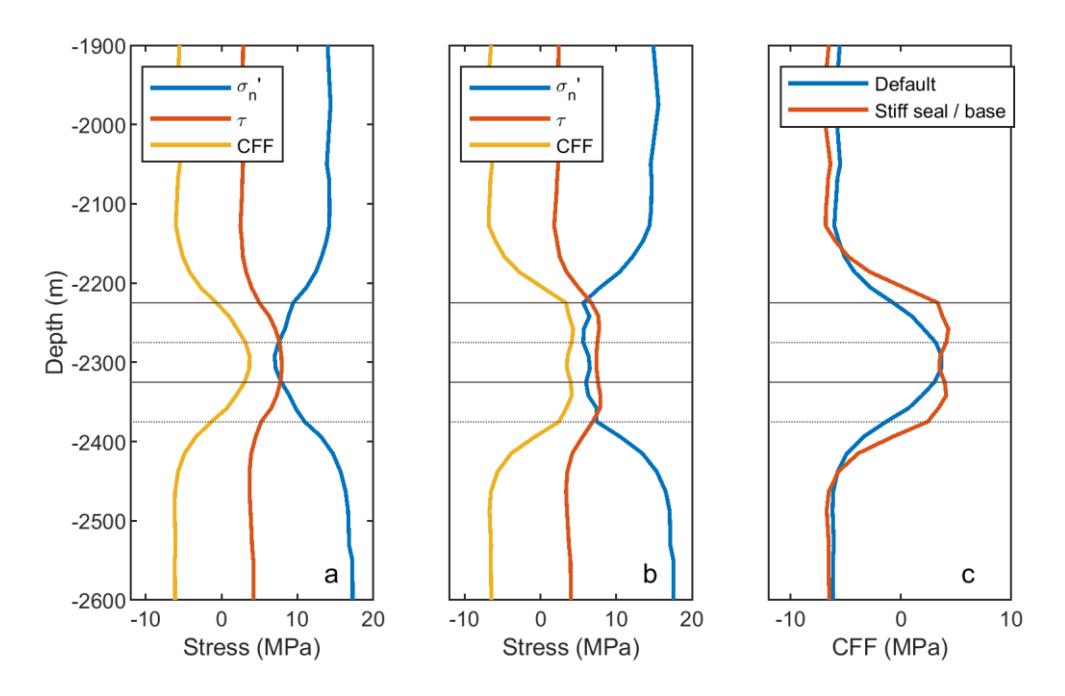


Figure 5-12 Effect of stiffness contrast between reservoir and seal and base formations on fault stress. Fault stresses are shown for the scenario where the doublet is located in the footwall and is oriented parallel to the fault at 100 m from the fault, after 50 years of operations. Solid lines indicate footwall depth, dotted lines the hanging wall depth. a) Default scenario with uniform elasticity. b) Heterogeneous elasticity, where the seal and base formation have a Young's modulus of 30 GPa (2 x that of the reservoir formation). c) Coulomb Stress for both the default and the stiff seal/base scenario's.

5.5 Discussion & Conclusion

The OPM-DIANA workflow presented in this chapter provides the pressure-temperature history and the stress changes in and around a doublet operating in a faulted reservoir, in full 3D. The results presented in this chapter show that fault stress changes are largest within the cooled volume, and depend strongly on the proximity of the injection well to the fault, as well as the doublet orientation with respect to the fault, fault offset, and stiffness contrasts. The results are in agreement with an earlier study by van Wees et al. (2020), who presented a similar 3D workflow using OPM for the pressure temperature fields, but MACRIS (Mechanical Analysis of Complex Reservoir for Induced Seismicity) for the computation of the stress changes. The geometry used in van Wees et al. (2020) is the same as the faulted block geometry used in the current study. The Coulomb stress changes on the fault are the same as in the current study with a maximum at the reservoir-reservoir juxtaposition, decreasing gradually in the up- and down-dip direction. Van Wees et al. (2020) furthermore show that stress changes are smaller when flow is prevented across the fault due to e.g. a fault throw larger than the reservoir thickness, because cooling occurs on one side of the fault only. It is interesting to consider the effect of fault permeability on the evolution of the cooling front and hence the fault stresses. Sealing faults may lead to smaller stress changes, but it will also be interesting to compare the area over which the stress changes occur. If the cooled volume grows preferentially on one side of the fault in the direction along the fault strike, the magnitude of stress change may be smaller but the area larger, which could promote larger slip events. Also, if a damage zone is present along the fault this could lead to a larger cooled volume in the strike direction of the fault. We recommend to address the effect of fault permeability and the role of a damage zone on the cooling front and stress change in future modeling studies.

The OPM-DIANA workflow is slower than the OPM-MACRIS workflow, mainly due to differences in the mapping algorithms of the PT-field to the MACRIS vs the DIANA model space, and also because of the effective mesh-free approach used in MACRIS. DIANA FEA on the other hand allows for variations in stiffness and nonlinear material behavior, which is not incorporated in MACRIS. Indeed, in Section 5.4.4 we show that a stiffer seal and base can promote fault reactivation as the stressing rate in these formations is higher than in the reservoir. This is because part of the seal and base experience cooling, and the stress changes are related to the higher Young's modulus of those formations. In case stiff overburden formations are expected, this effect is important to take into account.

Many previous studies have focused on depletion-induced stress changes and fault reactivation. In these studies the fault throw is shown to have a large effect on fault stress and reactivation, as also shown in Chapter 4. Note however that the effect of fault throw is much smaller for the geothermal-induced stress changes presented in this chapter. This is because the geometry of the PT-field is driving stress changes. For depletion relatively sharp contrasts in pressure likely exist between the porous, permeable reservoir formation and the impermeable seal. The sharp pressure contrasts, in combination with offset of the reservoir compartments, result in stress concentrations at the reservoir top and bottom (see e.g. Jansen et al., 2019). For geothermal doublets the pressure increase may similarly be limited to the reservoir formation if the seal and base are impermeable, but the pressure increase is relatively small and stress changes are driven by cooling. Even for an impermeable seal and base formation, thermal conduction will cause cooling of the seal and base, resulting in a relatively smooth transition of temperature changes between the reservoir and the seal and base. For these smooth temperature profiles no stress concentrations develop even though the reservoir formations are offset by the fault, see also for further discussion 6.1.2.

The main conclusions are listed here:

- Stress changes are almost solely determined by cooling; the pressure changes around the injection and production well remain limited.
- Circa 50 100 m of the seal and base formation are also cooled.
- The cooling front becomes increasingly asymmetric with increasing operation time, growing preferentially in the direction of the production well.
- The extent of the cooling front matches relatively well with SRIMA and the cooling front predicted by the heat balance equation. The largest differences occur because of the asymmetry mentioned above. For fault reactivation this plays a role when the doublet is oriented perpendicular to the fault orientation.
- Cooling of parts of the fault results in a decrease in effective normal stress and increase in shear stress, with the net effect a positive Coulomb stress change (destabilizing)
- When the cooling front has reached the fault an elliptical (doublet fault-parallel) area of higher Coulomb stress develops.
- The cooling-induced Coulomb stress reaches its maximum at depths where reservoir is juxtaposed against reservoir, and decreases gradually towards the seal and the base. No stress concentrations developed near the reservoir top and bottom even though the reservoir is offset by the fault. This is because thermal diffusion which yields a smooth temperature distribution in and above and below the reservoir. Fault offset does however enhance the Coulomb stress changes along the reservoir interval.
- For stiffer seal and base the Coulomb stress changes in the seal and base exceed those of the reservoir. Stiffer seal and base hence promote reactivation and lead to a larger depth interval that is affected by the stress changes i.e. the full reservoir interval from top of the footwall to the base of the hanging wall, as well as parts of the seal and base, whereas for uniform elasticity mainly the reservoir-reservoir juxtaposition is stressed. The larger the offset on the fault, the larger the difference between the heterogeneous and homogeneous elasticity scenarios.

6 Integration and discussion

6.1 Comparison of the different modeling tools

In this report three novel, different geomechanical modeling tools were presented that address fault reactivation (and seismic rupture) in and around a geothermal doublet circulating fluid through a porous reservoir formation. Each of these tools has its own merits and limitations, and each can be used for different purposes. In this section we summarize the advantages and limitations of the three tools: SRIMA, PANTHER2D, and OPM-DIANA. We then go on to compare the PT-fields used in these tools, and the resulting stress changes, and give recommendations on the use and future improvements of the three tools.

6.1.1 Summary of model setup and advantages and limitations

SRIMA allows to map the reactivation risk associated to different injection and subsurface scenarios for a simplified scenario of constant injection into a single vertical well in a reservoir with homogeneous flow and temperature properties. Temperature and pressures are modeled assuming lateral convective flow, and vertical conduction to the seal and base. The assumption of radialsymmetry implies SRIMA cannot capture the asymmetry of the cooling front when it preferentially grows to the production well with increasing injection time. To a first order, however, SRIMA captures the temperature field and the fault stress changes well, and can be used as a screening tool for geothermal doublets to assess the extent of the cooled volume (r_{cooled}), the extent of the volume where fault reactivation can occur (r_{crit}), and the reactivation potential on faults. Results can be used when designing geothermal doublet operations in a reservoir with mapped faults. The use of SRIMA should be limited to reservoirs where convective heat transfer is dominant in the reservoir, where fault offset remains limited (less than the reservoir height), and faults are fully open. Care should be taken when using SRIMA for large stiffness contrasts in the seal and base, in particular when the ratio of elastic Young's modulus of seal and aquifer is smaller than a factor 0.5. The benchmark against an axisymmetric reservoir in DIANA FEA using the same PT-field shows that just outside the cooled front the fault stress changes in the reservoir may not be conservative. The assumption of a simplified radial-symmetrical geometry implies also limitations for use in case of strongly deviated wells and in case geothermal doublet operations occur in heterogeneous reservoirs with high-permeability streaks or when permeable fault systems are present.

PANTHER2D focuses on the effects of fault geometry and fault weakening on reactivation and rupture. A uniform pressure or temperature field is prescribed within the reservoir, whilst for cooling also thermal conduction to the seal and base is incorporated. The resulting poro- and or thermoelastic stress changes are computed on and around a fault that offsets the reservoir. Fault reactivation is modeled, as well as the along-dip rupture length. PANTHER2D incorporates fault weakening behavior which is a fundamental aspect of seismic instability on faults. This means we can use PANTHER2D for first order assessment of the potential for rupture growth outside of the reservoir, which is directly relevant for seismic event magnitude. The assumption of uniform cooling in the reservoir and equal cooling of reservoir blocks on both sides of the fault (simulating e.g. an undetected fault near the injection well) yields conservative stress change estimates for cooling with respect to the more realistic case where cooling occurs over an elliptical volume. Moreover, being 2D plane-strain, it lacks the third dimension; for assessment of seismic magnitudes we need to make assumptions on width of the seismic rupture area. PANTHER2D cannot account for large stiffness contrasts between in the seal and base and reservoir. We used PANTHER2D to analyze driving mechanisms and characteristics of reactivation and rupture for both a depleting and for a cooling reservoir, comparing rupture lengths and seismic event magnitudes.

OPM-DIANA can be used to model fault reactivation in 3D, taking into account the asymmetrical spatio-temporal evolution of the cooling front between the injection and production well, realistic fault and reservoir geometries and heterogeneities, such as stiffness contrasts between reservoir, base and seal. In contrast to the other tools, it can be used to assess the effects of doublet configuration on fault reactivation potential (e.g. doublet orientation with respect to the fault and distance between injection and production well). As modelling in OPM-DIANA is computer-intensive, fully stochastic analysis with 10,000s simulations is not feasible on a regular desktop PC. We consider OPM-DIANA a valuable tool for the understanding of stressing mechanisms around doublets and assessment of fault reactivation potential, when geometry, flow and mechanical parameters are more constrained based on location-specific data and results are validated against monitoring data. The 3D model workflow using OPM-DIANA is for example computer-intensive compared to the two fast models introduced in Chapters 3 and 4, SRIMA and PANTHER2D. In total, the 3D workflow requires several hours, with the interpolation step being the most time consuming followed by the flow simulation. In contrast, a single model realization in SRIMA and PANTHER2D takes several milliseconds, which makes these two models more suitable for quick screening and stochastic analyses. However, both these two faster models use several simplifying assumptions with respect to the 3D model workflow.

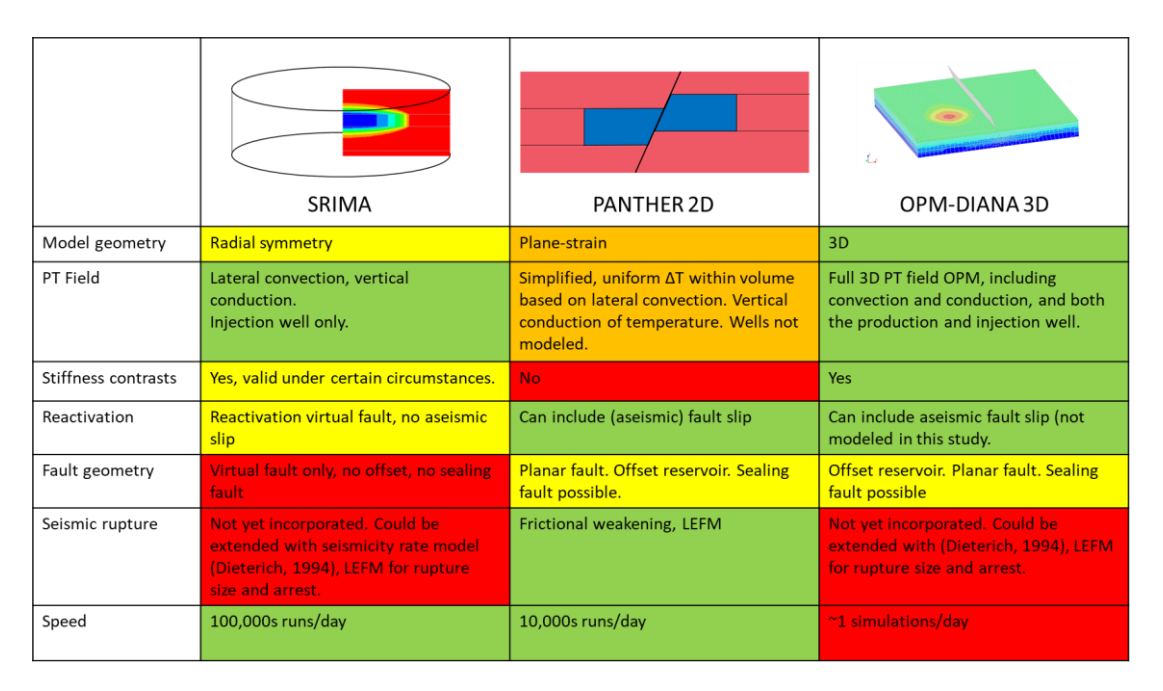


Figure 6-1 Overview of the three model approaches presented in this report and different assumptions used. Speed is related to the runtime on a powerful PC, not on a cluster or supercomputer.

6.1.2 Temperature distributions used in OPM-DIANA3D, SRIMA and PANTHER2D

First of all, the shape and extent of the cooled area are compared. For SRIMA, radial symmetry is assumed around the injection well and no production well is thus included. For PANTHER2D, uniform cooling is assumed within the reservoir, with the width of the cooled zone based on the convective heat balance equation (Equation 4-2). In Figure 6-2 and Figure 6-3 the temperatures computed in OPM Flow and SRIMA, as well as the cooled radius computed from the heat balance equation, are compared. Overall the agreement between OPM Flow and SRIMA is good. The cooling front computed by OPM Flow is however less abrupt then that of SRIMA, and extends slightly beyond that of SRIMA. This is likely due to horizontal conduction of heat not being taken into account in SRIMA (see e.g. Saeid & Barends, 2009), or numerical diffusion of temperature as was stated in Section A6,

where the pressures and temperatures computed in SRIMA were compared to those of reservoir simulator Eclipse.

With progressive injection time the cooling front modeled in OPM Flow becomes increasingly asymmetric with the cooled volume growing preferentially towards the production well, an effect that is not captured by SRIMA. The OPM Flow results show that in the direction of the production well cooling of several tens of degrees may occur over several hundreds of meters beyond the cooled radius computed for a scenario just considering the injection well such as in SRIMA, or the radius from the heat balance equation (Figure 6-2c, d, Figure 6-3c, d). The center of the cooled volume also does not coincide with the injection well but is shifted slightly towards the production well (Figure 6-2).

Apart from the doublet-parallel direction, the heat balance captures the extent of the cooled area reasonably well. The extent of the cooled volume computed in SRIMA in fact coincides with that computed using the heat balance equation, which is also based on lateral convective heat transfer. However, the temperature distribution inside the cooled volume differs significantly, with a uniform temperature decrease employed for the heat balance equation but an elliptical temperature distribution in SRIMA. The difference is due to conductive heat transfer to the seal and base formations which is accounted for in OPM Flow and SRIMA, but is not for the current convective heat balance equation. Hence, the uniform temperature change within the cooled radius computed using the heat balance equation will overestimate the temperature decrease within the reservoir in particular near the edges of the cooled front, because it does not include cooling of the seal and base.

Note that the temperature distribution shown for SRIMA in Figure 6-3 is not used one-to-one for the computation of thermo-elastic stresses. Rather, the temperature distribution shown in Figure 6-3 is parametrized by a number of uniformly cooled cylinders to allow for the use of the Myklestad thermo-elastic solutions, superimposed with uniaxial stress changes for the cooled parts of the seal and base (see Appendix A). This leads to small, acceptable difference in (vertical) stress changes near the edges of the cooled volume.

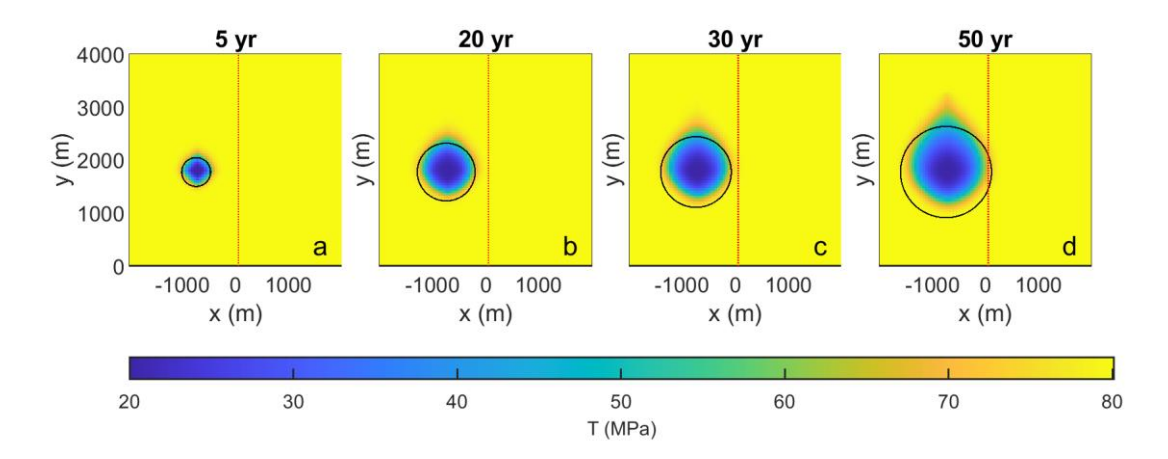


Figure 6-2 Comparison of temperature distribution computed in OPM Flow against cooled cylinder computed based on the heat balance equation (Equation 4-2). Results are shown at $-2300 (z_{mid})$ for a doublet oriented parallel to the fault, located 750 m from the fault.

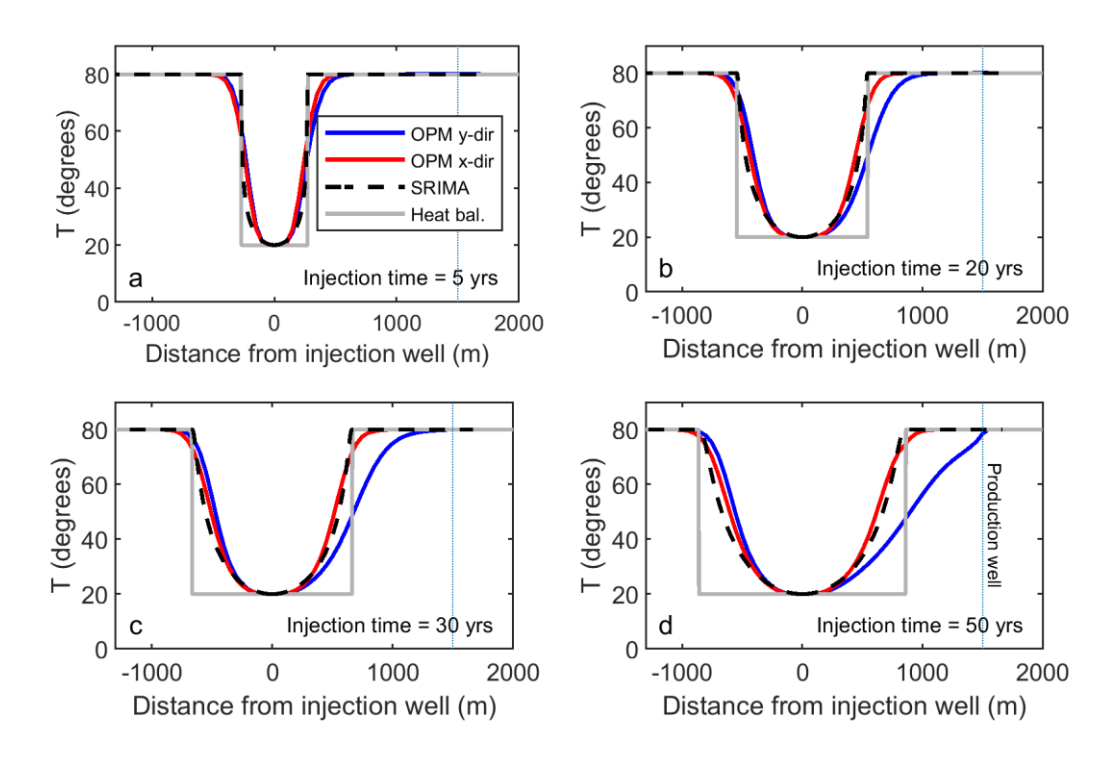


Figure 6-3 Comparison of modeled reservoir temperature with distance from the injection well for OPM Flow and SRIMA. Temperatures are taken at the center of the reservoir at -2300 m. For OPM Flow the temperature is shown in the direction towards the production well (y-dir), as well as perpendicular to the doublet orientation (x-dir). In addition to the model results also the cooled radius of the heat balance equation is shown.

6.1.3 Stress changes in the reservoir and comparison to uniaxial stress change

Using the same pressure and temperature field, in this case the axisymmetric pressure and temperature changes computed using SRIMA, the poro-thermo-elastic stress changes computed in SRIMA and an axisymmetric DIANA model can be compared (see also Appendix A.7). The total horizontal stress change is very similar (Figure 6-4b), but the total vertical stress change is different (Figure 6-4c). Overall the vertical stress decrease in the cooled area is underestimated in the SRIMA calculations. Also the discretization of the temperature field shows up as sudden jumps in the vertical stress changes. However, because the vertical stress change is only 25% of the horizontal stress change, the resulting Coulomb Stress changes are quite similar.

It is also insightful to compare the stress changes computed in SRIMA and DIANA to a first order estimate assuming uniaxial strain for each location in the reservoir. Under this assumption, stress changes could be computed directly from the pressure and temperature field, ignoring stress transfer (stress arching). For a give pressure and temperature change, uniaxial strain conditions (i.e. laterally extensive reservoir) imply the total vertical stress change is zero, and the total horizontal stress change due a pressure and temperature change is given by

$$\Delta \sigma_h = \frac{E\eta \Delta T}{(1-\nu)} - \frac{\Delta P(1-2\nu)}{(1-\nu)}$$
 6-1

where E is Young's modulus, η is the linear thermal expansion coefficient, and v is Poisson's ratio. The $\Delta\sigma_h$ and $\Delta\sigma_v$ computed directly from the pressure and temperature distribution of SRIMA are plotted in Figure 6-4 (blue dash-dotted lines). Within the cooled reservoir volume the horizontal stress change under the uniaxial assumption matches well with the stress computed in SRIMA. Close to the edge of the cooled volume, around 550 m from the well, the uniaxial approximation underestimates the horizontal stress decrease, as stress arching effects are not included. Also the vertical stress change is different; under uniaxial conditions the vertical stress change is zero whereas

for the current scenario the total vertical stress does change. Because this is not taken into account for the uniaxial approximation, the resulting Coulomb Stress change is underestimated. The smaller the width of the cooled volume the larger the vertical stress change will be (see e.g. Soltanzadeh & Hawkes, 2009) and the larger the difference between the uniaxial approximation and SRIMA and DIANA. Computing stress changes directly from the pressure and temperature field provided by SRIMA or e.g. another reservoir simulator could give a good first order estimate of the stress response, but will underestimate the Coulomb stress (and reactivation potential) just outside the cooled area and also within the cooled area when the aspect ratio of the cooled volume (height/width) decreases. Discrepancies are also expected near faults offsetting the reservoir compartments and for elasticity contrasts. In such cases DIANA3D FE modeling or PANTHER2D could be used.

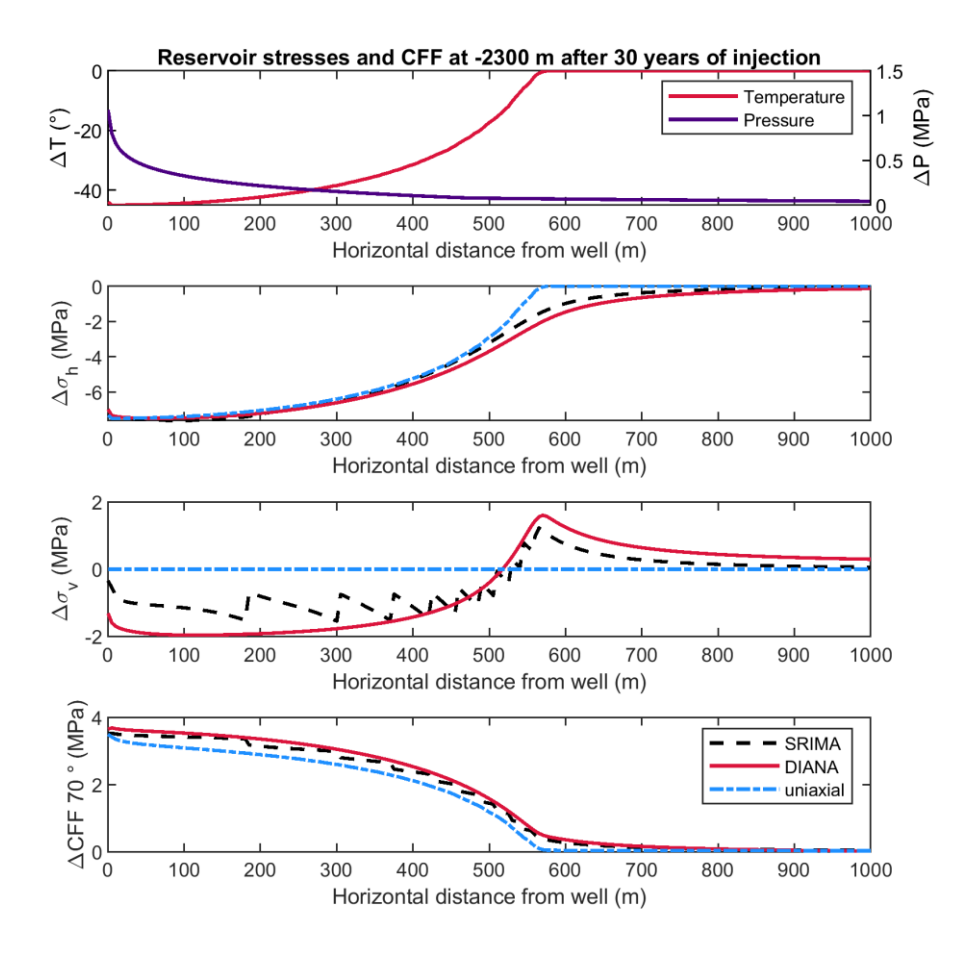


Figure 6-4 Comparison of stress changes for an axisymmetric model. a) Axisymmetric pressure and temperature field computed using SRIMA, b, c, and d) respectively the total horizontal, vertical, and Coulomb stress change computed using SRIMA, DIANA and assuming uniaxial stress change at each location experiencing a pressure and/or temperature change (ignoring stress arching effects). Pressures, temperatures, and stresses are computed at -2300 m depth (the reservoir center) and plotted against distance from the injection well.

6.1.4 Fault stress changes on offset faults

The difference in the three temperature functions discussed in the previous section can result in different thermo-elastic stress changes. In addition, OPM Flow and PANTHER2D include a realistic fault geometry where the reservoir is offset, whereas SRIMA does not. From gas production related

studies it is know that fault offset can cause stress concentrations and promote fault reactivation. Not including fault offset could thus lead to an underestimate of fault stress changes; hence it is important to evaluate the effect of offset on fault stress changes for the geothermal doublet scenario, in combination with the effects of the assumed temperature distribution on the fault stress changes and other differences such as the assumed model geometry.

In Figure 6-5 the fault stresses computed using the DIANA 3D model, SRIMA (axisymmetric), and PANTHER2D (plane-strain) are compared, on a fault with 50 m offset at 100 m from the injection well. Along the reservoir-reservoir juxtaposition (-2275 to -2325 m), the normal stress change computed using SRIMA is overestimated and the shear stress increase underestimated. For the current dip and offset the resulting CFF is however similar, though the increase in CFF occurs over a larger part of the fault compared to the 3D model, because fault offset is not taken into account. This agreement between the CFF computed in SRIMA and DIANA3D may be coincidental; in DIANA3D the CFF is peaked because of reservoir offset (+Figure 5-11c), whereas in SRIMA the CFF on steeply dipping faults in the cooled reservoir volume tends to be overestimated by ~15% due to the model assumptions (Appendix A.8).

The normal stress decrease modeled in PANTHER2D in the reservoir-reservoir interval matches well with DIANA 3D, but the shear stress increase is significantly larger than that of the other two models. The net result is an overestimate of the Coulomb Stress in the reservoir center. The reason for this is two-fold: the use of the uniform temperature decrease in the reservoir in combination with the offset reservoir in PANTHER2D, and the plane-strain assumptions in PANTHER2D. Uniform cooling of the reservoir results in shear stress increases being concentrated to reservoir-reservoir juxtaposition (see also 4.4.2). In SRIMA there is no offset and in OPM-DIANA the temperature profile is more gradual compared to PANTHER2D, which leads to lower shear stress changes. PANTHER2D does agree with a comparable DIANA2D plane-strain model, although stress concentrations in the reservoir are a bit more pronounced in PANTHER2D.

PANTHER2D and DIANA2D are plane-strain model. This is applicable to depleting reservoirs but cooling occurs in a cylindrical or elliptical volume around the injection well. This can lead to different stress responses. In Soltanzadeh & Hawkes (2009) stress arching ratios are compared for a planestrain and an axisymmetric inclusion. The differences between plane-strain case (ellipsoidal cylinder) and axisymmetric case (oblate spheroid) are 13% (horizontal stress change) and 17% (vertical stress change) at most for aspect ratios of 1 (for the default Poisson ratio of 0.2 and Biot of 1), decreasing to zero difference for infinite width reservoirs. Over 80% of simulations in Chapter 4 have an aspect ratio of 0.3 or less, for which the difference between plane-strain and axisymmetric Coulomb Stress Changes is <5%. Only in the case of very thick reservoirs and relatively small flow rates, or early in the injection period, will the plane-strain assumption deviate significantly from the axisymmetric cooling front. Hence ~5% of the difference between PANTHER2D and DIANA3D could be attributed to the plane-strain assumption, and the remainder of the difference is likely the result of the different temperature function. Another reason for the differences between PANTHER2D and OPM-DIANA could be the relatively large element size used in OPM-DIANA (10 m, compared to 1 m) which tends to smoothen stress concentrations. PANTHER2D (and DIAN2D) will thus tend to be conservative with respect to the other two models in that it underestimates the amount of cooling required for reactivation. Hence it is important keep in mind that the plane-strain models tend to be conservative for the current normal faulting configuration.

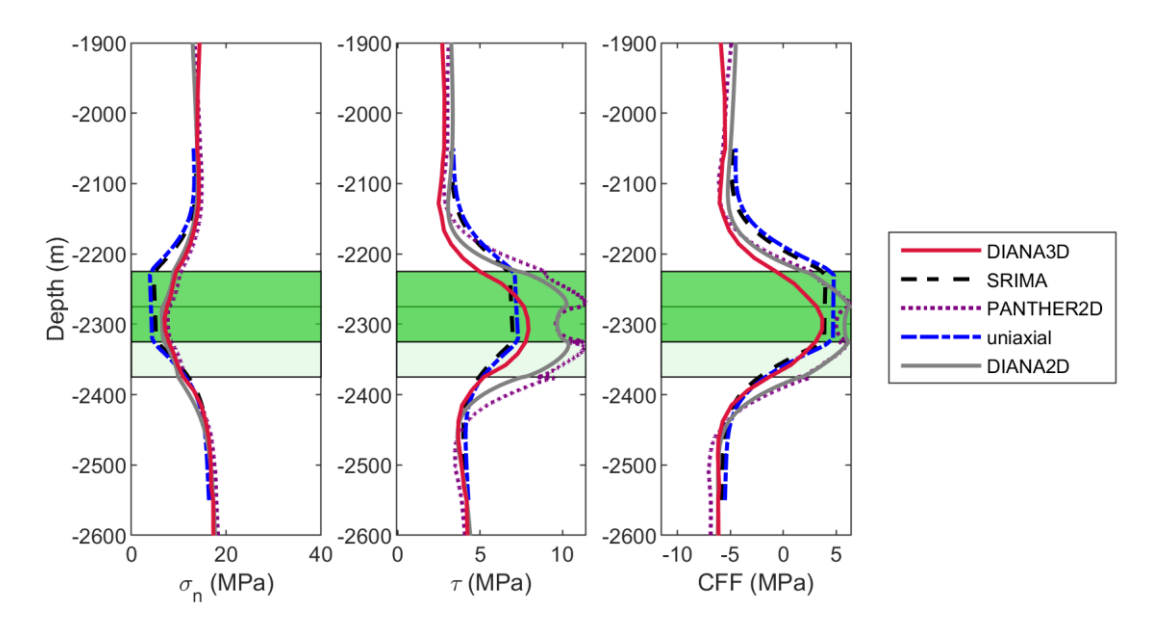


Figure 6-5 Comparison of fault stresses computed in DIANA3D-OPM, SRIMA, and PANTHER2D. Fault stresses are shown after 30 years of operation, using the default input parameters summarized in Table 5-1. For comparison also the uniaxial stress changes computed using the PT-field of SRIMA are shown. For DIANA3D and PANTHER2D a 50 m offset (0.5*reservoir thickness h) was included, for SRIMA this was not. For both DIANA3D and SRIMA the fault is located 100 m from the injection well, well within the cooled volume.

6.1.5 Applications of the different modeling tools

The modeling tools presented here can be used to assess the potential for fault reactivation in and around geothermal doublets, an important measure that helps to mitigate felt induced events. To assess the potential for fault reactivation it is important that the modeling tool that is used a) captures the appropriate mechanisms and trends, b) gives an adequate stress response on the fault, c) is conservative, and d) is quick enough to allow for sensitivity analysis or stochastic analysis, since the uncertainties in input parameters are large.

Although the OPM-DIANA 3D workflow captures more aspects affecting fault reactivation (3D pressure-temperature distribution, different doublet configurations, stiffness contrasts, fault offset) than SRIMA and PANTHER2D, it is computer-intensive. A (limited) sensitivity analysis could be performed to identify key parameters and mechanisms involved, but a fully stochastic analysis with 10,000s simulations is not feasible. For such an analysis, the faster tools presented here could be used. To a first order, SRIMA captures the temperature field and the fault stress changes well, and could be used to assess the extent of the cooled volume (2r_c), the extent of the volume where fault reactivation can occur (rcrit), and the reactivation potential on faults. The use of SRIMA should be limited to reservoirs where convective heat transfer is dominant in the reservoir, where fault offset remains limited (less than the reservoir height), and faults are fully open. We do recommend to evaluate the Coulomb Stress changes computed in SRIMA against a larger range of fault offsets in OPM-DIANA to better quantify the offsets for which the results of SRIMA remain valid. In addition, for large stiffness contrasts in the seal and base care should be taken when using SRIMA. In particular just outside the cooled front the fault stress changes in the reservoir may not be conservative with respect to those in OPM-DIANA, see the benchmark in Appendix A. One solution would be to include a small 'buffer' zone of ~100 m which would also account for differences in the temperature distribution near the cooling front (e.g. Figure 6-3).

In terms of the maximum shear stress on the fault PANTHER2D is conservative, perhaps overly so. PANTHER2D is currently most suitable for situations where sharp contrasts in pressure and or temperature exist between the reservoir and seal and base, such as for gas production, or when sharp contrasts in thermal conductivity are expected. However, because of its conservative nature

PANTHER2D could still be used to assess the potential for fault reactivation, and identification of key parameters, as done in Chapter 4. PANTHER outperforms the other two models when it comes to the computation of rupture length (in a fast semi-analytical way using Linear Elastic Fracture Mechanics LEFM). The other two models focus on fault reactivation, but fault reactivation is not the same as seismicity. Seismicity is driven by frictional weakening on the fault, following reactivation. Depending on the stress conditions, seismic slip can propagate beyond the fault area affected by the stress changes, which is crucial for the final event magnitude. Fault slip and/or frictional weakening is not yet included in SRIMA and OPM-DIANA. So when interested in the potential for rupture to propagate into the seal and base formations, or a first-order magnitude estimate (see 6.3), PANTHER2D could be used. Additionally, SRIMA and OPM-DIANA could be extended to include LEFM rupture calculation along the fault dip, or be coupled to the Dieterich seismicity rate model which relates Coulomb stress change rates to seismicity rates (Dieterich, 1994).

6.1.6 Main model assumptions and recommendations on further tool development

- <u>Linear elasticity:</u> In all three model approaches linear elasticity is assumed. However, significant inelastic strains may occur upon temperature or pressure changes (Pijnenburg et al., 2018, Soustelle, personal communication experiments for WarmingUp 4B). The effects of inelasticity remain yet to be evaluated. In addition, spatial distribution of parameters is uniform, whereas significant spatial variability of elastic parameters, permeability and porosity are expected.
- <u>Simplified geometries</u>: All three models approaches assume idealized geometries (axisymmetric reservoir, straight faults, single reservoir). This may suitable for generic modeling fault reactivation, gaining a basic understanding of the process, performing stochastic analyses, testing the effect of more complex behaviors such as fault weakening and inelastic deformation, but such simplified geometries may not be applicable for specific case studies. In reality, strike and dip of faults will vary substantially, which causes heterogeneous stresses along the fault. These more realistic geometries can be incorporated in MACRIS, which takes fault geometries directly from Petrel and related PT-fields from reservoir simulators as OPM Flow. This work is currently underway in WarmingUp 4B and will be reported at a later time. Also it is recommended to take into account stacked reservoirs (i.e. multiple sandstone members targeted with operations) to compute cooling and stress changes; such reservoir behaviors are relevant for e.g. the West Netherlands Basin.
- <u>Uniform formation properties:</u> Apart from variable Young's modulus and permeability (SRIMA, OPM-DIANA), other elastic and flow properties were kept uniform from formation to formation. In reality, strong lateral and vertical variations in e.g. permeability exist, leading to a heterogeneous shape of the cold front. This could result in some cooled pathways reaching the fault earlier in time, promoting reactivation. However, reactivated areas are expected to be smaller. It will be interesting to evaluate the effect of heterogeneous permeability on induced magnitudes.
- <u>Single doublet:</u> In the models approaches a single doublet (OPM-DIANA) or injection well (SRIMA) is modeled. However, as geothermal energy grows more and more doublets are created, which may lead to interference (e.g. Daniilidis et al., 2021). This might mean larger fault areas experience stress changes. It is recommended to optimize doublet placement both with respect to production as well as fault reactivation and event magnitudes.
- Open fault: In all three model approaches the fault is assumed to be open, not sealing. A sealing fault between the wells or close to the doublet affects the PT distribution (e.g. Daniilidis et al., 2021, van Wees et al., 2020) which also affects the reactivation potential. It is recommended to explore the effects of sealing or partially transmissive faults in future studies.
- <u>Lack of aseismic slip:</u> Both in OPM-DIANA and SRIMA fault slip (seismic or aseismic) is not explicitly modeled. Aseismic slip may however play an important role; for e.g. hydraulic fracturing in shales it is hypothesized that aseismic slip in the clay-rich target formation causes stress transfer to overlying, stiffer, more earthquake-prone formations (Eyre et al., 2019). This could be very relevant for the geothermal formations, which also contain lots of clay and

- sandstones, in particular if a stiffer formation overlies or underlies the geothermal target formation.
- <u>Lack of fault-weakening and rupture:</u> Apart from Panther2D, the fault weakening behavior that
 is fundamental for seismic fault slip is not considered. Future approaches could use the stress
 changes computed in the tools presented here, and link those to earthquake cycle models or
 dynamic rupture simulators, in 3D. This also allows for a link with monitoring data.

6.2 Key factors driving fault reactivation and seismicity

It is important to pinpoint the role of different input parameters on fault reactivation. To this end, stochastic analysis was performed using both SRIMA and PANTHER2D. Both analyses yield comparable outcomes, with the most important input parameters being:

- the stress path parameters Youngs modulus E and thermal expansion coefficient η , which both correlate positively with the reactivation potential
- in-situ stress ratio $K_0 = \sigma_n/\sigma_v$ which shows a negative correlation with the reactivation potential (lower ratio, higher criticality)
- the depth, since the temperature difference between the depth-dependent in-situ reservoir temperature and injected fluids (20°C) increases with depth.

The OPM-DIANA 3D workflow furthermore shows the importance of distance of the injection well from the fault and the orientation of the doublet with respect to the fault. For SRIMA reservoir height h is also important; this is because f_{crit} is calculated at different locations along a horizontal line in the reservoir. The smaller h, the larger the cooled radius and the higher the reactivation potential. For PANTHER2D the throw t was also of importance.

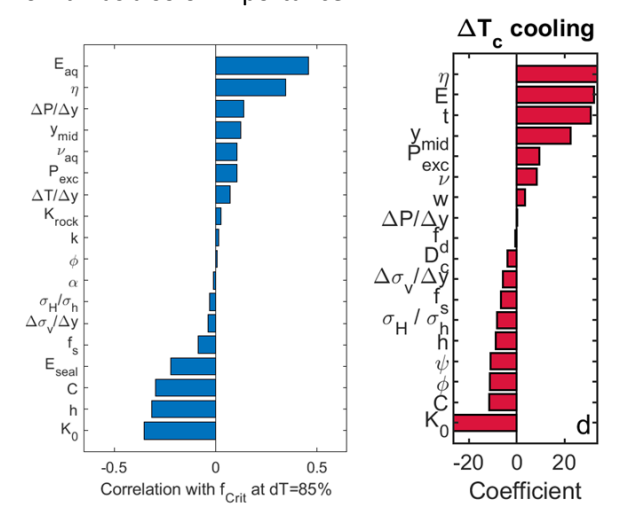


Figure 6-6 Linear regression coefficients for the stochastic modeling analysis in a) SRIMA and b) PANTHER. The risk measure used in a is the fraction of critical fault orientations f_{crit} which is measured over a horizontal line in the center of the reservoir, and the risk measure in b) is the temperature change required for fault reactivation. Note that the negative sign of the temperature changes results in a positive correlation for input parameters promoting fault reactivation as they increase in value. The same input parameters were used in both analyses, see for definition of symbols and values Table 3-1 and Table 4-1.

For the analyses in this report a generic set of input parameters relevant to geothermal operations in the Netherlands (and comparable reservoirs abroad) was used. Better characterization of the input parameters will reduce the uncertainty, and allow for region-specific or site-specific analysis of fault reactivation. In WarmingUp 4B an experimental program is underway where the thermo-mechanical parameters of sandstones from different geothermal targets will be measured. In addition, in WarmingUp 4B a region-specific and stratigraphy-specific analysis of leak-off test data will be done to better quantify the stress field in different areas in the Netherlands. Pending the results of these analyses the stochastic model analysis can be updated. Regardless, significant uncertainty will likely remain. In addition it is important to consider epistemic uncertainties deriving from model

assumptions. A limited amount of physics could be included in the models. For future modeling approaches it is important to consider the potential effects of inelastic deformation of the reservoir and seal and base rocks, and to include appropriate fault material models to distinguish between seismic and aseismic fault slip. Also, geometries used in this study are simplified generic geometries. Using MACRIS (van Wees et al., 2018, Candela et al., 2019) stress changes on realistic fault geometries based on the geological models can be computed; this work is also underway in WarmingUp 4B. Also, the effect of cooling of stacked reservoir formations, as e.g. present in the Alblasserdam Member in the Western Netherlands Basin is important to investigate. In any case, validation of models against field data remains essential.

6.3 Seismic rupture and magnitude - comparison depletion and cooling

In the end, it is not fault reactivation that is a problem, it is the occurrence of *seismic* fault slip on the reactivated fault, with magnitudes large enough to be felt at the surface. In this study we do not compute seismic catalogs, but the model results can give insight in the maximum magnitudes that may occur. The maximum expected magnitude M_{max} is an important component of seismic hazard and risk assessment (e.g. van Thienen-Visser et al., 2018, SODM, 2016). M_{max} is the upper bound of the frequency-magnitude distribution that is expected for a certain field/region. Note that the probability of M_{max} occurring is actually very low; mostly events that are recorded, if any at all, are (much) smaller than the M_{max} .

Moment magnitudes can be calculated from the seismic moment M_0 (here in Nm) using (Hanks & Kanamori, 1979)

$$M_{w} = (\log_{10} M_0 - 9.1)/1.5 ag{6-2}$$

The seismic moment for a finite, buried, dip-slip fault is approximately related to the stress drop $\Delta \tau$ and fault dimensions through (Kanamori & Anderson, 1975, Starr, 1928)

$$M_0 = \left(\frac{3\pi}{8}\right) \Delta \tau L_{dip}^2 L_{strike}$$
 6-3

The current seismic hazard analysis in place for the small gas fields (Dutch gas fields excluding Groningen) requires the computation of M_{max} (SODM, 2016). One of the two methodologies to compute M_{max} in the approach for the small gas fields assumes seismic slip will remain limited to the reservoir interval. It uses the maximum fault dimensions within or adjacent to the gas fields to constrain the along-dip fault length L_{dip} and the along-strike fault length L_{strike} which can be used to compute the seismic moment (Example 1A in Figure 6-7). It is interesting to compare fault dimensions and maximum magnitudes of these small gas fields to the geothermal case. A similar approach could be to use the dimensions of the cooled volume around the injection well to determine L_{strike} and L_{dip} . In some cases the cold front will reach a known fault structure, cooling it down partially. Here we do not investigate specific cases or regions; as an example we have set the cooled fault length to 20% of the diameter of the cold front (Example 2A). In a worst-case scenario undetected faults are present close to the injection well; in this case L_{strike} could be set equal to the diameter of the cold front $2r_c$ (Example 3A).

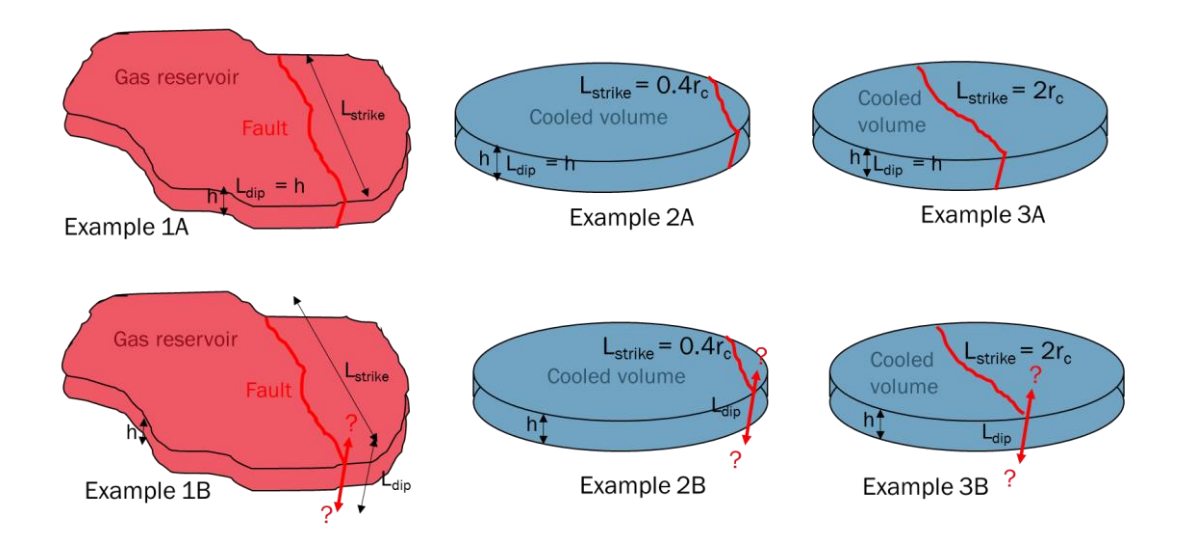


Figure 6-7 Example scenarios of the use of fault dimensions for the computation of M_{max} . Example 1A) L_{strike} is the maximum fault length within the gas reservoir, and L_{dip} the fault height within the gas reservoir. In Example 1B L_{strike} is the same but L_{dip} is computed using modeling (e.g. Panther 2D). Example 2A) cold front interacts with a known fault, example shown for the case L_{strike} is 40% of the radius of the cooled volume. Example 3A) worst-case scenario of undetected fault close to the injection well, assuming L_{strike} equals the diameter of the cooled volume. In all Examples B L_{strike} is the same as for A but L_{dip} is computed using modeling (Panther 2D). The stress drop for all A examples is fixed at 5 MPa, but the stress drop for all B examples also follows from modeling.

Typical measured L_{strike} for the small gas fields in the Netherlands fall between 1000 and 6000 m (Figure 6-8f). The diameter of the cold front estimated using Equation 4-2 for currently operational doublets after 30 years of operations is significantly smaller than the maximum fault length for gas reservoirs, mostly between 500 and 2000 m (Figure 6-8b). On the other hand, reservoir heights for the gas reservoirs are somewhat smaller than those of the geothermal target formations (Figure 6-8a and e). These dimensions could be used to give a first order estimate of M_{max} , but in addition to the dimensions, the stress drop must be specified. For the small gas fields a fixed stress drop of 5 MPa is used (Thienen-Visser et al., 2018, SODM, 2016). For the geothermal reservoir examples 2A and 3A the same value was assumed.

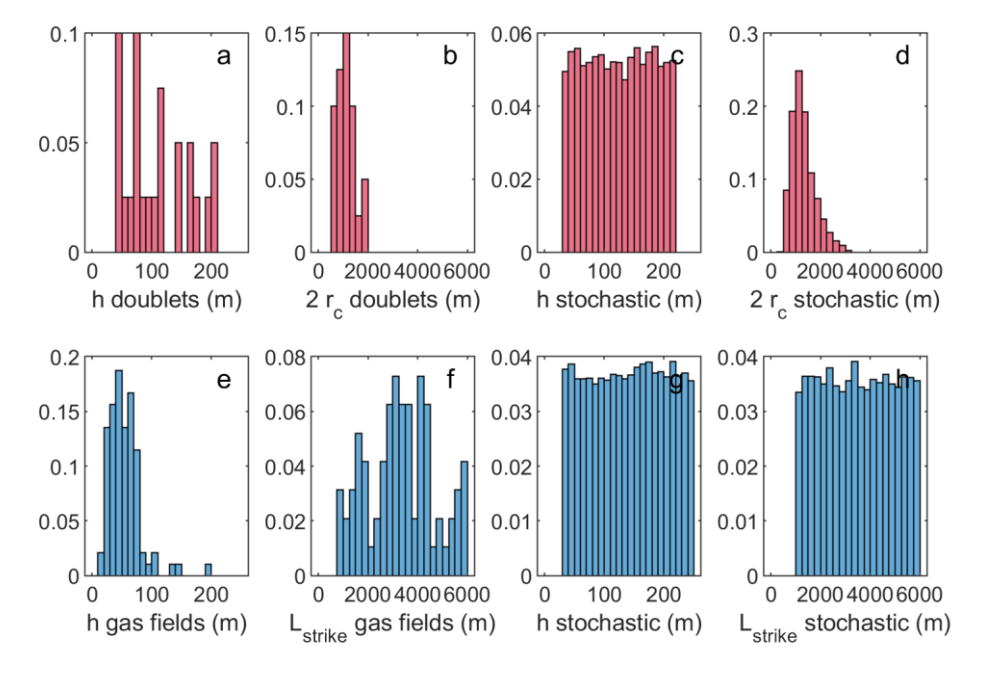


Figure 6-8 Histograms of normalized probabilities for dimensions of geothermal doublets and small gas fields. a) reservoir height observed for doublets in the Netherlands (i.e. thicknesses from Figure 2-2), b) diameter of cold front estimated using Equation 4-2

assuming c_{fluid} = 3771 Jkg⁻¹K⁻¹, a fluid density of 1052 kgm⁻³, specific heat capacity of the reservoir formation c_{rock} = 850 Jkg⁻¹K⁻¹, a rock density of 2200 kgm⁻³ (see text 4.3.6), an injection time of 30 years, and average annual flowrates of existing doublets (Figure 2-2, www.nlog.nl). Figures c and d show the same parameters, but now those as used in the stochastic analysis in Chapter 4 (i.e. uniform distributions). e) height of gas fields and f) maximum fault length L_{strike} within gas fields in the Netherlands (from Thienen-Visser et al., 2018). Figures g and h the same parameters, but now as used in the stochastic analysis for the depletion in Chapter 4 (i.e. uniform distributions).

Figure 6-9 a-c shows the histograms of maximum magnitudes computed for Examples 1A, 2A, and 3A ($L_{dip} = h$, $\Delta \tau = 5$ MPa), using dimensions from the stochastic model analysis of Panther (Figure 6-8 c, d, g, h), which are based on the observed dimensions of gas fields and cooled volumes. Maximum magnitudes for geothermal are within the same range as those for the gas fields, and are somewhat smaller (Figure 6-9 c vs a). Maximum magnitudes become significantly smaller if L_{Strike} is only a fraction of the radius of the cooled volume (Figure 6-9 b).

In all the A examples, vertical extension of rupture is limited by the reservoir height. However, stress perturbations can occur above and below the reservoir formation, due to pressure and temperature diffusion. Models indicate that in particular the latter can extend quite far (several 10s of m) into the seal and base formations (e.g. Section 3.4). The assumption that rupture remains within the reservoir formation may thus not always be conservative, as also noted in SODM (2016). Although the model approaches presented in this study do not model the full 3D dynamic rupture process following reactivation, Panther2D does give insight in the along-dip propagation of rupture. In Panther2D the frictional weakening and unstable slip following reactivation are included in the model workflow, and the resulting along-dip rupture length is determined by an energy balance using fracture mechanics. This gives a physics-based constraint on the propagation of rupture along the dip of the fault. Also, the stress drop is not imposed but follows from the frictional weakening parameters and the normal and shear stresses at the onset of rupture (initial + induced). Figure 6-9 d-f shows the histograms of maximum magnitudes computed for Examples 1B, 2B, and 3B, where L_{strike} is the same as for 1A, 2A, and 3A, but L_{dip} and $\Delta \tau$ follow from the Panther2D computations. Maximum magnitudes are generally larger than for the cases where L_{dip} = h (A-examples), even though the modeled stress drops are often somewhat smaller than the assumed 5 MPa for the A-examples. This is because:

- Rupture can propagate for some distance beyond the reservoir height, causing L_{dip} to be larger than h.
- Fault throw and dip are taken into account here, which was not the case for the A-scenarios. This increases the height of the perturbed interval to $^{\sim}(h + t)$, and $L_{dip} = h * \cos(90 dip)$.

The quadratic dependence of moment on L_{dip} causes these increases to have a significant effect. This emphasizes the importance of a better constraint on L_{dip} using physics-based modeling. Factors that need to be included in future research are the along-dip variations of in-situ stress and frictional properties related to different lithologies along the fault's dip.

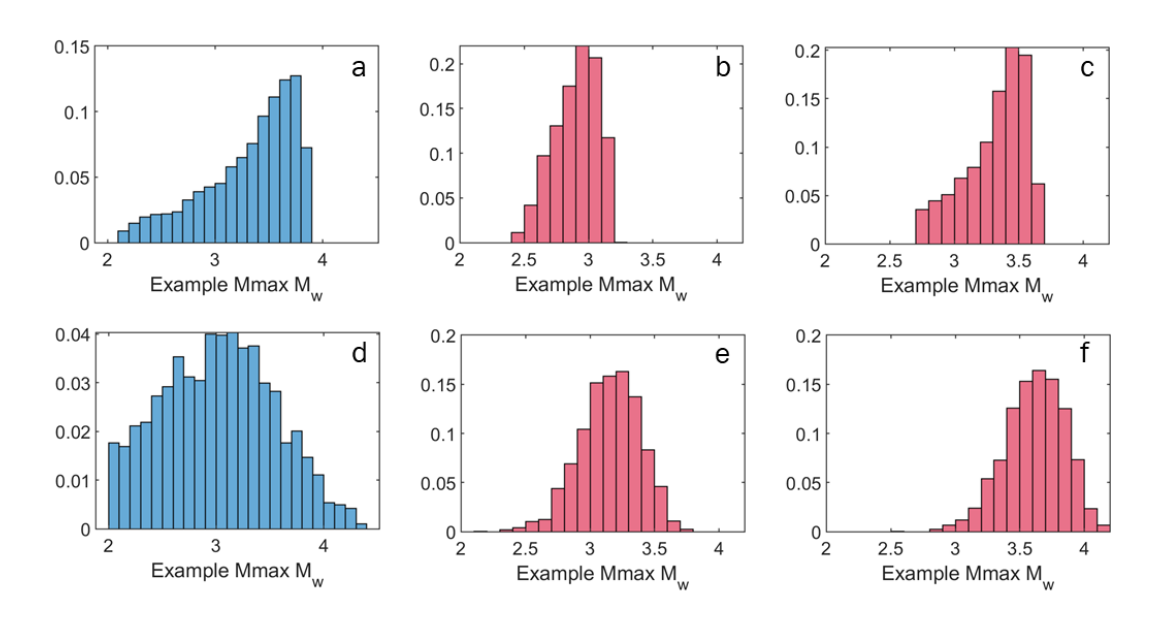


Figure 6-9 Histograms of maximum magnitude estimates for different example scenarios shown in Figure 6-7. A) Example 1A, b) example 2A, c) example 3A, d) example 1B, e) example 2B, f) example 3B, using dimensions from the stochastic parameter ranges evaluated in Chapter 4 (Figure 6-8 c, d, g, h).

At the same time, it is very likely the assumed L_{strike} is strongly overestimated. Fault strike and dip vary along the strike of the fault, causing a heterogeneous along-strike stress. Rupture will likely start in one of the high stress regions, but the low stress regions may prevent rupture to grow further along the strike of the fault, reducing L_{strike} . Also, large aspect ratios (L_{strike}/L_{dip}) are unlikely to occur; for large natural dip-slip earthquakes aspect ratio's do not exceed 8 (Weng & Yang, 2017). Exclusion of such aspect ratios would further reduce the maxima of the distributions shown in Figure 6-9. In addition, there are fundamental differences in the spatio-temporal characteristics of fault loading for gas depletion and geothermal operations. For gas production, faults in the reservoirs or reservoir compartments are relatively evenly loaded with time, as pressure equilibration through a gas field (compartment) usually is a fast process. Hence, the fault length affected by the stress change does not change with time, but the stress change increases linearly with the pressure drop (Figure 6-10a). For geothermal operations however, cooling is the main driver for the stress changes and the radius of the cooled volume r_c grows with injection time (e.g. Equation 4-5). When the cooled volume reaches a fault the stressed fault length will increase with injection time (Figure 6-10b), and the fault will get progressively reactivated with various (smaller) events spread over the injection time (e.g. Wassing et al., 2021). Hence it is likely that the L_{strike} of the (initial) induced events is much smaller than the diameter of the cold front (e.g. example 2A, 2B). These computed M_{max} for 2A and 2B show that the reduced L_{strike} assumed for cooling has a major effect on the M_{max} . Hence for geothermal both the stress drop is expected to be lower (due to the lower effective normal stress) than for gas depletion and the L_{strike} is expected to be smaller than for gas depletion due to the spatio-temporal evolution of the cold front. This stresses the importance of fault characterization in the subsurface and good estimates of the cold front propagation. A future directive for estimation of M_{max} is that the current model approaches and/or extended approaches modeling spatio-temporal evolution of progressive (seismic) events using improved post-failure behavior are validated against field observations where possible.

One important difference in expected (microseismic) response between depletion and cooling is that for cooling progressive reactivation of a fault is expected with time, whereas for depletion, a larger fault area may slip suddenly because fault are likely more evenly loaded with time (Figure 6-10). Indeed, several gas fields in the Netherlands have shown M > 3 earthquakes, without any smaller events preceding these larger events. For cooling on the other hand the reactivated fault area and event sizes are expected to grow with time (except if the initial fault strength is critical). This suggests that microseismic monitoring of geothermal projects can be very useful to assess the

seismicity potential with operation time, which helps to take potential mitigation measures in case seismicity rates or magnitudes increase. On the other hand, monitoring could be useful to rule out the likelihood of larger events; if it is known a fault has experienced substantial cooling but no seismicity has been recorded, it may suggest fault reactivation occurs aseismically or via small magnitudes (see next section). Monitoring of both the evolution of the cold front (e.g. WarmingUp 4C) and seismicity may hence be useful for mitigation of seismic hazard.

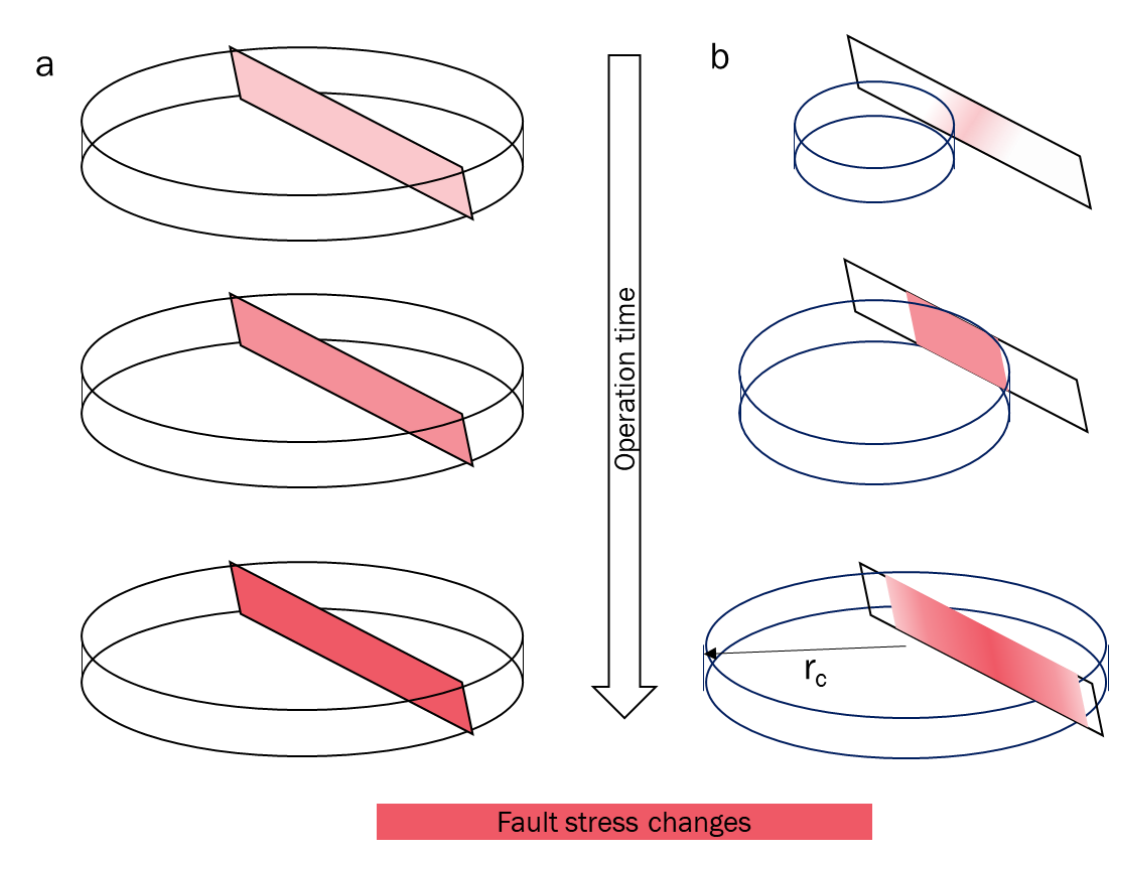


Figure 6-10 Schematic illustration of differences in fault stressing during gas depletion (a) and geothermal operations in sandstone reservoirs (b). R_c is the radius of the cooled volume, which increases with ongoing injection of cold water.

6.4 If cooling induces such significant stress changes, why have we not observed felt seismicity near geothermal doublets in sandstone reservoirs?

Regardless of which model is used, it is clear that thermo-elastic stress changes can be significant and could well lead to fault reactivation if the cooling front has reached a fault. However, no felt seismic events ($^{\sim}M > 2$) have been reported for doublets in the Netherlands, nor for doublets targeting similar formations in other countries (Buijze et al., 2019). This seems contradictory, but there may be various (complementary) explanations why no felt seismicity has (yet) been recorded. Some of these have been mentioned throughout the report, here we summarize briefly those points again.

• The limited operation time and positioning of well with respect to faults. The first doublet in the Netherlands started operating in 2006, and about 50% of the operational doublets only came online in 2015 or later (e.g. Mijnlieff, 2020). The radius of the cold front may thus only

- be several 100 m (Figure 4-3b). In the protocol for the seismic hazard screening of Q-con (2016), proximity to faults is penalized and doublets are often placed at some distance from known faults. It may thus be that the cold front has not reached known faults yet, or faults in the vicinity of the injection well experienced only a limited amount of cooling.
- Rock properties and inelastic strain: Rock stiffness in some of the poorly consolidated formation may be relatively low, which would cause lower thermoelastic stresses. Also, a large part of the deformation may be inelastic (e.g. Pijnenburg et al., 2018), which could change the stress path and potentially make it less destabilizing.
- <u>Stable in-situ stress</u>: Stress changes can be significant, but if the in-situ stress is stable fault failure may not be reached. Most parts in the Netherlands are characterized by low tectonic loading rates. In particular in the sedimentary cover, the in-situ stress may be far from critical as suggested by leak-off-test data (Muntendam-Bos, 2020). Within WarmingUp 4B further analyses into the in-situ stress state will be performed and reported at a later stage.
- <u>Heterogeneous in-situ stress</u>: Even if the stress in the reservoir is such that failure occurs, the in-situ stress in seal and base formations may be stable or even near-isotropic. Creepprone lithologies such as clays, mudstones, and evaporites will relax differential (shear stresses) over geological times and are likely to have a more stable in-situ stress state (e.g. Warpinski, 1989). If events were to occur within the target sandstone formation, they might be limited in size because the stress above and below the reservoir might be stable.
- Aseismic or low-frequency fault slip: Even if fault reactivation does occur, fault slip is not necessarily seismic. Seismic fault slip requires stress build-up to the failure strength, followed by rapid weakening of the fault strength through e.g. frictional weakening or a sudden loss of cohesion. The amount of frictional weakening varies with lithology. Laboratory experiments indicate that cohesive faults, and faults in competent rocks as for example granites, carbonates, and anhydrites are prone to frictional weakening and seismic slip. However, articular non-cohesive sandy and clay-rich fault gouges are not prone to seismic slip (Hunfeld et al., 2017), and may thus slide aseismically upon reactivation, as is inferred for e.g. fault reactivation during hydraulic fracturing (Eyre et al., 2019). In addition, cooling reduces the effective normal stress on the fault which also tends to promote aseismic slip (e.g. Guglielmi et al., 2015, Cappa et al., 2019). Note that aseismic slip can transfer stresses and load lithologies more prone to seismic slip (Eyre et al., 2019, Buijze, 2020), so knowledge of the local geology remains important for modeling of seismic and aseismic slip.
- Low stress drop: The initial amount of shear stress available on faults at 2 − 3 km depth is limited to <10 MPa for the normal faulting regime and likely stable in-situ stresses in the Netherlands (see e.g. Figure 4-5). Cooling also reduces the effective normal stresses. If rupture is driven purely by a reduction of friction, this means the shear stress drop (which is the friction drop multiplied with the effective normal stress) during rupture could be relatively low and the seismic events are less strong. Low stress drops are for example observed for seismic events close to the injection well during early stages of high pressure fluid injections (Chen & Abercrombie, 2020, Yu et al., 2020) where the high pressures lower the effective normal stress near the well.
- Progressive fault reactivation. The extent of the seismic slip event will largely be determined by the cooled area on the fault, unless the in-situ stress is critical and seismic slip can propagate outside of the cooled area. The highly stressed, cooled fault area, is elliptical in shape and grows with time, e.g. Figure 5-4, Figure 5-6. Early in the injection event sizes are thus expected to remain relatively small, possibly releasing some of the stress build-up within the elliptical area (Wassing et al., 2021). Subsequent events may be larger or remain limited to the 'outer ring' of the highly stressed area. Also, fault roughness can lead to smaller events compared to those on the planar fault geometry included in the current model.

For future geothermal developments and seismic hazard assessment studies it is essential that the role of these ingredients is further investigated through a combination of laboratory studies, monitoring and data-driven modeling.

7 Conclusions

Understanding the mechanisms of stress changes around geothermal doublets, the conditions under which these stress changes could reactivate pre-existing faults, and what controls the magnitudes of induced events, is crucial for site-specific hazard assessment and the development of mitigation measures. The use of geomechanical models can help understand important processes, key geological properties, and operational settings affecting fault reactivation and seismicity potential. In this report we present three modelling tools for analysis of fault reactivation potential near geothermal doublets, i.e. SRIMA (Seal and Reservoir Integrity Mechanical Analysis), PANTHER2D (Physics-based semi-Analytical Tool for Human-induced Earthquake Rupture), and OPM-DIANA FEA (Open Porous Media - DIANA Finite Element Analysis). SRIMA computes analytically the porothermoelastic stress changes around an injection well, assuming lateral convective flow and vertical temperature diffusion to the seal and base. PANTHER2D is a plane-strain model where a uniform temperature or pressure decrease in the reservoir and vertical diffusion to the seal and base are assumed. Fault stress changes are computed incorporating effects of offset reservoir compartments, and frictional weakening behavior is included to model the post-reactivation fault slip. OPM-DIANA is a 3D model workflow coupling the pressure and temperature changes in a geothermal doublet computed in the reservoir simulator OPM to the Finite Element package DIANA FEA. Each of these tools has its own merits and limitations, and each can be used for different purposes. SRIMA and PANTHER2D are (semi-)analytical tools which can give a first order assessment of fault reactivation, and in case of PANTHER2D, induced event magnitudes. The speed of these tools allows for incorporation of uncertainties in stochastic and sensitivity analyses, providing insights into the key factors that drive the potential of fault reactivation and seismicity. As they are based on simplified geometries, they are generally less well suited to capture the effects of geological complexity, heterogeneity and the spatio-temporal evolution of the cooling front. The FE numerical tool of OPM-DIANA analysis is complementary to the fast analyses of SRIMA and PANTHER2D, incorporating less parameter uncertainty but a higher degree of subsurface complexity such as stiffness contrast, different doublet configurations, and other heterogeneities. For a summary of the three model tools see Section 6.1 and Figure 6-1.

In this study, the three modelling tools were used to address the following questions:

- What are the key factors that drive fault reactivation and induced seismicity in geothermal doublet operations?
 - O Which parameters affect (the likelihood) of fault reactivation?
 - O Which parameters affect the extent of fault rupture?
- What is the extent of the cooling front and the critically perturbed zone around the geothermal doublets?
- What are the differences between seismicity induced by cooling (geothermal doublet operations) and depletion (gas production)?

The main conclusions for each topic are summarized below.

Key parameters for fault reactivation and seismicity during geothermal operations

- Stress changes for geothermal doublet operations in porous sandstone formations derive
 almost exclusively from temperature decreases around the injection well. The temperature
 decrease can be up to several 10's of degrees over hundreds of meters from the injection
 well, whereas pressure changes are often small (<1 MPa) and limited to the vicinity of the
 injection well.
- Normal faults that lie within the cooled volume around the injection well experience destabilization – i.e. the Coulomb stress on the fault increases. Destabilization occurs at the reservoir depth level, as well as just above in the seal and below in the base as these also experience some degree of cooling.

- The magnitude of the Coulomb stress changes depends predominantly on the reinjection temperature and the thermo-elastic properties of the reservoir formation. Faults offsetting cooled reservoir compartments enhance the Coulomb stress changes within the reservoir interval. In addition Coulomb stress changes increase with the radius of the cooled volume.
- A stiff seal and base formation results in larger Coulomb stress changes above and below
 the reservoir, and a larger fault area that experiences destabilization. In addition, in case of
 higher elasticity tensile stresses may develop, which increase the risk of inducing hydraulic
 fractures in the seal. This is because the seal and base also cool down, and the thermo-elastic
 stress in the seal and base are larger than those in the reservoir because of the higher
 Young's modulus.
- The fault reactivation potential depends on the Coulomb stress change in combination with the pre-existing, tectonic state of stress in and around the geothermal reservoir.
- Frictional weakening causes seismic instability to occur following reactivation. The extent of
 the seismic rupture along the dip of the fault is predominantly controlled by the initial stress
 ratio, fault dip, the frictional weakening parameters, and height of the reservoir interval.

Extent of the cooling front and critically perturbed zone

Cooling dominates the fault reactivation potential in and around geothermal doublets in porous sandstone reservoirs. The shape and size of the cooled reservoir volume is therefore an important indicator for fault reactivation. The main findings with respect to the cooling front (extent of cooling with distance from the injection well, r_{cooled}) and the radius of criticality (maximum distance from the injection well at which faults are reactivated) are listed here:

- The fault area that experiences positive Coulomb stress changes increases in size as the cooled volume around the injection well increases with operation time.
- The cooling front becomes increasingly asymmetric with increasing operation time, growing preferentially in the direction of the production well.
- When the cooling front has reached the fault an elliptical (doublet fault-parallel) area of higher Coulomb stress develops.
- The cooling-induced Coulomb stress reaches its maximum at depths where reservoir is juxtaposed against reservoir, and decreases gradually towards the seal and the base.
- Significantly more fault area experiences cooling & stressing for a geothermal doublet of which the connecting line is oriented perpendicular to the fault and crosses it.
- Destabilization and fault reactivation may occur both within and outside the cooling front due to stress transfer, although the stress changes decay rapidly beyond the cooled reservoir volume.
- When the initial criticality of the faults is moderate or low, the expected radius of criticality during injection mostly does not extend more than 30% beyond the thermal front. Radii of criticality that are much larger than the radius of cooling only occur in reservoirs that are initially already close to critically stressed. This observation can be used when designing geothermal operations in a reservoir with pre-existing faults or fault structures.
- Radii of criticality can be large (exceeding 500m), particularly in case of an initial stress regime that is already critical or in case of small reservoir thickness.

Differences between cooling-induced and depletion-induced fault reactivation / seismicity:

Although geothermal doublet operations in porous sandstone reservoir in the Netherlands and abroad have not (yet) resulted in the occurrence of felt seismicity, production from gas fields in similar sandstone reservoirs has led to felt seismicity. It is insightful to compare the stressing mechanisms between gas production and cooling.

• The direction of the stress path for cooling is on average more destabilizing than for depletion, which is reflected in a higher fault reactivation potential for cooling. This is because the effective normal stress decreases during cooling but increases during depletion. Note that this conclusion holds for faults that lie within the cooled or depleted area.

- Fault throw offsetting depleting or cooling reservoir formations tends to concentrate faults stresses and hence promotes reactivation for steep normal faults. The more abrupt variations in temperature or pressure changes between formations, the larger the stress concentrations, in particular near the edges of formations. The more diffuse the pressure and/or temperature profile, the smoother the stress changes and the smaller the stress concentrations. Plane-strain models applied to cooling however overestimate the stress changes w.r.t. the more applicable axisymmetric or full 3D modeling of cooling.
- Both for depletion and cooling, the height of the reservoir interval and fault throw, initial
 tectonic stress, fault dip, and amount of frictional weakening are the most important
 parameters controlling the along-dip rupture length.
- Rupture lengths are slightly larger for cooling than for depletion. This is because temperature changes extended further into the seal and base than pressure changes, causing stress changes over a larger fault length, and hence a larger rupture length.
- However, the event stress drop for cooling-induced events is smaller, as the effective normal stress has been reduced during cooling.
- Maximum magnitude estimates for cooling were in the same range as those estimated for the small gas fields in the Netherlands when assuming the events span the entire cooled volume. In the more likely scenario that only part of the cooled volume (see next point) maximum magnitude estimates for cooling are smaller.
- While for depletion the pressure change occurs relatively uniformly along the strike of the fault, for cooling around an injection well the fault area affected by the temperature change will grow with time. This is expected to lead to a different evolution of seismicity: fault reactivation and seismic moment release is expected to occur more gradually for cooling than for gas depletion. This should be verified by monitoring field cases through e.g. microseismic monitoring, tilt meters, fiber-optic measurements, and INSAR, and validating geomechanical models against those monitoring data.
- A gradual increase of fault area critically stressed by cooling and a gradual release of seismic
 energy with time could be favorable for mitigation of felt seismic events, as it increases the
 chance of detecting seismicity (and potentially unmapped faults) by seismic monitoring
 networks well before large fault segments are perturbed by the cooling front.

Recommendations:

- Model validation: Inform the presented geomechanical methods with lab- and field-derived input parameters, apply models to specific cases and validate models against field measurements such as microseismic monitoring.
- <u>Doublet design & optimization:</u> Choose optimal placement of wells from faults to limit stress
 changes on those faults. Evaluate whether there are case studies where it is known the cold
 front has reached the fault, and check whether monitoring observations are in line with
 expected behavior (reactivation or not, seismic or aseismic).
- Fault slip modeling: in the end, it is seismic fault slip of substantial magnitude that poses a problem at the surface, not fault reactivation itself. Clay-rich faults and faults in non-cohesive sedimentary rocks are generally less prone to seismic slip (Hunfeld, 2020), whereas faults in stiff rocks as carbonates and granites are more prone to seismic slip. Also frictional properties will vary along a fault's dip and strike. For an improved analysis of (maximum) magnitudes we recommend to model progressive cooling-induced fault reactivation in 3D through injection time, using the appropriate fault weakening behavior for fault slip.
- Experimental: Improve thermo-mechanical characterization of geothermal target reservoir rocks and seal and base rocks (primarily Young's modulus, thermal expansion coefficient), as these are fundamental for constraining the amount of stress change. In addition, investigate the elasto-plastic and visco-plastic rock behavior experimentally, as these may cause different stress paths compared to using linear elastic rock properties. (Experimental characterization of the reservoir rocks is part of the WarmingUp 4B project results will be reported in a separate document). Furthermore Investigate the friction, cohesion, and

- dynamic weakening behavior of fault rock materials. Clay-rich and low-cohesive cataclastic faults may be prone to aseismic slip rather than seismic slip, thus significantly lowering the seismogenic potential of a formation.
- <u>Upscaling:</u> Upscaling of lab-derived elastic properties to the reservoir scale using correlations with well logs.
- <u>Field data</u>: Improve characterization of the initial stress field, and make a distinction between regions and lithologies. In particular clay-rich formations under- or overlying reservoir formations may carry only a low tectonic stress, which would prevent seismic events from growing large. (Characterization of the in-situ stress field based on newly available leak-off-test and minifrac data provided by NAM is part of the WarmingUp project 4B; results will be reported in a separate document). Improve characterization of faults in the main geothermal target formations, looking in particular at their orientations and fault mineralogy and whether faults are cohesive / sealing or not.
- <u>Case studies</u>: Include realistic fault geometries and permeability fields (geothermal-induced fault reactivation on faults as included in Petrel will be studied in WarmingUp 4B and results will be reported in a separate document).
- <u>Interference</u>: Model the effect of multiple doublets located close together. Does the interference give rise to larger stress changes? Can well positioning be optimized in terms of low fault reactivation potential and high productivity?

8 References

- Ampuero, J., & Ben-Zion, Y. (2008). Cracks, pulses and macroscopic asymmetry of dynamic rupture on a bimaterial interface with velocity-weakening friction. Geophysical Journal International, 173 (2), 674-692.
- Bayart, E., Svetlizky, I., & Fineberg, J. (2016). Fracture mechanics determine the lengths of interface ruptures that mediate frictional motion. Nature Physics, 12 (2), 166.
- Buijze, L. (2020). Numerical and experimental simulation of fault reactivation and earthquake rupture applied to induced seismicity in the Groningen gas field. (PhD Thesis, Utrecht University).
- Buijze, L., van Bijsterveldt, L., Cremer, H., Paap, B., Veldkamp, H., Wassing, B. B., van Wees, J., van Yperen, G. C., & ter Heege, J. H. (2019a). Review of induced seismicity in geothermal systems worldwide and implications for geothermal systems in the Netherlands. Netherlands Journal of Geosciences, 98
- Buijze, L., van den Bogert, P., Wassing, B. B. T., & Orlic, B. (2019b). Nucleation and Arrest of Dynamic Rupture induced by Reservoir Depletion. Journal of Geophysical Research: Solid Earth, 124 (4), 3620-3645.
- Buijze, L., van den Bogert, P. A. J., Wassing, B. B. T., Orlic, B., & ten Veen, J. (2017). Fault reactivation mechanisms and dynamic rupture modelling of depletion-induced seismic events in a Rotliegend gas reservoir. Netherlands Journal of Geosciences, 96 (5), s131-s148.
- Busch, A., Amann, A., Bertier, P., Waschbusch, M., & Krooss, B. M.The Significance of Caprock Sealing Integrity for CO2 Storage. SPE International Conference on CO2 Capture, Storage, and Utilization, New Orleans, Louisiana, USA,10-12 November 2010. SPE 139588Candela, T., Van Der Veer, E. F., & Fokker, P. A. (2018). On the importance of thermoelastic stressing in injection-induced earthquakes. Rock Mechanics and Rock Engineering, 51(12), 3925-3936.
- Candela, T., E. F. Van Der Veer, and P. A. Fokker. "On the importance of thermo-elastic stressing in injection-induced earthquakes." Rock Mechanics and Rock Engineering 51.12 (2018): 3925-3936.
- Candela, T., Osinga, S., Ampuero, J., Wassing, B., Pluymaekers, M., Fokker, P. A., van Wees, J., de Waal, H. A., & Muntendam-Bos, A. G. (2019). Depletion-induced seismicity at the Groningen gas field: Coulomb rate-and-state models including differential compaction effect. Journal of Geophysical Research: Solid Earth, 124 (7), 7081-7104.
- Cappa, F., Scuderi, M. M., Collettini, C., Guglielmi, Y., & Avouac, J. P. (2019). Stabilization of fault slip by fluid injection in the laboratory and in situ. Science advances, 5(3), eaau4065.
- Carey, J. W., Svec, R., Grigg, R., Lichtner, P. C., Zhang, J., & Crow, W. (2009). Wellbore integrity and CO2-brine flow along the casing-cement microannulus. Energy Procedia, 1 (1)
- Chen, X., & Abercrombie, R. E. (2020). Improved approach for stress drop estimation and its application to an induced earthquake sequence in Oklahoma. Geophysical Journal International, 223(1), 233-253.
- Daniilidis, A., Nick, H. M., & Bruhn, D. F. (2021). Interference between geothermal doublets across a fault under subsurface uncertainty; implications for field development and regulation. Geothermics, 91, 102041.
- Eshelby, J. D. (1957). The determination of the elastic field of an ellipsoidal inclusion, and related problems. Proceedings of the Royal Society of London. Series A, Mathematical and Physical Sciences, 241 (1226), 376-396.
- Eyre, T. S., Eaton, D. W., Garagash, D. I., Zecevic, M., Venieri, M., Weir, R., & Lawton, D. C. (2019). The role of aseismic slip in hydraulic fracturing–induced seismicity. Science advances, 5(8), eaav7172.

- Farsimadan, M., Dehghan, A. N., & Khodaei, M. (2020). Determining the domain of in situ stress around Marun Oil Field's failed wells, SW Iran. Journal of Petroleum Exploration and Production Technology, 10(4), 1317-1326.
- Galis, M., Ampuero, J., Mai, P. M., & Kristek, J. (2019). Initiation and arrest of earthquake ruptures due to elongated overstressed regions. Geophysical Journal International, 217 (3), 1783-1797.
- Galis, M., Ampuero, J. P., Mai, P. M., & Cappa, F. (2017). Induced seismicity provides insight into why earthquake ruptures stop. Science Advances, 3 (12)
- Galis, M., Pelties, C., Kristek, J., Moczo, P., Ampuero, J., & Mai, P. M. (2015). On the initiation
 of sustained slip-weakening ruptures by localized stresses. Geophysical Journal
 International, 200 (2), 888-907.
- Guglielmi, Y., Cappa, F., Avouac, J. P., Henry, P., & Elsworth, D. (2015). Seismicity triggered by fluid injection—induced aseismic slip. Science, 348(6240), 1224-1226.
- Hanks, T. C., & Kanamori, H. (1979). A moment magnitude scale. Journal of Geophysical Research: Solid Earth, 84(B5), 2348-2350.
- Haug, C., Nüchter, J. -., & Henk, A. (2018). Assessment of geological factors potentially affecting production-induced seismicity in North German gas fields. Geomechanics for Energy and the Environment, 16, 15-31.
- Hunfeld, L. B., Niemeijer, A. R., & Spiers, C. J. (2017). Frictional properties of simulated fault gouges from the seismogenic groningen gas field under in situ P–T-chemical conditions. Journal of Geophysical Research: Solid Earth, 122(11), 8969-8989.
- Hunfeld, L. B., Chen, J., Hol, S., Niemeijer, A. R., & Spiers, C. J. (2020). Healing behavior of simulated fault gouges from the Groningen gas field and implications for induced fault reactivation. Journal of Geophysical Research: Solid Earth, 125(7), e2019JB018790.
- Hunfeld, L. B. (2020). Frictional properties of simulated fault gouges from the Groningen gas field and implications for induced seismicity. (PhD Dissertation, Utrecht University).
- Ito, Y., Obara, K., Shiomi, K., Sekine, S., & Hirose, H. (2007). Slow earthquakes coincident with episodic tremors and slow slip events. Science, 315(5811), 503-506.
- Jansen, J., Singhal, P., & Vossepoel, F. (2019). Insights from closed-form expressions for injection-and production-induced stresses in displaced faults. Journal of Geophysical Research: Solid Earth, 124 (7), 7193-7212.
- Kammer, D. S., & McLaskey, G. C. (2019). Fracture energy estimates from large-scale laboratory earthquakes. Earth and Planetary Science Letters, 511, 36-43.
- Kammer, D. S., Radiguet, M., Ampuero, J., & Molinari, J. (2015). Linear elastic fracture mechanics predicts the propagation distance of frictional slip. Tribology Letters, 57 (3), 23.
- Koning, E. J. L. (1988). Waterflooding under fracturing conditions. PhD Thesis, Technical University Delft.
- Koning, E. J. L., & Niko, H. (1985). Fractured water-injection wells: a pressure falloff test for determining fracture dimensions. In SPE Annual Technical Conference and Exhibition. OnePetro, SPE 14458.
- Levandowski, W., Weingarten, M., & Walsh III, R. (2018). Geomechanical sensitivities of injection-induced earthquakes. *Geophysical Research Letters*, 45(17), 8958-8965.
- Mijnlieff, H. F. (2020). Introduction to the geothermal play and reservoir geology of the Netherlands. *Netherlands Journal of Geosciences*, 99.
- Mulders, F. M. M. (2003). Modelling of stress development and fault slip in and around a producing gas reservoir. (Doctoral Thesis, Technical University of Delft).
- Myklestad, N.O. (1942). Two problems of thermal stress in the infinite solid. J. Applied Mechanics, September 1942, A-136 A-143
- Nield, D. A., & Bejan, A. (2017). *Convection in porous media* (Fifth Edition). New York:
- Orlic, B. (2009). Some Geomechanical Aspects of Geological CO2 Sequestration. KSCE Journal of Civil Engineering, 13 (4), 225-232.

- Orlic, B., & Wassing, B. B. T. (2013). A Study of Stress Change and Fault Slip in Producing Gas Reservoirs Overlain by Elastic and Viscoelastic Caprocks. Rock Mechanics and Rock Engineering, 46 (3), 421-435.
- PBL, CBS, TNO, RIVM, & RVO. (2020). Klimaat- en Energieverkenning 2020. Den Haag: Planbureau voor de Leefomgeving (PBL).
- Perkins, T. K., & Gonzalez, J. A. (1985). The effect of thermoelastic stresses on injection well fracturing. *Society of Petroleum Engineers Journal*, *25*(01), 78-88.
- Q-Con & IF-Technology (2016). Defining the Framework for Seismic Hazard Assessment in Geothermal Projects.
- Rasmussen, A. F., Sandve, T. H., Bao, K., Lauser, A., Hove, J., Skaflestad, B., ... & Thune, A. (2021). The open porous media flow reservoir simulator. *Computers & Mathematics with Applications*, 81, 159-185.
- Rioseco, E. M., Löhken, J., Schellschmidt, R., & Tischner, T. (2013, February). 3-D geomechanical modeling of the stress field in the North German basin: case study GeneSysborehole GT1 in Hanover Groß-Buchholz. In 38th Workshop on Geothermal Reservoir Engineering (pp. 11-13).
- Ripperger, J., Ampuero, J. -., Mai, P. M., & Giardini, D. (2007). Earthquake source characteristics from dynamic rupture with constrained stochastic fault stress. Journal of Geophysical Research: Solid Earth, 112 (B4)
- Roest, J. P. A., & Kuilman, W. Geomechanical analysis of small earthquakes at the Eleveld gas reservoir. Rock Mechanics in Petroleum Engineering, Delft, The Netherlands, August 1994. SPE-28097-MS
- Rutqvist, J., & Tsang, C. -. (2002). A study of caprock hydromechanical changes associated with CO2-injection into a brine formation. Environmental Geology, 42, 296-305.
- Saeid, S., & Barends, F. B. J. (2009, October). An extension of Lauwerier's solution for heat flow in saturated porous media. *In Proc. COMSOL Conf. Milan.*
- SODM. (2016). Methodiek voor risicoanalyse omtrent geïnduceerde bevingen voor gaswining - Tijdelijke leidraad voor adressering MBB. Report No. VERSIE 1.2, Den Haag: State Supervision of Mines.
- Soltanzadeh, H., & Hawkes, C. D. (2008). Semi-analytical models for stress change and fault reactivation induced by reservoir production and injection. Journal of Petroleum Science and Engineering, 60, 71.
- Soltanzadeh, H., & Hawkes, C. D. (2009). Induced poroelastic and thermoelastic stress changes within reservoirs during fluid injection and production. Porous Media: Heat and Mass Transfer, Transport and Mechanics, , 27.
- Stichting Platform Geothermie, DAGO, Stichting Warmtenetwerk, & EBN. (2018). Masterplan Aardwarmte in Nederland.
- Svetlizky, I., & Fineberg, J. (2014). Classical shear cracks drive the onset of dry frictional motion. Nature, 509 (7499), 205-208.
- ter Heege, J. H., van Bijsterveldt, L., Wassing, B. B. T., Osinga, S., Paap, B., & Kraaijpoel, D. (2020). Induced seismicity potential for geothermal projects targeting Dinantian carbonates in the Netherlands. Report by SCAN, executed by Ministry of Economic Affairs (EZK), EBN, TNO, and Interreq.
- TNO-AGE. (2021). Delfstoffen en aardwarmte in Nederland Jaarverslag 2020. Den Haag: Ministerie van Economische Zaken en Klimaat (EZK). Executed by TNO-AGE.
- Uenishi, K., & Rice, J.,R. (2003). Universal nucleation length for slip-weakening rupture instability under nonuniform fault loading. Journal of Geophysical Research, 108 (B1), 2042.
- van den Bogert, P. A. J. (2018). Depletion-induced fault slip and seismic rupture. 2D Geomechanical models for the Groningen field, The Netherlands. Assen: Nederlandse Aardolie Maatschappij B.V. . (Executing organisation: Shell Global Solutions International B.V.. Editors: van Elk, Jan and Doornhof, Dirk)

- van den Bogert, P. A. J. (2015). Impact of various modelling options on the onset of fault slip and fault slip response using 2-dimensional Finite-Element modelling. Restricted, Report No. SR.15.11455, Rijswijk: Shell Global Solutions International B.V.
- van den Bogert, P. A. J. (2018). Depletion-induced fault slip and seismic rupture. 2D Geomechanical models for the Groningen field, The Netherlands. Assen: Nederlandse Aardolie Maatschappij B.V. (Executing organisation: Shell Global Solutions International B.V.. Editors: van Elk, Jan and Doornhof, Dirk)
- van den Bogert, P. A. J., & van Eijs, R. M. H. E. (2020). Why Mohr-circle analyses may underestimate the risk of fault reactivation in depleting reservoirs. International Journal of Rock Mechanics and Mining Sciences, 136, 104502.
- van Thienen-Visser, K., Roholl, J. A., van Kempen, B. M. M., & Muntendam-Bos, A. G. (2018). Categorizing seismic risk for the onshore gas fields in the Netherlands. Engineering Geology, 237, 198-207.
- van Wees, J., Pluymaekers, M., Osinga, S., Fokker, P. A., Van Thienen-Visser, K., Orlic, B., Wassing, B. B. T., Hegen, D., & Candela, T. (2019). 3-D mechanical analysis of complex reservoirs: a novel mesh-free approach. *Geophysical Journal International*, 219 (2), 1118-1130.
- Wassing, B. B. T., Buijze, L., & Orlic, B. (2017). Fault reactivation and fault rupture in producing gas fields with elastic and visco-elastic caprocks. *51st Rock Mechanics Symposium, San Francisco, California, USA*, *25-28 June 2017.* ARMA 17-355
- Wassing, B. B. T., Candela, T., Osinga, S., Peters, E., Buijze, L., Fokker, P. A., & Van Wees, J. D. (2021). Time-dependent Seismic Footprint of Thermal Loading for Geothermal Activities in Fractured Carbonate Reservoirs. Frontiers in Earth Science, 805.
- Willems, C. J. L. (2017). Doublet deployment strategies for geothermal Hot Sedimentary Aquifer exploitation. Application to the Lower Cretaceous Nieuwerkerk Formation in the West Netherlands Basin. (PhD, Technical University Delft).
- Willems, C. J., Vondrak, A., Mijnlieff, H. F., Donselaar, M. E., & Van Kempen, B. M. (2020). Geology of the Upper Jurassic to Lower Cretaceous geothermal aquifers in the West Netherlands Basin—an overview. Netherlands Journal of Geosciences, 99.
- Yu, H., Harrington, R. M., Kao, H., Liu, Y., Abercrombie, R. E., & Wang, B. (2020). Well proximity governing stress drop variation and seismic attenuation associated with hydraulic fracturing induced earthquakes. Journal of Geophysical Research: Solid Earth, 125(9), e2020JB020103.
- Zbinden, D., Rinaldi, A. P., Urpi, L., & Wiemer, S. (2017). On the physics-based processes behind production-induced seismicity in natural gas fields. Journal of Geophysical Research: Solid Earth, 122 (5), 3792-3812.

Bijlage A SRIMA background theory and benchmark

The fast analytical tool SRIMA (Seal and Reservoir Integrity Mechanical Analysis) presented in Chapter 3 computes pressure and temperature changes around an injection well, the subsequent poro-thermo-elastic stress changes, and associated measures for reactivation and hydraulic fracturing risks. The present Appendix details how the pressure and temperature changes are computed analytically, and under which simplifications (Section A.1 and A.2). Sections A.3 and A.4 detail how, built on these, the induced stresses are calculated; Section A.5 shows the correlations used for the risk measures. In Section A.6 the validity of the pressure and temperature approximations is tested by comparing the computed pressure and temperatures to outcomes of the reservoir simulator Eclipse. The calculation of poro-thermo-elastic stresses from the pressure and temperature changes also involves several simplifications. The validity of these simplifications is addressed by comparing the poro-thermo-elastic stress changes computed in SRIMA to those of DIANA Finite Element Analysis, both using the same pressure and temperature input (Section A.7). This comparison is done for both uniform elasticity (Section A.8), and for seal and base formations with a 4x higher (Section A.9) or lower stiffness (Section A.10) compared to the reservoir formation.

The benchmark of pressure and temperature in SRIMA to Eclipse shows that the correspondence is excellent. The approximations of horizontal, developed, convective flow of fluid and heat in the reservoir and diffusive flow in the bounding layers works well, The approximation made for the pressure in the bounding layers adequately covers the distortion from purely vertical flow.

The comparison of poro-thermo-elastic stress changes in SRIMA to DIANA FE shows that, for uniform elasticity:

- The match within the cooled reservoir volume is good for the horizontal stress change (<7% difference), but vertical stress decrease is underestimated by SRIMA. The vertical stress increase to the side of the cooled reservoir volume is also underestimated in SRIMA.
- SRIMA yields larger Coulomb Stress changes within the cooled rock volume and is thus conservative.
- Just to the side of the cooled rock volume SRIMA underestimates the Coulomb stress change and is not conservative. This is due to stress arching not being accounted for in SRIMA.

For stiffer seal and base formations the benchmark exercise showed that (Section A.9):

- The match within the reservoir formation is good (<5% difference), better even than for uniform elasticity
- In the cooled parts of the seal and base the difference in stress change is larger than for uniform elasticity (<30% difference between SRIMA and DIANA) but SRIMA yields conservative values for fault reactivation in a normal faulting setting
- To the sides of the cooled parts in the seal and base formation SRIMA underestimates the Coulomb stress change i.e. not conservative in a normal faulting setting.

For more compliant seal and base formations the comparison shows that:

- Differences in horizontal stress within the cooled reservoir formation can be considerable, up to 25%.
- SRIMA again overestimates Coulomb stress change within the cooled reservoir formation and is thus conservative.
- SRIMA underestimates (Coulomb) stress changes to the side of the cooled volume and is not conservative at this location.

To summarize, stress changes computed by SRIMA within the cooled reservoir formations typically are in good agreement with FE simulations (<10% difference), though the difference is larger in case the seal and base formation are more compliant than the reservoir (<25% difference). In both cases SRIMA is conservative for fault reactivation in a normal faulting setting as it overestimates Coulomb

Stress Changes. The good to reasonable agreement between computed stresses, and SRIMA being conservative in terms of CSC indicates that SRIMA is a useful tool to study fault reactivation around an injection well. However, care must be taken when considering reactivation just to the side of the cooled volume; here SRIMA systematically underestimates the Coulomb Stress change and is thus not conservative. This effect is due to the lack of stress arching in SRIMA for heterogeneous elasticity, and the effect becomes particularly important when seal and base have a significantly lower stiffness than the reservoir as arching effects become stronger.

A.1 Temperature field

Injection of fluid into the reservoir affects its temperature through advection and conduction. The differential equation describing these two effects reads

$$(\rho C)_{rock} \frac{\partial T}{\partial t} + (\rho C)_{fluid} \mathbf{v} \cdot \nabla T = \nabla \cdot (K_{rock} \nabla T)$$
8-1

with ρ the density; C the specific heat; \mathbf{v} the superficial fluid velocity; K_{rock} the heat conductivity. This equation assumes equal temperature of the fluid and the solid where they are in contact.

The balance between diffusion and convection is described by the Péclet number: $Pe = \frac{(\rho C)_{fluid} \cdot vL}{K_{rock}}$, in which L is a representative length [Nield & Bajan, 2017]. For a Péclet number larger than 1 we must have $vL > \frac{K_{rock}}{(\rho C)_{fluid}}$. This is normally the case for injection into a permeable aquifer, therefore the energy balance in the aquifer will usually be convection dominated.

For a semi-analytical solution we limit ourselves to the simplified case of constant-rate injection, purely radial-horizontal convection in a convection-dominated permeable layer, and purely vertical diffusion in the low-permeability overlying and underlying layers (Figure 3-1). The solution has been formulated by different authors; we use the formulation by Candela et al (2018). The solution for a layer of thickness h (centered around z=0) in which cool fluid is injected with a mass injection rate \dot{m} from t=0 onward, in the bounding layers and in the aquifer, reads

$$T_{seal}(r,z,t) = T_{res} + \left(T_{inj} - T_{res}\right) \operatorname{erfc}\left[\frac{ar^{2} + b\left(|z| - \frac{h}{2}\right)}{\sqrt{t - cr^{2}}}\right] H(t - cr^{2})$$

$$T_{aq}(r,t) = T_{res} + \left(T_{inj} - T_{res}\right) \operatorname{erfc}\left[\frac{ar^{2}}{\sqrt{t - cr^{2}}}\right] H(t - cr^{2})$$

$$a = \frac{\pi K_{rock}}{\dot{m}c_{fluid}\sqrt{\kappa_{T}}}; b = \frac{1}{2\sqrt{\kappa_{T}}}; c = \frac{\pi h\xi\rho_{w}}{\dot{m}}$$

$$\kappa_{T} = \frac{K_{rock}}{(\rho C)_{rock}}; \xi = \frac{\rho_{rock}c_{rock}}{\rho_{w}c_{fluid}}$$

$$r_{cooled} = \left(\frac{qt_{inj}}{\xi h\pi}\right)^{0.5}$$

Results of a comparison of the ensuing fields and a validation with results obtained with numerical techniques is given in the Section A.6.

A.2 Pressure field

The pressure associated with injection of water into an aquifer depends on a number of parameters: injection rate, time evolved, aquifer permeability and height, skin, water viscosity of cold (injected) and warm (reservoir temperature) water, distribution of reservoir properties, well configuration. In a highly permeable aquifer, a pressure distortion will quickly propagate into the reservoir and the

pressure profile around an injection well will become approximately logarithmic (Orlic, 2009). The hot and cold reservoir parts will have their own logarithmic slope because of the temperature-dependent viscosity. If we have obtained a steady-state pressure distribution with negligible leakage to overlying and underlying layers, with a constant-pressure boundary at a distance r_e , and constant viscosity μ , the pressure distribution in the reservoir is given by

$$P_{aq}(r) = \begin{cases} P_0 + \frac{\dot{m}\mu_h}{2\pi\rho_w k_{aq}h} [\ln r_e - \ln r] & (r > r_c) \\ P_0 + \frac{\dot{m}\mu_h}{2\pi\rho_w k_{aq}h} [\ln r_e - \ln r_c] \\ + \frac{\dot{m}\mu_c}{2\pi\rho_w k_{aq}h} [\ln r_c - \ln r] \end{cases}$$

$$(r \le r_c)$$

$$(r \le r_c)$$

Due to the low permeability in the adjacent layers, the pressure distribution there is not stationary and must by determined through the application of Darcy flow and mass balance. Like the temperature, this pressure is also described by a diffusivity equation:

$$\frac{\partial P}{\partial t} = \kappa_{P,z} \frac{\partial^2 P}{\partial z^2} + \kappa_{P,r} \frac{\partial^2 P}{\partial r^2} \left(t \ge 0; |z| \ge \frac{h}{2} \right)$$

$$P\left(z > \frac{h}{2}, t = 0 \right) = P_0$$

$$P\left(z = \frac{h}{2}, t \right) = P_{aq}(r)$$
8-4

The hydraulic diffusivity $\kappa_P = \frac{k_{seal}}{\phi \mu c}$ (k – permeability; ϕ – porosity; μ – viscosity; c – compressibility); the value may be different for horizontal and vertical directions due to permeability anisotropy. In contrast to thermal diffusion, a simple 1D diffusion into seal and base will not work for the pressure. The reason is the large variation of the pressure close to the well. Pressure that is induced in the seal in the center of the reservoir will "leak away" both vertically and horizontally, and the second term in the pressure diffusion equation cannot be discarded. Alternatively one can state that the pressure in the seal at some distance is influenced by an extended pressurized area of the reservoir. We therefore adopted an equation similar to the expression for temperature but with the temperature substituted by an effective pressure for such a cylinder:

$$P(r,z,t) = P_{aq}\left(r + z - \frac{h}{2}\right) \operatorname{erfc} \frac{z - \frac{h}{2}}{2\sqrt{\kappa_P t}}$$
8-5

For the diffusivity in the seal and the base we take the value as calculated for the virgin reservoir temperature. This will result in an overestimate of the pressure close to the well and close to the interface. A validation of the pressure field with numerical techniques is also provided in Section A.6.

A.3 Thermo-elastic stress

When the temperature and pressure distributions (ΔT and ΔP) are known and the mechanical behavior is linearly elastic, the induced stresses and strains ($\Delta \sigma_{ij}$ and ε_{ij}) must obey the porothermo-elastic constitutive equation. Selecting the sign convention with compressive stresses positive, we have

$$\Delta \sigma_{ij} = 2G \left[\varepsilon_{ij} + \frac{\nu}{1 - 2\nu} \varepsilon \delta_{ij} \right] + (\alpha \Delta P + \beta_T \Delta T) \delta_{ij}$$
 8-6

Here, G is the shear modulus; ν the Poisson ratio, α is Biot constant, $\beta_T = \alpha_b K = 3\eta K = \frac{\eta E}{1-2\nu}$ the product of the volumetric thermal expansion coefficient α_b times the bulk modulus K; η the linear

thermal expansion coefficient. The constitutive equation needs to be solved with the appropriate boundary conditions.

For a cooled cylinder with discontinuous temperature profile at the boundary, analytical equations are available for the induced thermo-elastic stresses, both inside and outside the cooled cylinder (Carey et al., 2009; Rutqvist & Tsang, 2002). These can be easily implemented. We discretize the calculated temperature profile in the reservoir, and deploy superposition of the resulting cylinders. Besides the cooled part of the reservoir, there is also cooling of part of the seal and the base. For the effect of this zone, we closely look at the Myklestad solutions for a very flat cooled cylinder, i.e. a cylinder with a large radius / height ratio, and at radial locations well within the cooling radius. Such cylinders result in an induced horizontal stress in the cylinder of about $\frac{\eta E}{1-\nu}\Delta T$; outside it is approximately zero. Vertical induced stresses virtually vanish, both inside and outside such cylinders. Our estimate for the thermal stress is therefore a superposition of Myklestad's solution both inside and outside the cooled cylinder in the reservoir, supplemented with a term proportional to the temperature at positions outside that region.

Myklestad developed his equations for a cooled or heated cylinder in a full space with homogeneous elastic properties. Realistic geological scenarios require the possibility of incorporating inhomogeneities. For the thermoelastic stresses these would be properties which are different for different layers. We applied the analytical correlations developed for homogeneous subsurface to situations with an elasticity contrast between reservoir and seal and base, but with proportionality factor for each contribution based on a benchmark exercise.

A.4 Poro-elastic stress

The developed pore pressure in the reservoir is a logarithmic function of the distance from the well. An obvious approach would therefore be to discretize the pressurized area and numerically integrate the contribution of pressurized "ring elements" to the poroelastic stress. We found, however, that an approximation of the effect of the complete pressurized reservoir with the effect of a single pressurized cylinder sufficed. The pressure and the radius of this cylinder depends on the position where we want to evaluate the stresses. Clearly, a calibration is crucial in this approach.

The best approximation that we found, in terms of simplicity and accuracy, uses a pressurized cylinder of radius $r_{eq}=10r$ and pressure $\Delta p_{eq}=\Delta p\left(\frac{1}{10}r_{eq},0\right)$ for the poroelastic effect at a position (r,z); $|z|\leq \frac{h}{2}$ in the reservoir $r_{eq}=10r+\left(|z|-\frac{h}{2}\right)$ and pressure $\Delta p_{eq}=\Delta p\left(\frac{1}{10}r_{eq},0\right)$ for the effect at a position (r,z); $|z|>\frac{h}{2}$ in the seal or the base. Figure 8-1 visualizes the concept for the equivalent pressurized cylinder. The effect of the pressurization of parts of the seal and the base are treated completely analogous to the thermoelastic effect of the cooling of those parts: we add a term $\frac{1-2\nu}{1-\nu}\alpha_{Biot}\Delta P$ to the cylinder contribution in the seal and the base, with the actual pressure at the point of calculation.

Introducing elasticity contrasts at the interfaces had only minor effect on the resulting poro-elastic stresses. This is due to the form of the source terms in the constitutive equation, $\alpha_{Biot}\Delta P + \beta_T\Delta T$. The elastic modulus is directly present in the second term for thermo-elasticity; it is absent in the first term. Only some effect of the Poisson ratio remains.

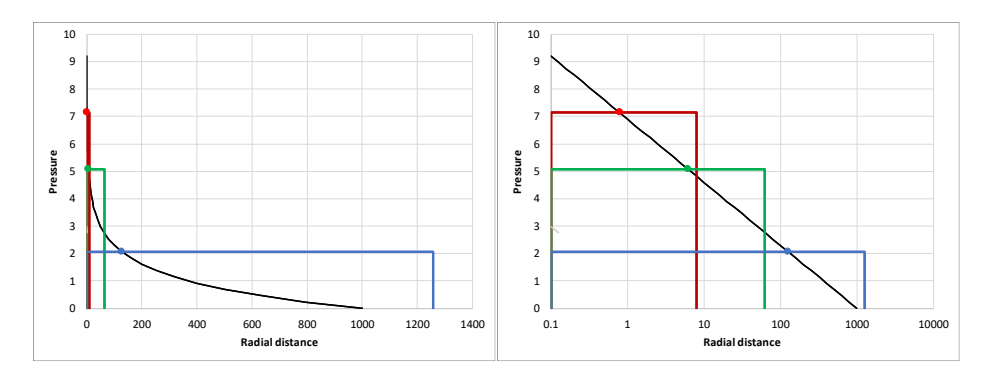


Figure 8-1

Concept of the equivalent pressurized cylinder. The poroelastic fields at the position of the red, green, and blue dots originates from the pressure in the reservoir that is given by the black curve. It is approximated by Myklestad's correlations for a pressurized cylinder with constant pressure inside it: the red, green and blue curves.

Figure A 1

A.5 Total stresses and Risk Measures

The calculated thermoelastic and poroelastic contributions to the stress are radially symmetric. If the virgin horizontal stresses are anisotropic, the rotational symmetry of the end product is broken and the poroelastic contributions must first be transformed to the cartesian coordinate system:

$$\sigma_{cart}^{PE} = \begin{pmatrix} \sigma_{xx}^{PE} & \sigma_{xy}^{PE} & \sigma_{xz}^{PE} \\ \sigma_{xy}^{PE} & \sigma_{yy}^{PE} & \sigma_{yz}^{PE} \\ \sigma_{xz}^{PE} & \sigma_{yz}^{PE} & \sigma_{zz}^{PE} \end{pmatrix}$$

$$= \begin{pmatrix} \cos \theta & \sin \theta & 0 \\ -\sin \theta & \cos \theta & 0 \\ 0 & 0 & 1 \end{pmatrix} \begin{pmatrix} \sigma_{r}^{PE} & 0 & \sigma_{rz}^{PE} \\ 0 & \sigma_{\theta}^{PE} & 0 \\ \sigma_{rz}^{PE} & 0 & \sigma_{z}^{PE} \end{pmatrix} \begin{pmatrix} \cos \theta & -\sin \theta & 0 \\ \sin \theta & \cos \theta & 0 \\ 0 & 0 & 1 \end{pmatrix}$$

$$\theta = \operatorname{atan} \left(\frac{y}{x}\right)$$

This expression makes use of the fact that induced shear stresses along the tangential coordinate must be zero because of the symmetry. With the maximum and minimum horizontal stresses, σ_{H0} and σ_{h0} , in the x and y direction, the final total stress and the final effective stress then are given by

$$\sigma_{total} = \sigma_{0} + \sigma_{cart}^{PE} = \begin{pmatrix} \sigma_{xx}^{PE} + \sigma_{H0} & \sigma_{xy}^{PE} & \sigma_{xz}^{PE} \\ \sigma_{xy}^{PE} & \sigma_{yy}^{PE} + \sigma_{h0} & \sigma_{yz}^{PE} \\ \sigma_{xz}^{PE} & \sigma_{yz}^{PE} & \sigma_{zz}^{PE} + \sigma_{v0} \end{pmatrix}$$
8-8
$$\sigma^{eff} = \sigma_{total} - P\delta_{ij} = \begin{pmatrix} \sigma_{xx}^{PE} + \sigma_{H0} - P & \sigma_{xy}^{PE} & \sigma_{xz}^{PE} \\ \sigma_{xy}^{PE} & \sigma_{yy}^{PE} + \sigma_{h0} - P & \sigma_{yz}^{PE} \\ \sigma_{xz}^{PE} & \sigma_{yz}^{PE} & \sigma_{zz}^{PE} + \sigma_{v0} - P \end{pmatrix}$$

There are different possibilities to define a measure for the reactivation risk. A first one is exceedance of the Mohr-Coulomb failure criterion on an existing fault. For a fault characterized with a normal vector \mathbf{n} we calculate the effective traction \mathbf{T}' on the plane, and the effective normal and shear stresses on the plane as

$$\mathbf{T}' = \sigma^{eff} \cdot \mathbf{n}$$

$$\sigma_n' = \mathbf{T}' \cdot \mathbf{n}$$
8-9

$$|\tau| = \sqrt{\mathbf{T}' \cdot \mathbf{T}' - \sigma_n'^2}$$

The slip tendency of the fault at evaluation is then given by the ratio between shear and effective normal stress, and the associated shear capacity utilization is defined as

$$SCU = \left| \frac{\tau}{C + f_S \sigma_n'} \right|$$
 8-10

Faults with a SCU larger than the unity will be reactivated.

A second measure is the exceedance of the failure criterion for the fault orientation that is most critically oriented. This can also be quantified as the slip tendency, but now for the fault orientation that is most prone to failure. The calculation does not require stresses for all possible orientations; it suffices to determine the principal stresses and the associated shear capacity of the rock, which is a measure for the proximity of the Mohr circle to the failure envelope. The shear capacity utilization for the critical orientation is calculated as

$$SCU = \frac{\sqrt{1 + f_s^2} (S_{max}' - S_{min}')}{f_s (S_{max}' + S_{min}') + 2C}$$
8-11

Failure will occur if the value for the shear capacity is larger than unity. The measure is defined locally. A third measure is the radius up to which failure occurs. It can be calculated by defining the maximum distance from the wellbore at which the shear capacity exceeds unity. The measure can be employed as a standalone measure or in conjunction with the position of the cooled front.

Finally, a fourth measure can be formulated as the percentage of possible fault orientations which are critical (Levandowski, 2018). The method to calculate this number is to calculate the criticality for a large number of evenly distributed fault orientations. This measure is a local measure. It can therefore be used to map the spatial distribution or in conjunction with the position of the cooling front.

A.6 Benchmark of the pressure and temperature calculation in SRIMA

We have validated the SRIMA-calculated temperature and pressure fields to output generated by Eclipse for the same input parameters. To this end we modelled an aquifer in which we injected cold water for a long time. The base case of the aquifer thickness of 100 m was varied: 30 m and 300 m thickness was also tested. Figure A 2 and Figure A 3 show excellent agreement between the SRIMA results and the Eclipse results. For thicker and thinner reservoirs, the agreement was the same. Only some numerical diffusion in Eclipse causes a more gradual temperature decrease in the reservoir; further, the leakage of (negative) heat to the bounding layers causes some vertical differentiation of the temperature profile in the aquifer near the thermal boundary.

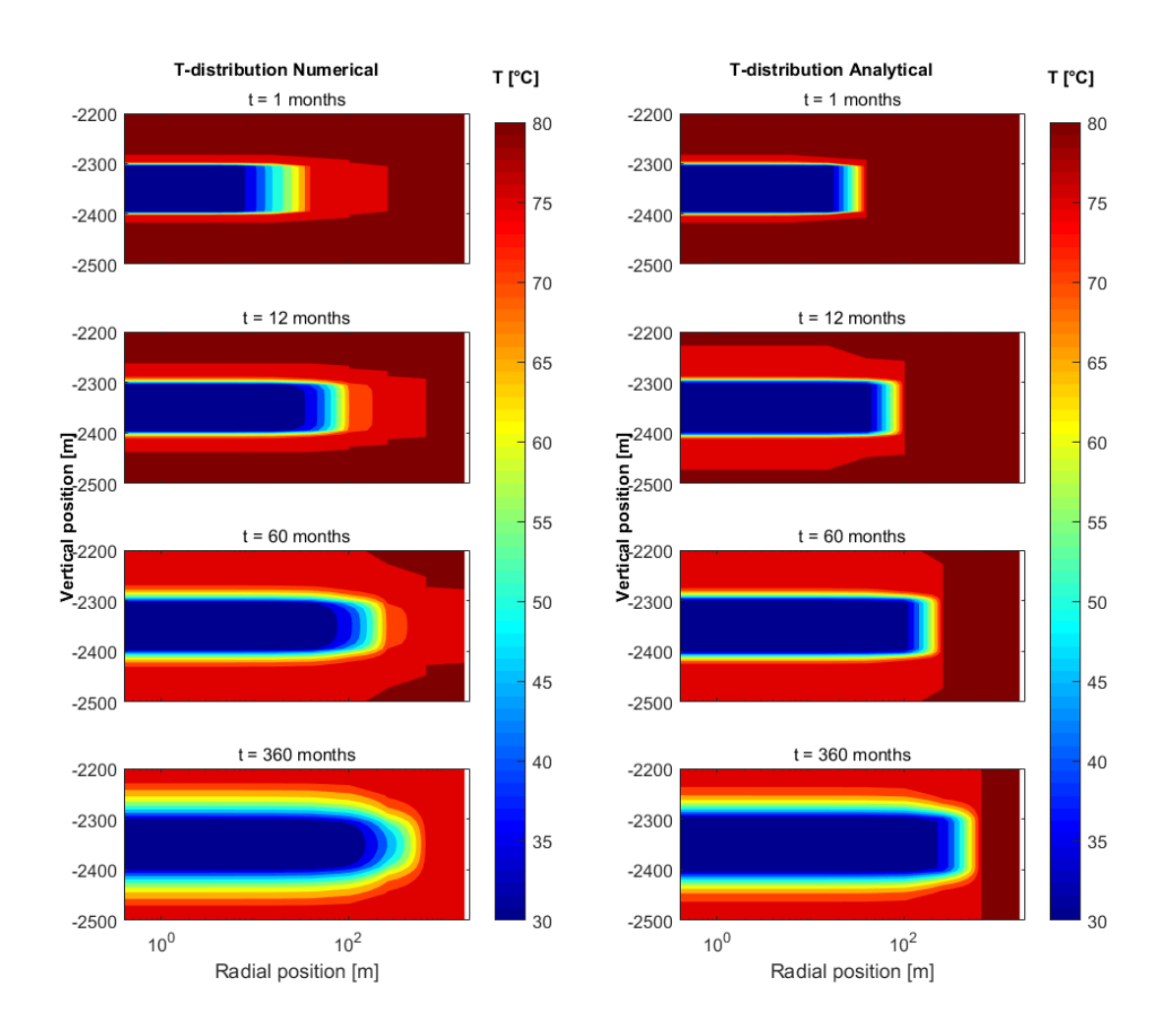


Figure A 2 Contour plots of the benchmark results of the temperature correlations. Left: numerical results. Right: Analytical results with SRIMA. Note that the radial axis is spaced logarithmically

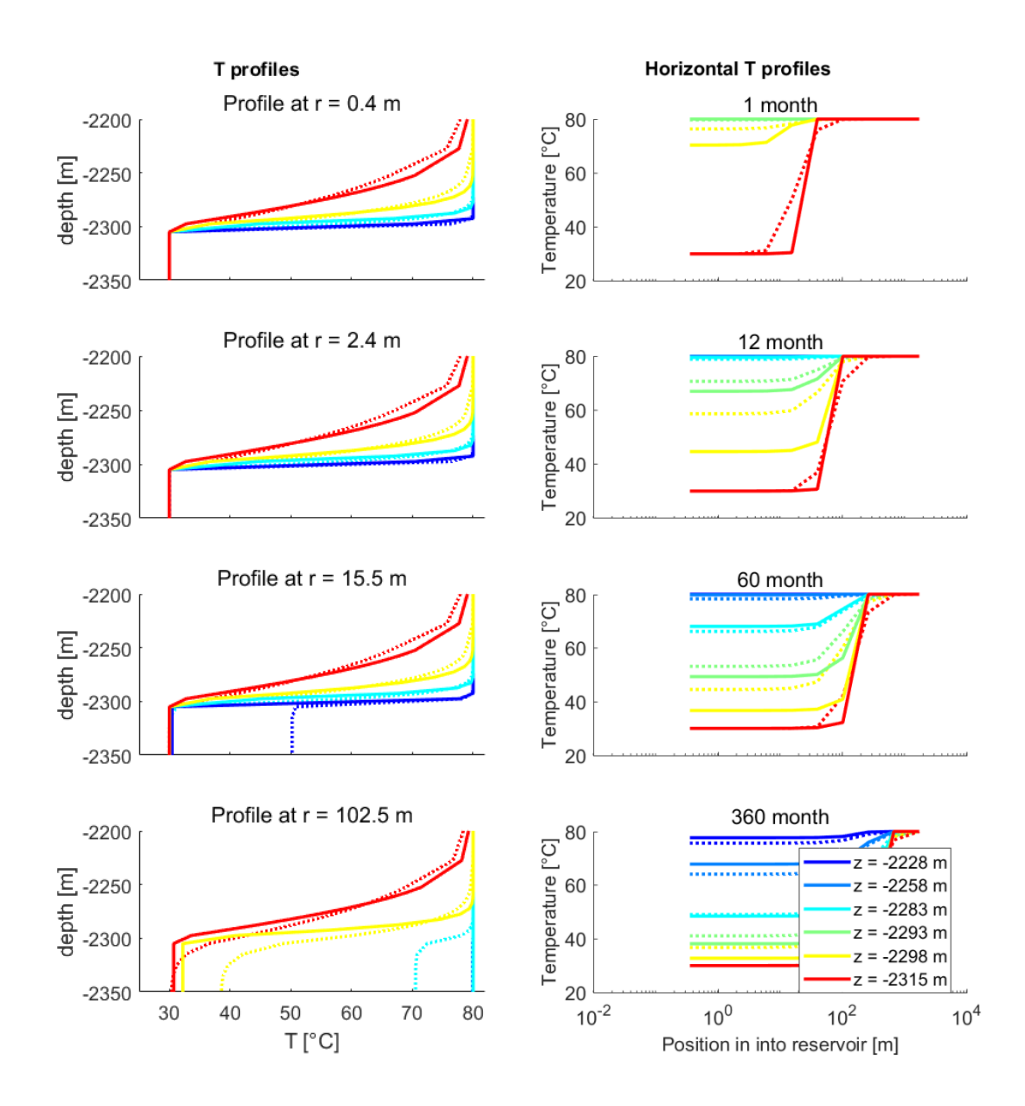


Figure A 3 Line plots of the benchmark results of the temperature correlations at different distances from the well. Left: vertical profiles. Colors dark blue, light blue, yellow and red indicate timings at 1, 12, 60 and 360 months; dotted curves are numerical results and solid curves are analytical results. Right: horizontal profiles at different vertical positions and different times

The pressure response as calculated in SRIMA was also verified using Eclipse. Figure A 4 and Figure A 5 give the results. As expected, the pressure profiles are indeed logarithmically decreasing with the radius, with different slopes in the cold and hot zones. This is best demonstrated in the profiles along a horizontal line: the pressures in the reservoir (red lines in right plot of Figure A 5) show a change in slope at the position of the cold front. Profiles for the 30-m and 300-m thick reservoir showed essentially the same behavior. The correspondence between numerical and analytical results in the bounding layers is slightly worse than for the temperature; this is mainly due to the pressure gradient present along the complete reservoir. Actually, this validation was used as a benchmark for the optimization of the choice of the effective cylinder pressure mentioned in Section A.2.

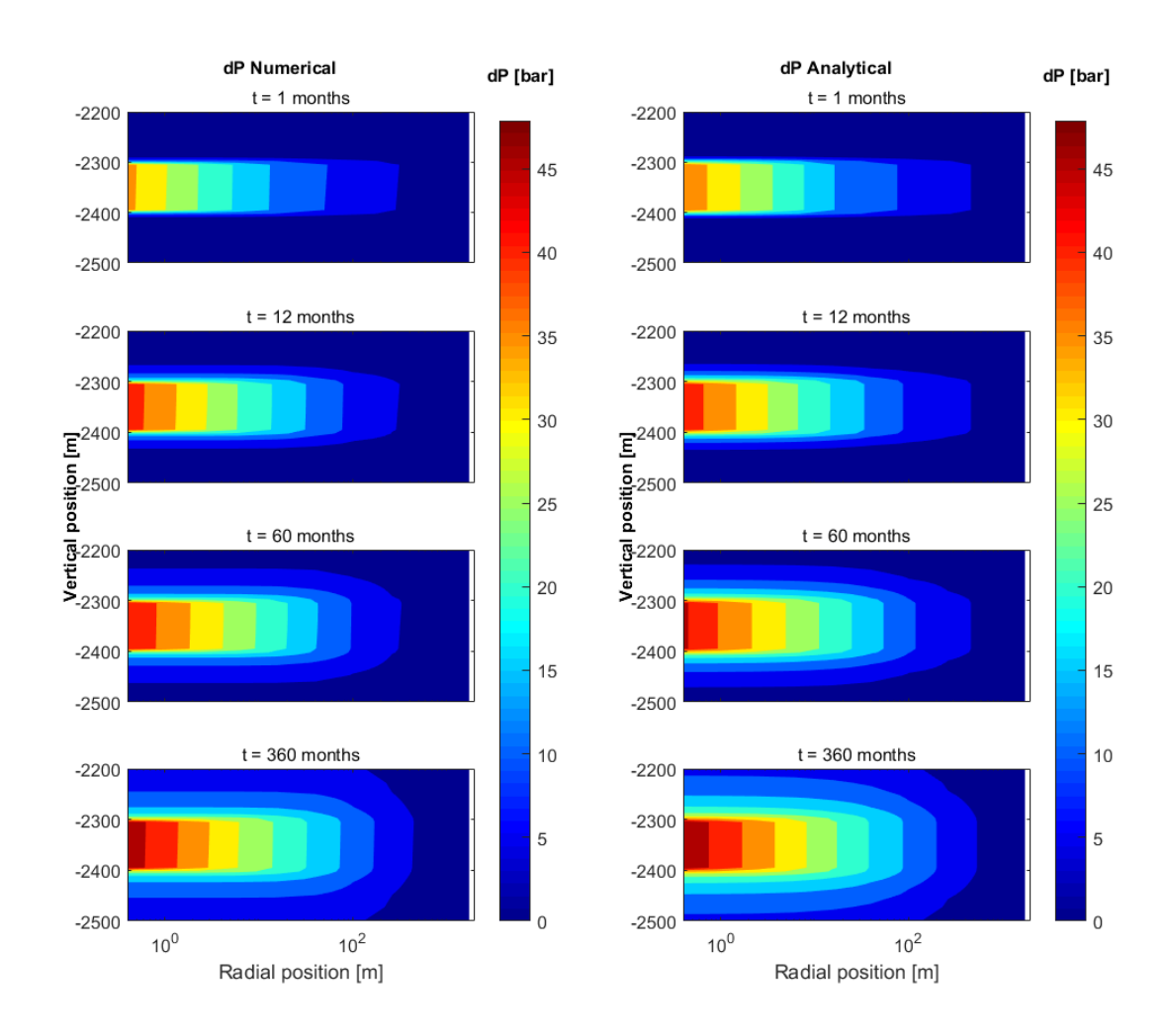


Figure A 4 Contour plots of the benchmark results of the pressure correlations. Left: numerical results. Right: Analytical results with SRIMA. Note that the radial axis is spaced logarithmically.

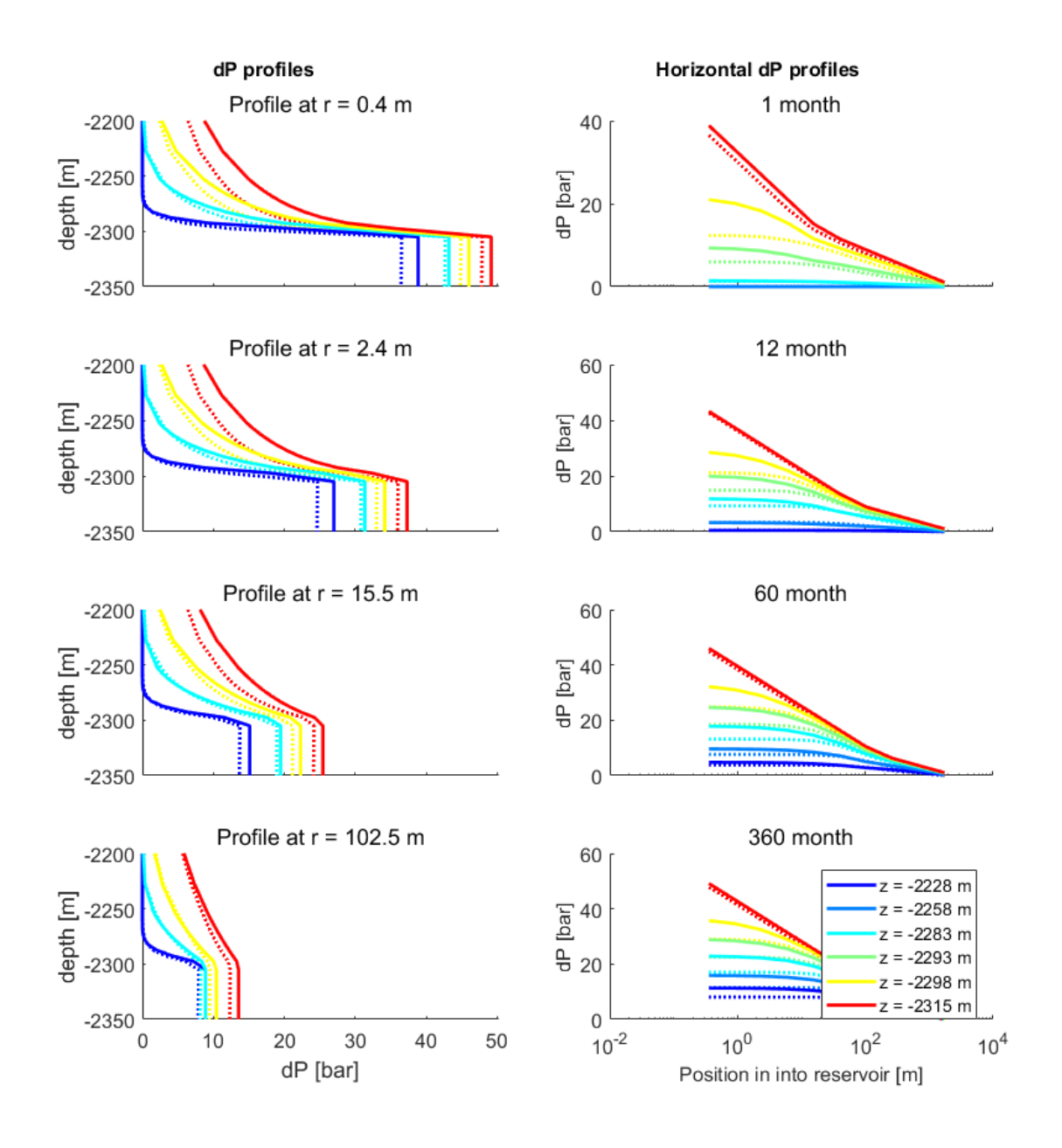


Figure A 5 Line plots of the benchmark results of the pressure correlations at different distances from the well. Left: vertical profiles. Colors dark blue, light blue, yellow and red indicate timings at 1, 12, 60 and 360 months; dotted curves are numerical results and solid curves are analytical results. Right: horizontal profiles at different vertical positions and different times

A.7 Benchmark of stress calculation: Model setup and input parameters

SRIMA simulates the poro-thermo-elastic stress changes due to injection into a reservoir formation overlain by a seal formation and underlain by a base formation (Section 3.3). The calculation of the stress change has been benchmarked against the Finite Element software DIANA FEA. The model setup in DIANA is similar to that of SRIMA; however, whereas seal and base are assumed to have infinite height in SRIMA a free surface is included in DIANA and the model depth is finite with a maximum depth of -5000 m (Figure A 6). Fixed displacement boundaries were imposed at the model sides and base, preventing displacement in the direction perpendicular to the boundary but allowing

displacement parallel to the boundaries. Like in SRIMA the model width was 2500 m and the well radius 0.2 m, and the reservoir formation was situated at -2300 m with a thickness of 100 m. The formations were modeled with linear triangular and quadrilateral elements (T6AXI and Q8AXI). The element size increased from 2 m at the well in the reservoir to a maximum of 20 m further away from the well.

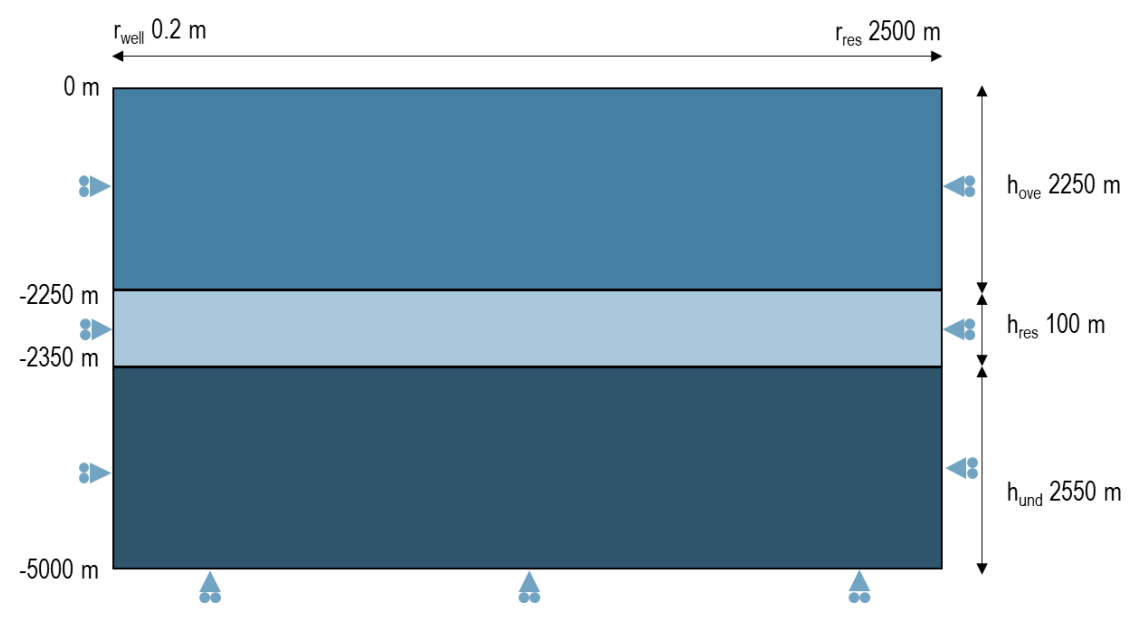


Figure A 6 Axisymmetric model in DIANA used to benchmark stress calculation in SRIMA. Triangles indicate the presence of displacement boundaries preventing motion perpendicular to the boundary.

Table A 1 Input parameters used for the benchmark of stress changes computed in SRIMA vs Eclipse and DIANA FEA.

Parameter (DIANA & SRIMA)	Symbol	Unit	Value
Mid depth	Ymid	m	2300
Reservoir thickness	h	m	100 (30, 300)
Throw	t	m	NA
Dip	θ	0	70
Vertical stress gradient	$\Delta \sigma_v / \Delta y$	MPa/km	22.6
Stress ratio σ_h / σ_v	K_0	-	0.708
Horizontal stress ratio $\sigma H / \sigma h$	σ_H/σ_h	-	1
Pressure gradient	$\Delta \sigma_{v}/\Delta y$	MPa/km	10.72
Strike with respect to σ_H	φ	deg	0
Overpressure in the reservoir	P_{exc}	MPa	0
Biot coefficient	α	-	1
Poisson's ratio	v	-	0.1
Young's modulus	E	GPa	15 (3.75, 60)
Linear thermal expansion coefficient	η	°C -1	1.20 · 10-5
Static friction	f_s	-	0.6
Flow-Temp parameters (Eclipse & SRIMA)			
Permeability	k	mD	500
Overburden permeability	kseal	mD	3.0 · 10-5
Reservoir temperature	T_{res}	°C	80
Injection temperature	T_{inj}	°C	35
Thermal conductivity	K_{rock}	W/mK	3.50
Specific heat capacity water	Cfluid	J/kgK	4200
Specific heat capacity rock	Crock	J/kgK	850
Seal density	$ ho_{rock}$	kg/m3	2200
Seal porosity	ϕ_{seal}	-	0.1
Seal Poisson ratio	Vseal	-	0.1
Density water	$ ho_w$	kg/m3	1000
Mass injection rate	q	kg/s	50
Water viscosity at T0	μ_c	Pas	0.0003
Water viscosity at Tinj	μ_h	Pas	0.001
Total compressibility	c	1/Pa	4.0 · 10-10

For the validation of the induced stresses, pressures and temperatures were computed in SRIMA. This PT-field was used as an input in DIANA, so both SRIMA and DIANA started with the same PT-changes from which the poro-thermo-elastic stresses are computed. The PT-field was computed at the node locations of the DIANA mesh. The PT-field after 30 years of injection was used for the benchmark. Note that rather than a temperature gradient as used in Chapter 5 a constant initial temperature of 80 degrees was assumed for the reservoir and seal and base formations.

In the benchmark exercise we compared both the horizontal, vertical and shear stress, as well as the Coulomb Stress Changes which are important for fault reactivation. Coulomb Stress Changes (CSC) are calculated as

$$CSC = \Delta \tau - f_s \Delta \sigma_n'$$
 8-12

Where $\Delta \tau$ is the shear stress change, $\Delta \sigma_n'$ is the effective normal stress change on the fault, and f_s is the static friction coefficient. For the Coulomb Stress Change a fault dip of 70° was used and a friction coefficient of 0.6.

A.8 Benchmark of stress changes - Uniform elasticity

Figure A 7 shows the horizontal and vertical stress changes modeled in DIANA and SRIMA after 30 years of injection, and Figure A 8 shows the shear, normal, and Coulomb stress changes for a fault dip of 70°. The cooling front extends for 570m from the wellbore, which is clearly reflected in the stress changes; the largest stress changes occur within the cooled volume. Since the pressure changes are small (Section 3.4.1) the poro-elastic response is limited and the stress response is dominated by thermo-elastic stress changes. The stress response to injection can be summarized as following:

- A decrease in total horizontal stress in the cooled volume, of 8.1 MPa for the current model. This is slightly less than the horizontal stress decrease for the same amount of cooling ($\Delta T = -45^{\circ}$) for a laterally extensive reservoir, which is given by $\Delta \sigma_{x(laterally \text{ extensive})} = E_{\eta} \Delta T/(1-v) = -9$ MPa (Figure A 7).
- A decrease in total vertical stress in the cooled volume. This decrease is much smaller than the horizontal stress decrease, with a maximum decrease of -2 MPa (Figure A 7).
- The largest shear stress changes occur at the outer edges of the cooled front (Figure A 7).
- The Coulomb Stress Change is largest within the cooled volume (Figure A 8, Figure A 9). The positive values of the CSC indicates the stress becomes more critical for the typical normal faulting orientation considered here.

Vertically oriented stress concentrations can be seen in the vertical stress changes computed in SRIMA (Figure A 7, Figure A 9). These stress concentrations are an artefact due to simplifications made for the analytical thermo-elastic stress calculation. The temperature field was approximated with 10 cylinders, each with a uniform temperature decrease of 10% of the total temperature decrease and a radius corresponding to 10% temperature decrease. The thermo-elastic stresses of each of these 10 cylinders can be computed analytically using the Myklestad solution, and stress changes of each cylinder are superimposed to obtain the total thermo-elastic stress changes (Section A.3). In DIANA the thermo-elastic stress is computed directly from the temperature field and no such concentrations are seen.

Furthermore, the comparison between SRIMA and DIANA FEA shows that, for uniform elasticity:

- SRIMA overestimates the horizontal stress decrease within the cooled reservoir volume by ~7% (Figure A 9).
- SRIMA underestimates the vertical stress decrease within the cooled reservoir volume with ~1 MPa which is ~30-50% of the total vertical stress decrease (Figure A 7, Figure A 9). In Figure A 9 the variations in vertical stress due to the approximation of the temperature with discrete cylinders as mentioned above can be seen, with abrupt changes in vertical stress of ~0.5 MPa which locally cause larger differences with respect to the DIANA results.
- SRIMA overestimates the Coulomb Stress change on a fault within the cooled reservoir volume computed by 15%, and even more in the cooled volume of the seal or base (Figure A 8, Figure A 9).
- SRIMA is thus conservative for fault reactivation within the cooled volume, for a normal faulting regime and relatively steep faults.
- Just to the side of the cooled volume (~600 m from the well) SRIMA underestimates the vertical stress increase and horizontal stress decrease. The resulting Coulomb stress change is underestimated by SRIMA; hence, SRIMA is not conservative just outside of the cooling front. Overall, the agreement between DIANA and SRIMA is reasonable (<7% difference in most of the cooled volume) and SRIMA is conservative within the cooled volume. However, just outside the cooling front SRIMA is not conservative. This should be considered for fault reactivation studies. Also, care must be taken not the consider the artificial vertical stress variations for fault reactivation.

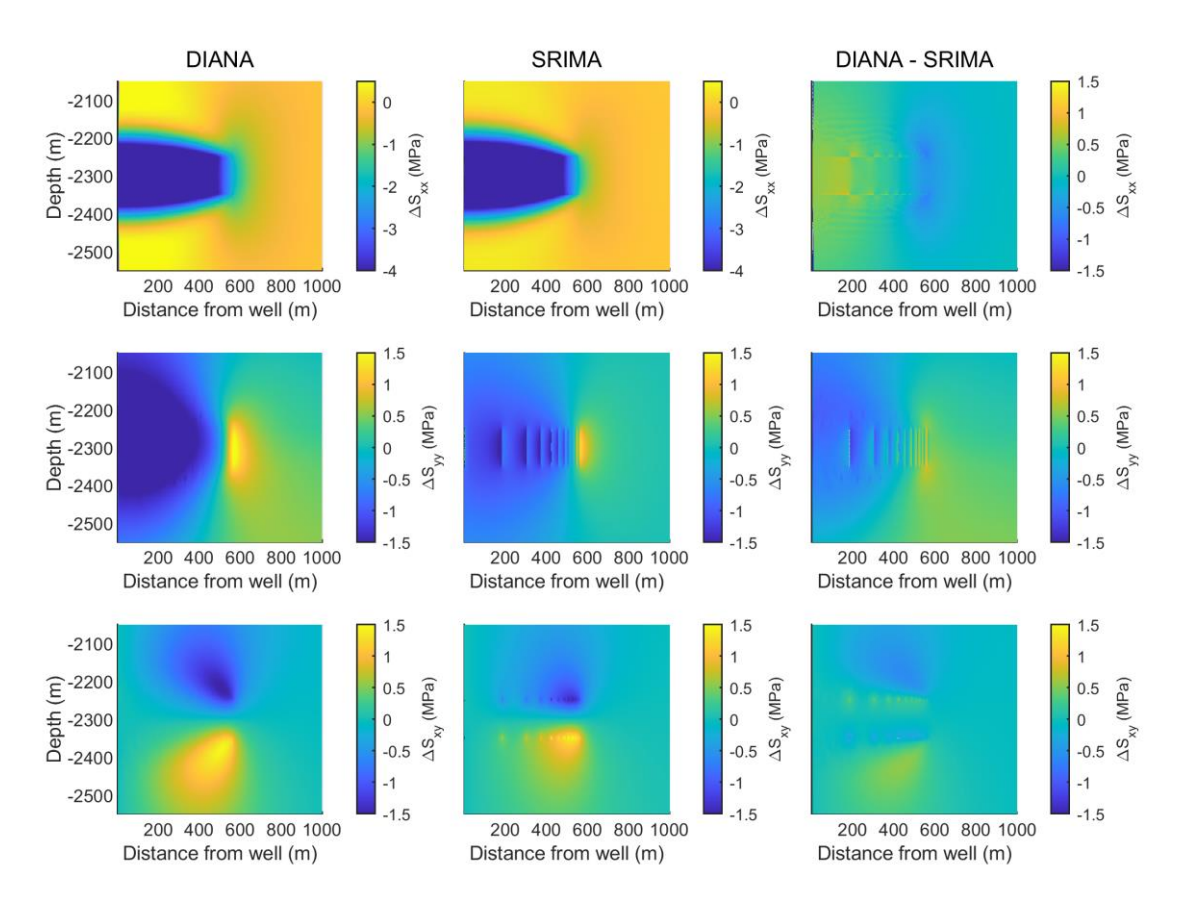


Figure A 7 Stress changes modeled in DIANA and SRIMA and differences between stress changes in both models, for a uniform elastic properties. Stress changes are computed after 30 years of injection. Horizontal stress change: ΔS_{xx} , vertical stress change: ΔS_{xy} , and shear stress change: ΔS_{xy} . Left column shown DIANA results, and the middle column the results from SRIMA. Right column shows the difference in stress change between DIANA and SRIMA, with positive values indicating the stress computed in DIANA is larger than in SRIMA.

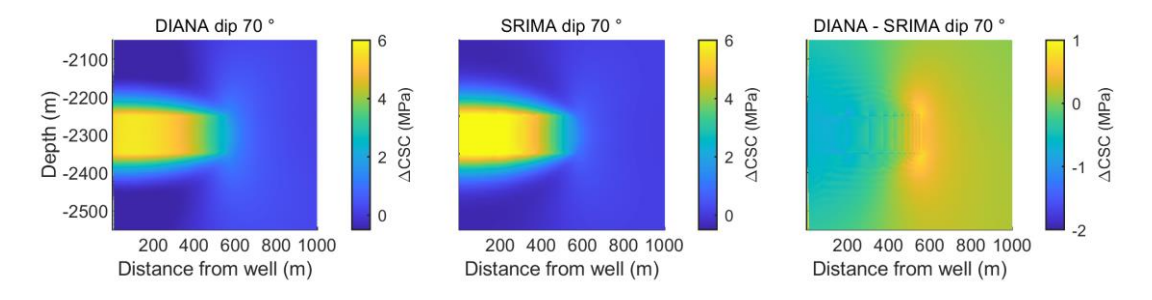


Figure A 8 Coulomb Stress Changes modeled in DIANA and SRIMA and differences between stress changes in both models, for a uniform elastic properties, a dip of 70° and a friction coefficient of 0.6. Stress changes are computed after 30 years of injection.

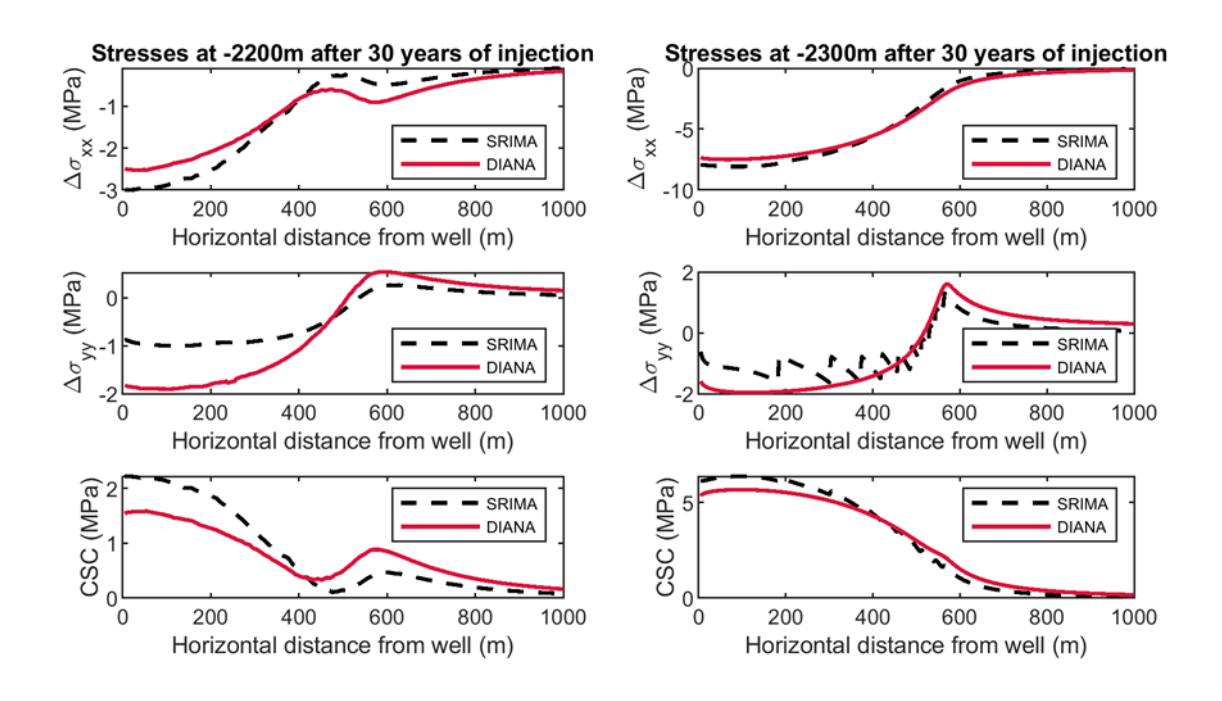


Figure A 9 Comparison of horizontal and vertical stress changes and Coulomb Stress Changes computed in DIANA and SRIMA at different depths, for uniform elasticity. Lefthand side: -2200 m depth, 50 m up into the seal formation. Righthand side: -2300 m depth, in the middle of the reservoir.

A.9 Benchmark of stress changes - Stiffer seal and base

The poro-thermo-elastic stress changes have also been compared for heterogeneous elasticity, with seal and base formations having a 4x higher stiffness than the reservoir. Note that this is an upper bound to stiffness contrasts, in reality it is likely less and model differences resulting from heterogeneous elasticity are also less.

The comparison between SRIMA and DIANA FEA shows that, for a 4x stiffer seal and base formation:

- The largest horizontal stress decrease and Coulomb stress increase occur in the cooled parts of the seal and base formations due to the higher stiffness.
- Within the reservoir the agreement between both the horizontal and vertical stress changes computed in DIANA and SRIMA is good (<5% difference), though artificial stress concentrations in vertical stress locally cause larger differences.
- The agreement between the stress changes within the cooled reservoir volume is better than for uniform elasticity, likely because the stiff seal and base reduce stress arching effects which is not captured in SRIMA.
- SRIMA overestimates the horizontal stress decrease in the cooled parts of the seal and base by ~15-20%
- SRIMA underestimates the vertical stress decrease above and below the cooled reservoir area by 50%
- The Coulomb stress changes (CSC) computed in the cooled reservoir volume show good agreement, but SRIMA overestimates the Coulomb stress change in the cooled parts of the seal and base by ~30%. Again, SRIMA is thus conservative in that it returns a larger CSC than DIANA.
- To the side of the cooled parts of the seal and base, SRIMA underestimates the Coulomb stress change.

The discrepancies are related to the application of analytical equations developed for a homogeneous body. The approximations made in Section A.3 do not correctly incorporate stress arching in a heterogeneous subsurface.

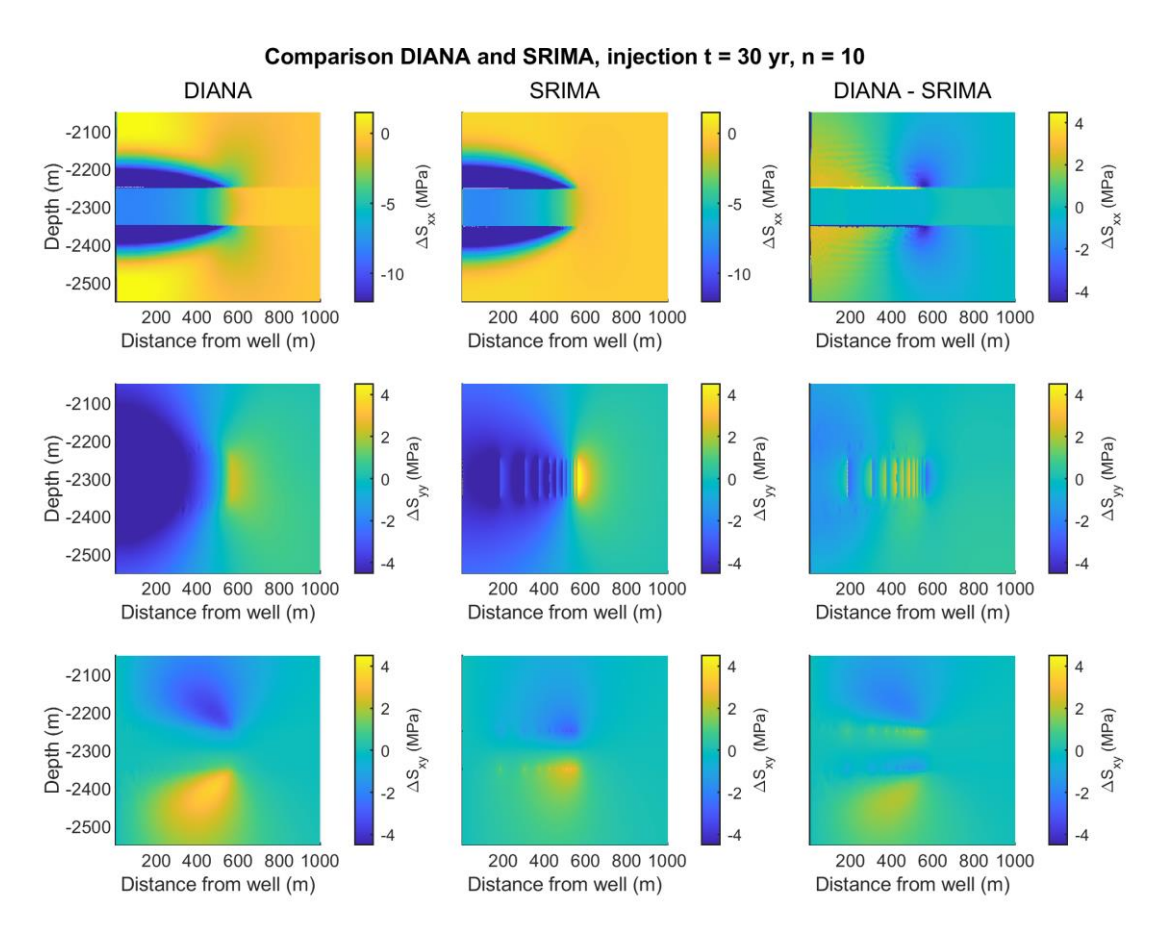


Figure A 10 Stress changes modeled in DIANA and SRIMA and differences between stress changes in both models, for a 4x stiffer seal and base formation. Stress changes are computed after 30 years of injection. Horizontal stress change: ΔS_{xx} , vertical stress change: ΔS_{xy} , and shear stress change: ΔS_{xy} . Right column shows the difference in stress change between DIANA and SRIMA, with positive values indicating the stress computed in DIANA is larger than in SRIMA.

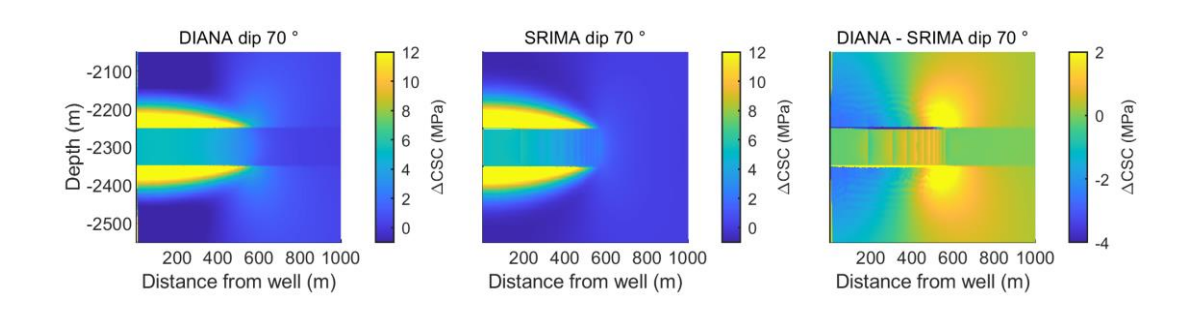


Figure A 11 Coulomb stress changes modeled in DIANA and SRIMA and differences between stress changes in both models, for a 4x stiffer seal and base formation. Coulomb stress changes (ΔCSC) are computed after 30 years of injection, for a 70° dipping fault at all locations in the model domain. Right column shows the difference in stress change between DIANA and SRIMA, with positive values indicating the Coulomb stress computed in DIANA is larger than in SRIMA.

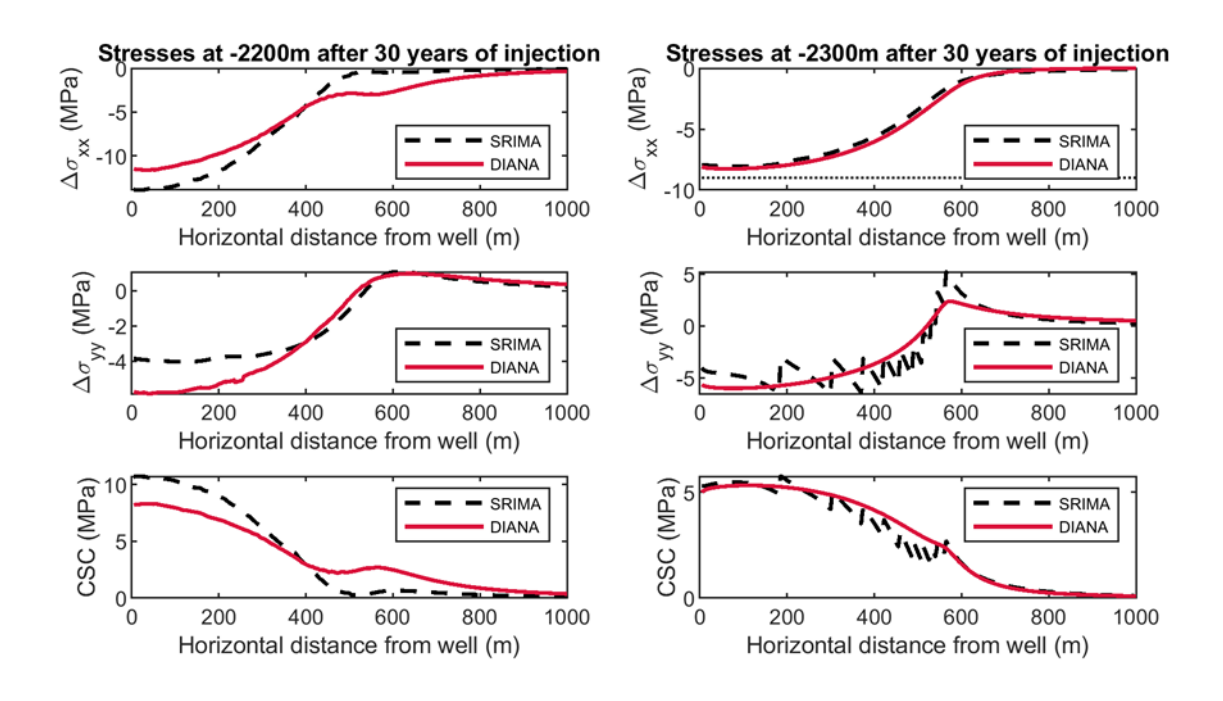


Figure A 12 Comparison of horizontal and vertical stress changes and Coulomb Stress Changes computed in DIANA and SRIMA at different depths, for 4x stiffer seal and base formations. Lefthand side: -2200 m depth, 50 m up into the seal formation. Righthand side: -2300 m depth, in the middle of the reservoir.

A.10 Benchmark of stress changes - More compliant seal and base

The poro-thermo-elastic stress changes have also been compared for heterogeneous elasticity, with seal and base formations having a 4x lower stiffness than the reservoir. Note that this is a significant contrast in stiffness, in reality it is likely less and differences resulting from heterogeneous elasticity are also less.

The comparison between SRIMA and DIANA FEA shows that, for a 4x more compliant seal and base formation (Figure A 13, Figure A 14, Figure A 15):

- SRIMA overestimates the horizontal stress decrease in the cooled reservoir volume by ~25% (Figure A 13, Figure A 15)
- SRIMA overestimates the Coulomb stress increase within the cooled reservoir volume by ~25% and is thus conservative within the cooled reservoir volume.
- SRIMA underestimates the vertical stress increase and the horizontal stress decrease to the side of the cooled reservoir volume
- SRIMA underestimates the Coulomb stress increase to the side of the cooled reservoir volume and is thus not conservative at this location.
- Stress changes outside of the cooled reservoir formation volume are significantly smaller than within the reservoir formation, but the relative mismatch between SRIMA and DIANA can be up to 100%.

Again, the discrepancies are related to the use of analytical correlations to heterogeneous subsurface for which they were not developed.

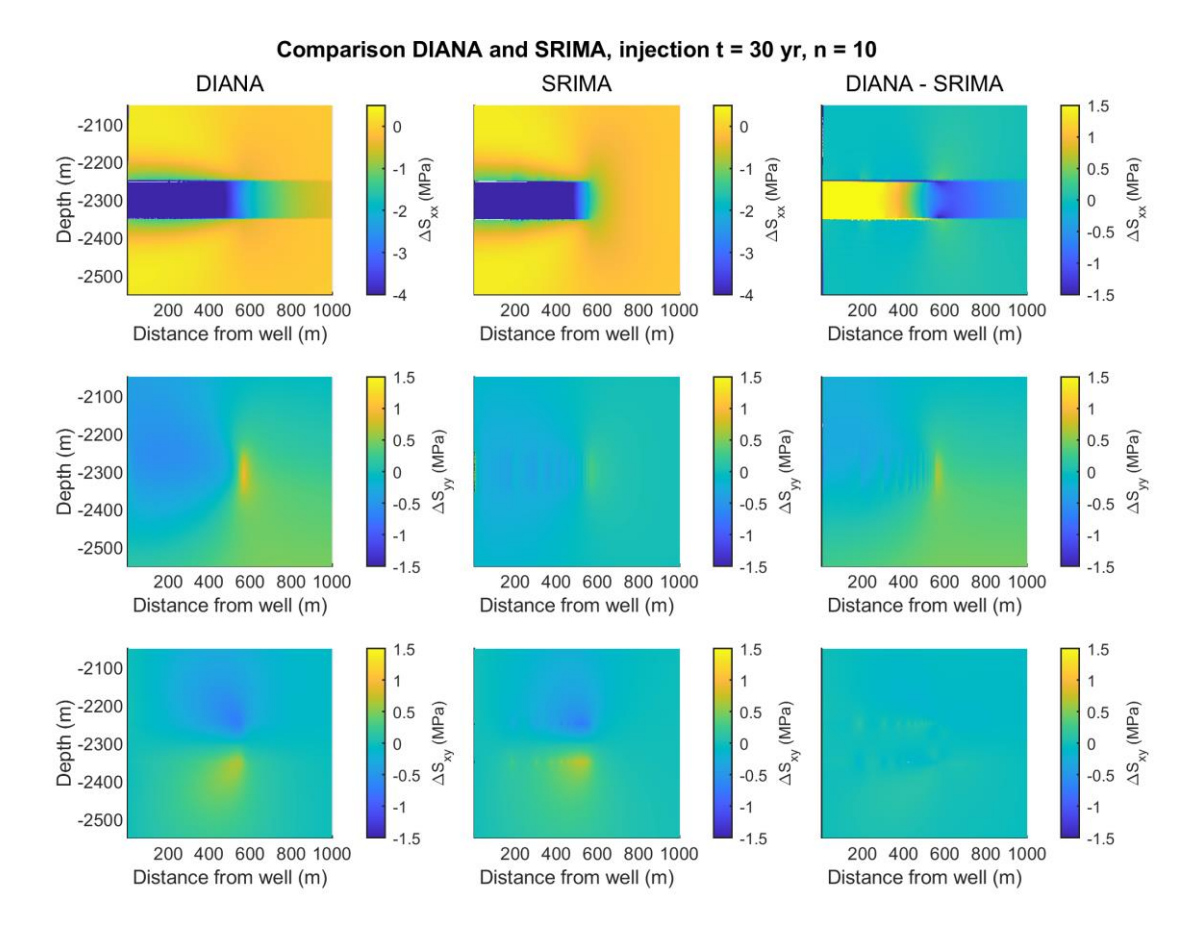


Figure A 13 Stress changes modeled in DIANA and SRIMA and differences between stress changes in both models, for a 4x more compliant seal and base formation. Stress changes are computed after 30 years of injection. Horizontal stress change: ΔS_{xy} , vertical stress change: ΔS_{yy} , and shear stress change: ΔS_{xy} . Right column shows the difference in stress change between DIANA and SRIMA, with positive values indicating the stress computed in DIANA is larger than in SRIMA.

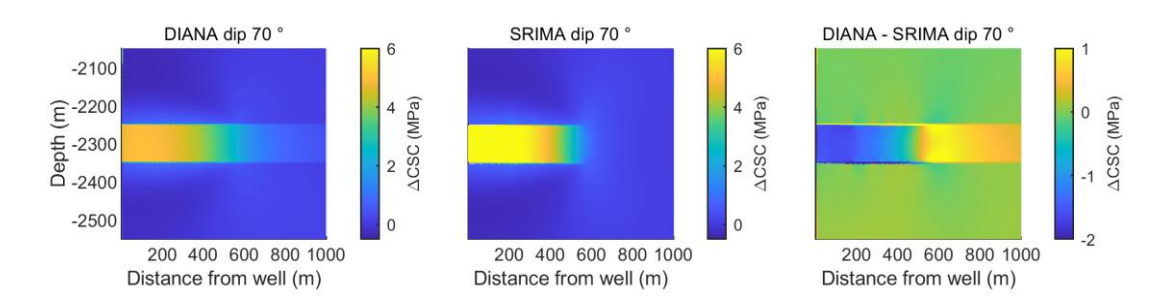


Figure A 14 Coulomb stress changes modeled in DIANA and SRIMA and differences between stress changes in both models, for a 4x more compliant seal and base formation. Coulomb stress changes (Δ CSC) are computed after 30 years of injection, for a 70° dipping fault at all locations in the model domain. Right column shows the difference in stress change between DIANA and SRIMA, with positive values indicating the Coulomb stress computed in DIANA is larger than in SRIMA.

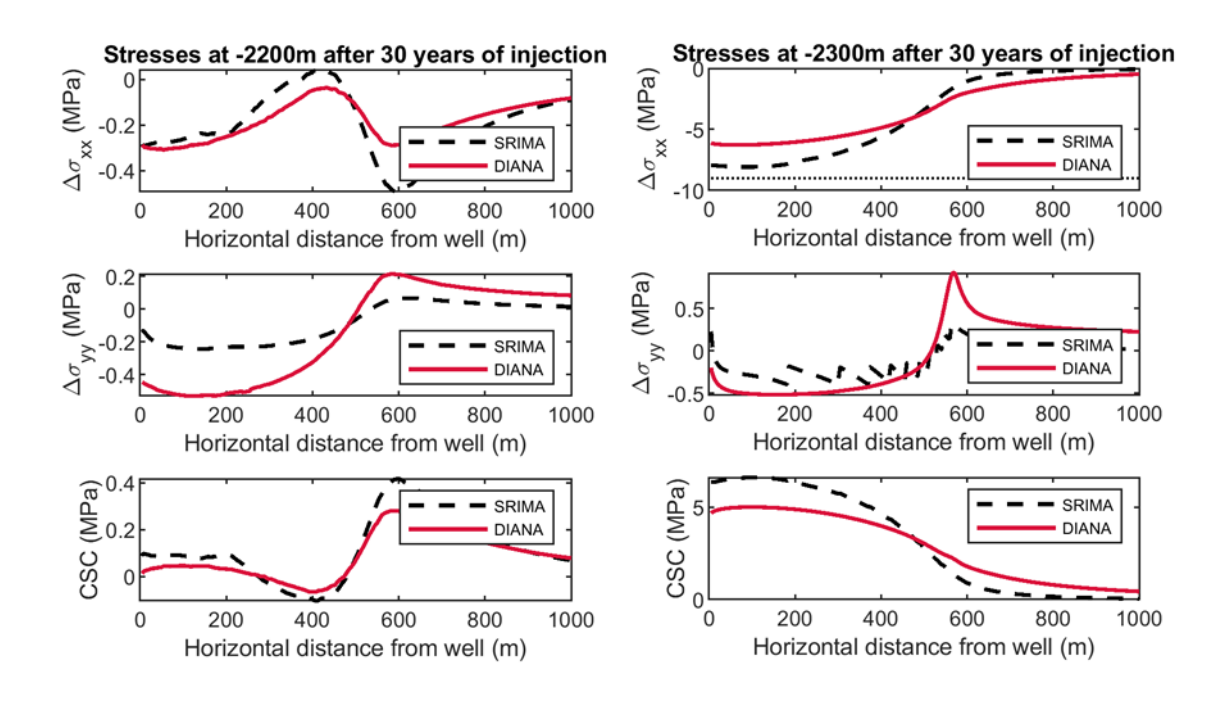
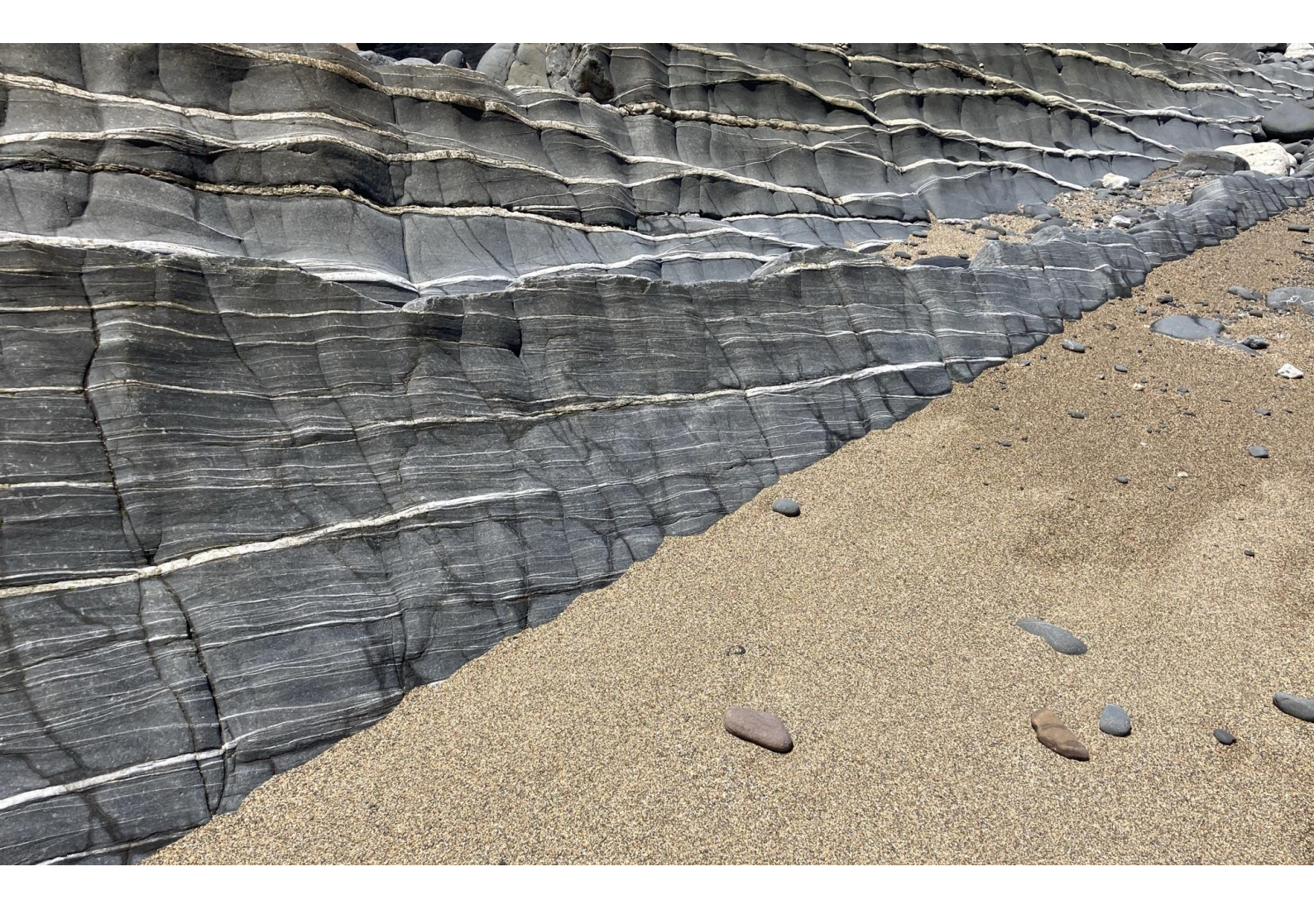


Figure A 15 Comparison of horizontal and vertical stress changes and Coulomb Stress Changes computed in DIANA and SRIMA at different depths, for 4x more compliant seal and base formations. Lefthand side: -2200 m depth, 50 m up into the seal formation. Righthand side: -2300 m depth, in the middle of the reservoir.





Adres

Princetonlaan 6 3584 CB Utrecht

Postadres

Postbus 80015 3508 TA Utrecht

Telefoon

088 866 42 56

E-mail

contact@warmingup.info

Website

www.warmingup.info